BIOCHEMICAL AND BIOPHYSICAL CHARACTERIZATIONS OF IMMUNOGLOBULIN SUPERFAMILY RECEPTORS NEOGENIN AND L1

Thesis by

Fan Yang

In Partial Fulfillment of the Requirements for the

degree of Doctor of Philosophy

CALIFORNIA INSTITUTE OF TECHNOLOGY

Pasadena, California

2011

(Defended September 10, 2010)

ACKNOWLEDGEMENTS

I am deeply indebted to my advisor, Professor Pamela J. Björkman, for giving me this great opportunity to explore biochemical research. She has always had confidence in my capability even though I had no prior training in biology. Without her support, I wouldn't have come this far. I am also grateful for her understanding and encouragement when I had difficulties in research or everyday life.

I would like to express the deepest appreciation to my committee chair, Professor Douglas C. Rees, whose guidance and persistent help in these many years made this dissertation possible. I also want to thank my committee members, Professor Aron Kuppermann and Professor Rob Phillips. Aron has always been insightful – he often reminded me of my physical chemistry background with his inspiring questions. Collaboration with Rob and Rob's former graduate student Tristan on the L1 project has been a great experience and I benefited a lot from it.

Dr. Anthony P. West initiated one of the thesis projects before I joined the lab. I want to express my heartfelt gratitude to him for being such a great scientist and a good mentor over the years. I also received plenty of technical advice from many outstanding fellow researchers, including former graduate students Agi Hamburger, Devin Tesar, Adrian Rice, and Joshua Klein, former postdoctoral scholars Drs. Zhiru Jenny Yang, Rich Olson, Tal Arnon, Elizabeth (Libby) Sprague, and Galina Jerdeva. Jenny has been a great friend and mentor since I joined the lab in early 2005 and I feel very fortunate to have shared the many years in the lab with her. Thanks Kathryn (Beth) Huey-Tubman, Rachel Galimidi, Priyanthi Gnanapragasam, and Paola Marcovecchio for being great colleagues and good friends. Discussions with Dr. Zhenfeng Liu at the Rees lab and Dr. Yan Zhang at the Chan lab were always helpful and I want to thank them for that. Dr. Jens Kaiser has been a great resource and extremely fun to talk to.

Special thanks go to Inder Nangiana, Michael Anaya, Dr. Jost Vielmetter, and the Caltech Protein Expression Center for assistance in expression of almost all proteins I ever made, Pavle Nickolovski and the Caltech Molecular Observatory for assistance

with automated crystallization, and former X-ray lab manager Dr. Leonard Thomas for his help with my first X-ray data collection.

Collaboration with Dr. An-Sheng Zhang at the Enns lab at Oregon Health and Sciences University has been pleasant and rewarding. I hope to see more of the iron-regulatory protein story with your never-ending effort.

I also want to express my gratitude to Dr. Ken Brakke, the author of Surface Evolver, for troubleshooting with the simulation script promptly.

I wish to thank Marta Murphy, Lynda Llamas, Dian Buchness, Agnes Tong, Icy Ma, and all other administrative staff for supporting me during the completion of this thesis project.

Last but not least, I would like to thank my husband Yu Liu for his continuous love over the years. Thanks to my adorable 17-month old son Yun-cong Evan Liu for giving me all the smiles. Thanks to my mother, Nanying Liang, who always offers her love and support when I need it most and for being understanding the entire time. I dedicate this work to them.

ABSTRACT

Immunoglobulin (Ig) superfamily receptors function in a wide variety of developmental and metabolic processes. We are particularly interested in characterizing two Ig superfamily receptors neogenin and L1. The first chapter of the thesis gives a brief review of the biological significance of neogenin and L1 and what has been learned in their functions. In Chapter 2, we describe the localization of the hemojuvelin-binding epitope of neogenin to the membrane proximal fifth and sixth fibronectin type III (FNIII) domains, with the sixth FNIII domain contributing the majority of the binding. Chapter 3 presents the crystal structure of this hemojuvelin-binding fragment at 1.8 Å, revealing a nearly linear domain arrangement. Hemojuvelin binding sites have been mapped to one face of the sixth FNIII domain based on sequence alignment between neogenin and DCC (Deleted in Colorectal Cancer), a molecule related to neogenin but does not bind to hemojuvelin. These results should also be informative in understanding the interaction between neogenin and repulsive guidance molecule (RGM), the closest homologue of hemojuvelin. The interaction between neogenin and RGM is known to regulate neuronal survival. Chapter 4, the second part of the thesis, describes our studies of L1-mediated homophilic adhesion using biophysical approaches. We built a basis shape model to describe L1-mediated homophilic adhesion between L1-coated giant unilamellar vesicles and flat substrate. Using confocal microscopy techniques, we were able to reconstruct the three-dimensional shape of an adhered vesicle. We developed an algorithm in order to derive adhesion strength from the configurations of adhered vesicles based on our basis shape model using energy minimization approach.

TABLE OF CONTENTS

LIST OF FIGURES AND TABLES

Chapter 1:
Introduction

Immunoglobulin (Ig) superfamily molecules

The concept of the immunoglobulin superfamily originated from the observation that domains within a variety of proteins share sequence similarity with immunoglobulin constant and variable domains, and such domains may have evolved from a common ancestral protein of ~100 amino acids in length (*1*). Initially, Ig or Ig-like domains were identified based on sequence similarity, but as more 3-D structures became available, this criterion was replaced by similarity based on structural features, which greatly broadened the definition of the superfamily. A typical Ig-like domain (Figure 1) has a sandwich-like fold formed by two sheets of antiparallel beta strands, and often a conserved disulfide bond between two cysteines, and an "invariant" tryptophan residue (*1*).

Most Ig superfamily molecules are located on cell surface, with exceptions including the secreted forms of antibodies. The most common functions of Ig superfamily receptors are adhesion/recognition and initiation of signaling cascade in the cytoplasm (*1*). One group of Ig superfamily receptors consists of tandem Ig-like domains followed by fibronectin type III (FNIII) domains, which is a common structure motif originally found in fibronectin (*2*). Both FNIII domains and Ig-like domains belong to the Greek key superfold (*3*), but the sequence similarity between these types of domains is usually quite low. The folding topology of a FNIII domain strongly resembles the IgC2 domain, but lacks the disulfide bond linking the two opposed beta sheets (*3*). Adhesion complexes formed by Ig superfamily molecules are not just static. Instead they are capable of sensing the signal from the extracellular space and modulating cellular activities (*4*).

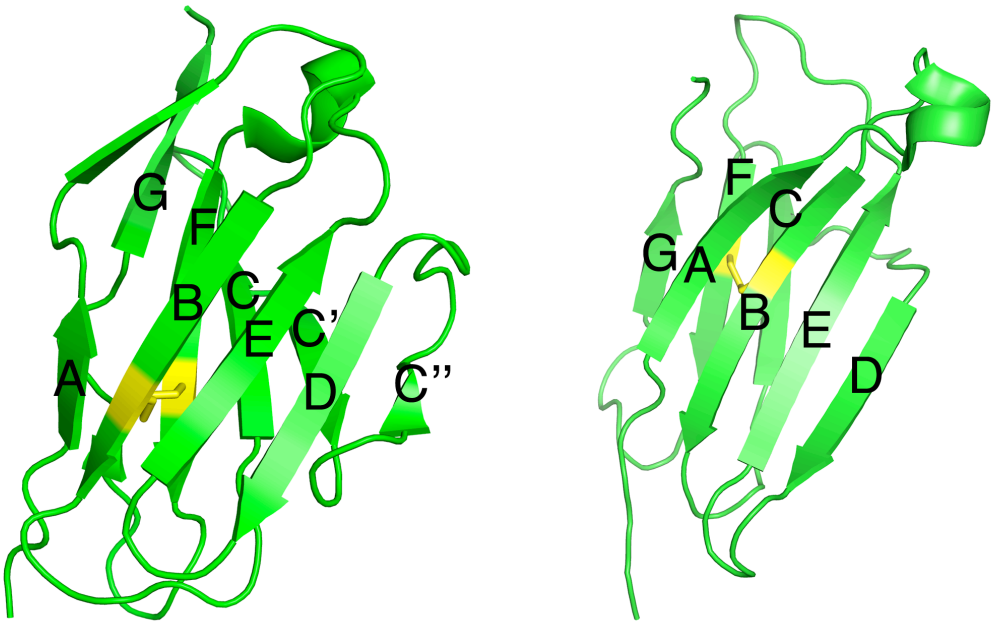

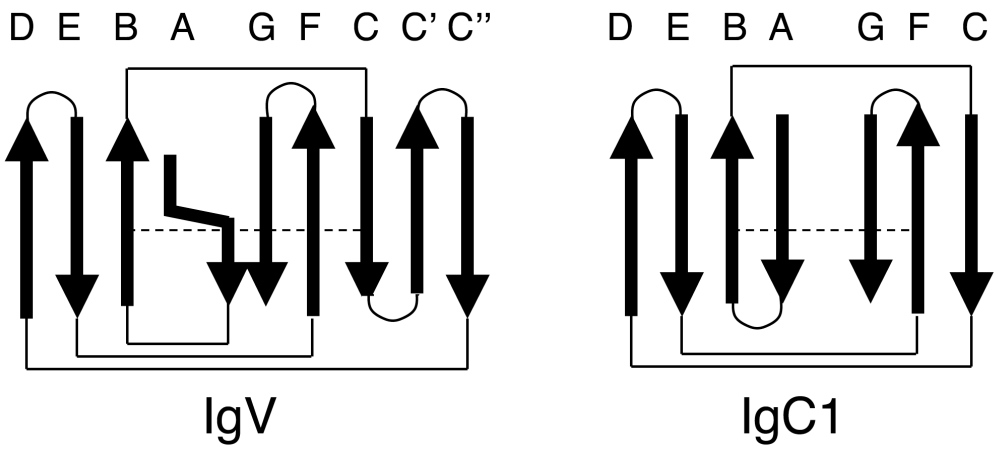

IgV IgC1

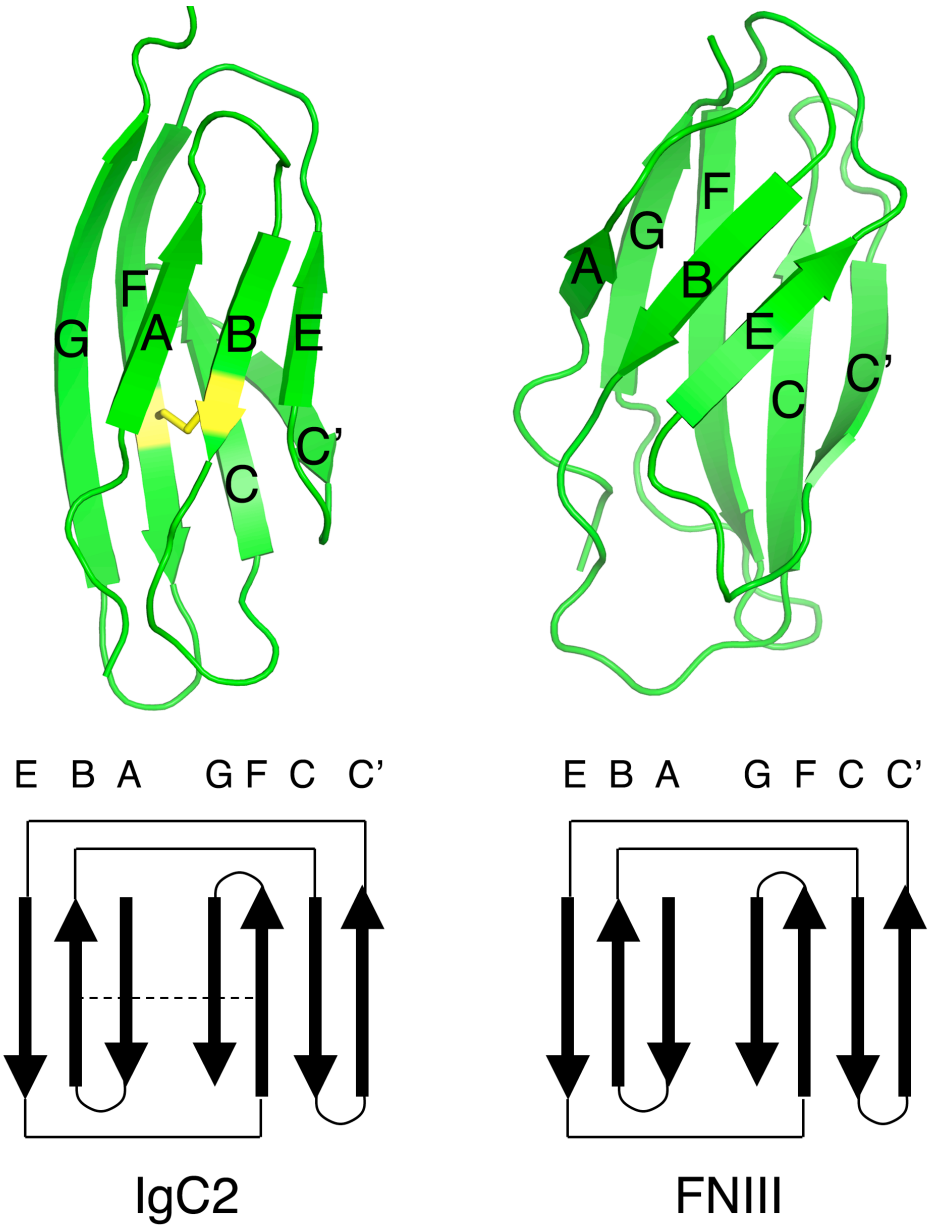

Figure 1. Ribbon and topology diagrams of typical Ig folds and FNIII fold. Disulfide bonds are shown as yellow sticks in ribbon diagram and dashed lines in topology diagram. The IgV and IgC1 domains are found in the immunoglobulin variable and constant regions, respectively. IgC2 domain shares sequence similarity to IgV but topologically looks like IgC1. FNIII domain has the same domain arrangement as the IgC2 but without the disulfide bond. PDB IDs used are 1YQV, 2YXF, 1HNF, and 1QR4.

Many Ig superfamily proteins function as adhesion molecules in the nervous system and they have been implicated in various roles during the development of the nervous system (*5*). Based on the composition of their extracellular domains, neural cell adhesion molecules of the Ig superfamily (IgCAMs) can be divided in three groups: containing Ig folds only, containing Ig folds followed by FNIII domain(s), and Ig folds linked to protein modules other than an FNIII domain. Figure 2 shows a schematic view of several neural cell adhesion molecules of the Ig superfamily, including the most extensively characterized proteins NCAM, L1, and DCC/neogenin. IgCAMs are known to interact with themselves (homophilic binding) and with other proteins (heterophilic binding), which can be other IgCAMs (*6*).

The thesis work described here is the characterization of the Ig superfamily receptors neogenin and L1 using biochemical and biophysical approaches. Although neogenin and L1 are both neural adhesion molecules of the Ig superfamily, neogenin interacts with a broader range of ligands and function in multiple aspects of development and metabolism other than CNS development, for example, iron homeostasis (*7*). Here we present studies aimed at elucidating the role of neogenin in the mammalian iron-regulatory network through its interactions with hemojuvelin. Chapter 2 presents the mapping of the hemojuvelin-binding epitope on neogenin and Chapter 3 presents the crystal structure of the hemojuvelin-binding fragment of neogenin and comparison with existing tandem FNIII domain structures. These results are also relevant to interactions between neogenin and repulsive guidance molecules (RGMs), which regulate neuronal survival and are related to hemojuvelin. The second part of the thesis describes a

biophysical approach to studying L1-mediated homophilic adhesion using L1 reconstituted into liposomes.

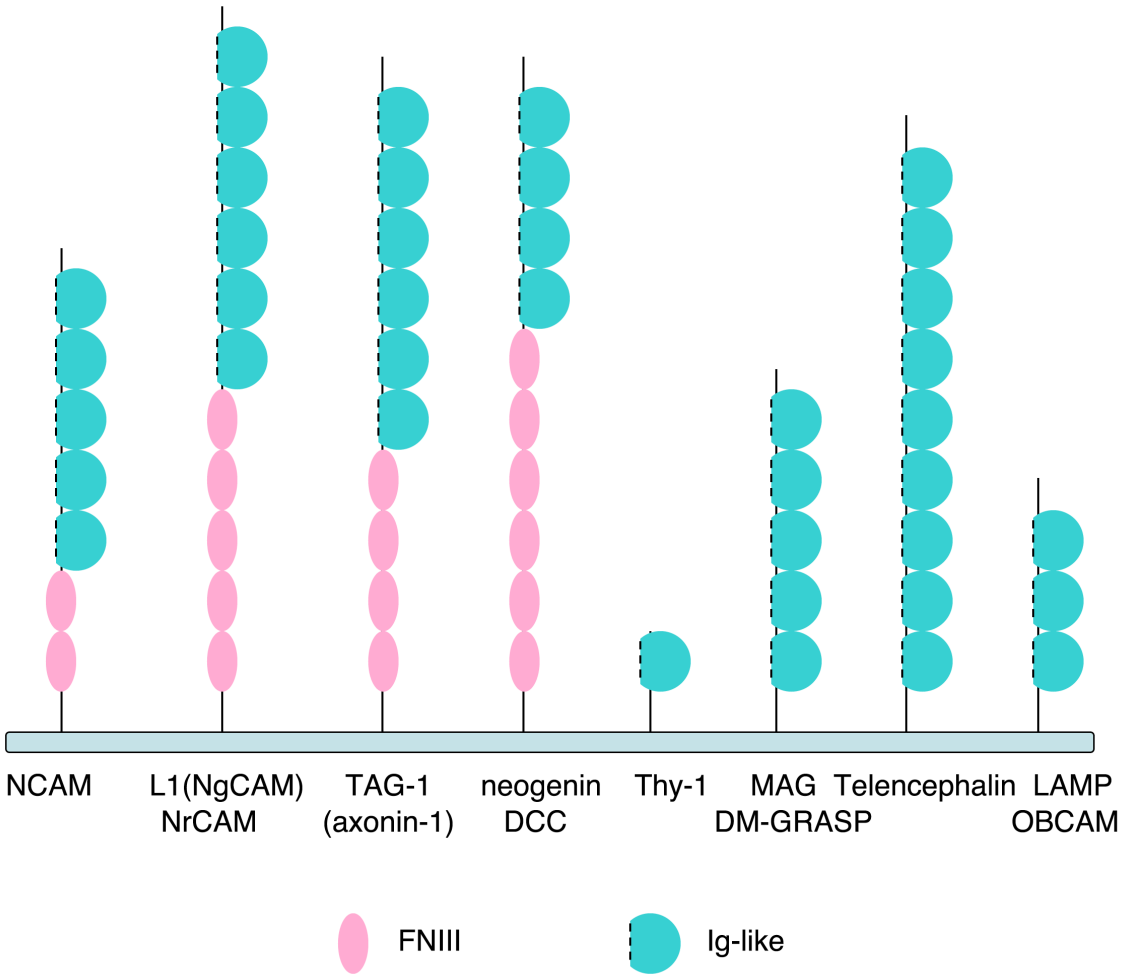

Figure 2. Neural adhesion molecules of the Ig superfamily. Proteins composed of Ig-like domains connected to FNIII domains (left) and proteins composed of Ig-like domains alone (right) are included. Ig superfamily proteins with Ig-like domains linked to motifs other than FNIII fold are not shown. Synonymous names are in parentheses. These molecules are associated with the membrane either by a single transmembrane segment or a glycosylphosphatidylinisotol (GPI)-anchor. For a more detailed list of Ig superfamily neural adhesion molecules, see reference (*5*).

Iron homeostasis

Iron is essential to almost all organisms on earth. The conversion between ferric (Fe^{3+}) and ferrous (Fe^{2+}) states enables it to donate and receive electrons and thus participate in many redox reactions. Well-known iron-containing proteins include the nitrogen fixation enzyme nitrogenase, ferrodoxin in photosynthesis, and the oxygen transporter hemoglobin. In order to maintain a normal level of iron availability and compensate for daily loss, dietary iron is absorbed through the mammalian intestinal epithelium, chelated by transferrin with extremely high affinity, and delivered to the rest of the body through the transferrin/transferrin receptor (Tf/TfR) system via a receptor-mediated endocytosis (*8*). Iron-loaded Tf undergoes a pH-dependent conformation change in the acidic environment of intracellular early endosomes and releases the iron for cellular usage or storage in ferritin, within which iron is kept in a non-toxic form and can be released for later application.

Ionic iron has the potential to initiate lipid peroxidation, a free radical chain reaction involving molecular oxygen that can lead to cell death. Therefore, iron usually exists in a tightly coordinated form such as within a heme or iron-sulfur cluster rather than the free ionic form. Mammals have evolved a complicated iron regulatory pathway in order to handle iron in a safe manner (*9*). Strict regulation of iron not only prevents it from damaging cellular structures, but also limits its availability to bacteria, thus preventing infection-induced inflammation. Dysfunction of regulation can lead to iron deficiency or iron overload, also known as hemochromatosis, which can result in severe damage to the liver, heart, and pancreas, and in the worst cases, organ failure (*10*).

Over the past two decades, many molecules in the iron-regulatory network have been identified, including HFE (*11*), transferrin receptor 2 (TfR2)(*12*), ferroportin (*13-16*), hepcidin (*17-19*), and hemojuvelin (*20*). Among these molecules, hepcidin, an anti-microbial peptide hormone secreted predominantly by liver, is the principal iron regulator (*21*). Hepcidin controls iron flux through binding and inducing internalization and degradation of ferroportin, the only known membrane iron exporter highly expressed in duodenal cells, hepatocytes, macrophages, and placental cells (*22*). Elevation in hepcidin expression prevents dietary iron uptake as well as iron efflux to the plasma and can lead to anemia. On the other hand, insufficient hepcidin production due to mutation in the hepcidin gene or its upstream regulators (HFE, TfR2, and hemojuvelin) results in most causes of hereditary hemochromatosis (*21*).

The hemochromatosis protein HFE is type I transmembrane protein and related to class I major histocompatibility complex (MHC) molecules, but lacking their peptide binding ability (*23*). HFE competes with iron-loaded Tf, the whole body iron status flag, for binding to TfR (*24, 25*). HFE also interacts with TfR2, a type II transmembrane protein with an N-terminal cytoplasmic domain and a large ectodomain homologous to TfR. TfR2 does bind iron-loaded Tf (*26*), and has been suggested to serve more as a sensor for body iron status than in Tf uptake (*27*). Despite the considerable sequence similarity between TfR and TfR2, HFE binds at different locations on these two molecules: the ectodomain in the case of TfR and the transmembrane region in the care of TfR2 (*28, 29*). Since HFE does not have any identifiable internalization sequence in its cytoplasmic domain, the TfR2/HFE interaction was proposed to transduce signals through the TfR2 intracellular domain when serum iron saturation is changed (*30*).

Compared with HFE and TfR2, the role of hemojuvelin in regulating hepcidin level is better understood thanks to growing information in recent years.

Iron regulatory protein hemojuvelin

In 2004, the *HJV* (originally called *HFE2)* gene*,* encoding the iron-regulatory protein hemojuvelin, was positionally cloned using samples from patients with juvenile hemochromatosis, an early-onset hereditary iron overload disorder (*20*). In HJV knocked-out mice, hepcidin mRNA is almost undetectable (*31*), consistent with the low urine hepcidin concentration in patients with HJV mutations.

Expressed in fetal and adult liver, heart and skeletal muscle, human *HJV* encodes a protein of 426 amino acids, including a secretion signal peptide, a conserved RGD triamino acid motif, a partial von Willebrandt factor domain, and a glycosylphosphatidylinisotol (GPI) anchor for attaching the mature protein to the cell membrane. The closest homologues of hemojuvelin are repulsive guidance molecules (RGMs), which have multiple functions in neural development. Hemojuvelin can undergo a proteolytic cleavage at a conserved Asp-Pro bond and forms two fragments that usually associate together (*32*). This feature was also observed in mouse and chick RGM family members (*32*). Hemojuvelin can exist in both soluble and membrane-associated forms. Soluble hemojuvelin is found in serum, serving as a competitor with its membrane-bound counterpart in a dose-dependent manner in regulating hepcidin expression (*32*).

The Ig superfamily receptor neogenin

Soon after the discovery of hemojuvelin, neogenin, a cell surface receptor belonging to the Ig superfamily, was found to guide axon growth and regulate neuronal survival through interacting with repulsive guidance molecule A (RGMa) (*33, 34*), the closest homolog of hemojuvelin. The high sequence similarity between hemojuvelin and RGMa suggested the possibility that neogenin might also function as the receptor for hemojuvelin, which was confirmed by co-immunoprecipitation experiment (*35*). The disease-causing mutant hemojuvelin G320V does not bind neogenin, indicating that the hemojuvelin-neogenin interaction is critical in iron homeostasis (*35*). Unlike the tissue-specific expression pattern for hemojuvelin, expression of human neogenin appears ubiquitous (*36*), with the highest mRNA level detected in skeletal muscle, one of the few places where hemojuvelin is highly expressed. Since hemojuvelin does not seem to play a major role in muscle morphogenesis (*20*), it has been proposed that the function of the hemojuvelin/neogenin interaction in skeletal muscle is to provide soluble hemojuvelin in serum (*37*).

Neogenin consists of a large ectodomain with four Ig-like domains and six FNIII domains, a transmembrane region and an intracellular domain (*38*). Sharing nearly 50% sequence identity, neogenin is closely related to the DCC (Deleted in Colorectal Cancer) protein. Both neogenin and DCC function as receptors for netrins, a group of proteins playing fundamental roles in the development of nervous system (*39, 40*). Neogenin is also involved in a broad range of developmental and metabolic processes. In addition to interacting with RGMs and netrin in axon guidance in the brain, neogenin is also critical in establishing organ architectures (*41*), in stimulating myogenic differentiation (*42*) and promoting mammary gland morphogenesis (*40*).

We initiated biochemical studies of the hemojuvelin/neogenin interaction to elucidate the mechanism of the interaction on the molecular level. The stoichiometry of the binding was found to be 1:1 and the hemojuvelin-binding epitope was mapped to the membrane-proximal FNIII 5-6 domains on neogenin as described in Chapter 2. In collaboration with Dr. An-Sheng Zhang in the Enns group at Oregon Health and Sciences University, we proved that this fragment is as effective as the intact neogenin ectodomain in competing with cell membrane neogenin both *in vitro* (Appendix A) and *in vivo* (Appendix B). The crystal structure of this hemojuvelin-binding fragment was solved and presented in Chapter 3. However, attempts to crystallize hemojuvelin alone and hemojuvelin/neogenin complexes have not yet been successful.

Hemojuvelin-assisted bone morphogenetic protein pathway

Belonging to the transforming growth factor β (TGF-β) superfamily, bone morphogenetic proteins (BMPs) are a group of secreted molecules that play important roles in the cell growth, differentiation, and apoptosis throughout the animal kingdom (*43*). Originally identified as inducer of bone formation *in vivo* when injected in mice, BMPs have been intensively studied after the cloning of the human BMP-2 gene in late 1980s (*44*). Like other molecules in the TGF-β superfamily, BMPs are synthesized as large precursors, which later become glycosylated and processed to form single disulfide bond-linked dimer with each polypeptide chain containing the C-terminal 114 residues of the propeptide (*45*).

Significant advances concerning the functions of BMPs and the receptor mediated signal transduction pathway have been achieved in recent years (*46*). Classic BMP

pathway is initiated by the binding of the ligand on the plasma membrane, inducing the heterodimerization of type I and type II transmembrane serine/threoinine kinase receptors, which in turn activates the Smad proteins by phosyphorylation (*47, 48*). The receptor-activated Smad will then recruit another protein called Smad4 and translocate into nucleus to regulate the transcription of target genes (*47, 48*). There are several different type I and type II receptors and their combination determines the molecules subsequently involved in the signal transduction (*47*).

An important advance in the iron field occurred in 2006, when hemojuvelin was identified as the co-receptor for BMP (*49*). Evidences showed that hemojuvelin-aided BMP signaling triggers hepcidin expression through the classic Smad1/5/8 activation upon binding of BMP to its type I and type II receptors (*49*). This pathway was found to be independent of other iron-regulatory proteins such as HFE, TfR2, and Interleukin-6 (IL-6) (*50*). BMP-responsive elements, STAT, and bZIP/HNF4/COUP motifs, were located in the promoter of hepcidin by two groups independently (*51, 52*). BMP-6 was then identified as the central endogenous regulator of hepcidin expression among all BMP family proteins *in vivo* and the phenotype of *BMP-6* null mice resembles hereditary hemochromatosis (*53*).

The major players in hemojuvelin-related hepcidin expression are depicted in Figure 3. How does neogenin fit into the picture of hemojuvelin-mediated BMP signaling? Shedding of hemojuvelin from cell membrane was observed to be responsive to the concentration of iron-loaded transferrin and hemojuvelin shedding is mediated by neogenin and independent of BMP or its antagonist (*37*). The group that initially discovered hemojuvelin as a co-receptor for BMPs claimed that hemojuvelin signaled

hepcidin expression only through a subset of BMP ligands (BMP-2, BMP-4, and BMP-6) and BMP receptors, and that this process was independent of neogenin (*54*). However, another study showed that neogenin-hemojuvelin interaction was critical in BMP-4-induced hepcidin expression (*55*), contradicting the previous conclusion. We also discovered that neogenin and BMP-2 do not bind to hemojuvelin at overlapping site (see Chapter 2), supporting the possibility that neogenin is part of the multi-protein complex that initiates the intracellular signaling that ultimately leads to hepcidin expression (*56*). Most recently, a third group succeeded in making neogenin$^{-/-}$ mice that exhibit iron overload, impaired BMP signaling and low levels of hepcidin (*57*). These researchers argued that neogenin regulates hemojuvelin/BMP-induced hepcidin expression through stabilizing GPI-anchored hemojuvelin and inhibiting hemojuvelin secretion.

Another way that neogenin may be involved in signaling is through the cleavage and translocation of its intracellular domain, which was suggested in a recent report (*58*). However, this study focused on the role of neogenin in axon guidance via interaction with the neuronal RGMa protein and thus does not directly address the questions in iron regulation, which mostly takes place in the liver. The exact role of neogenin in this pathway remains to be elucidated.

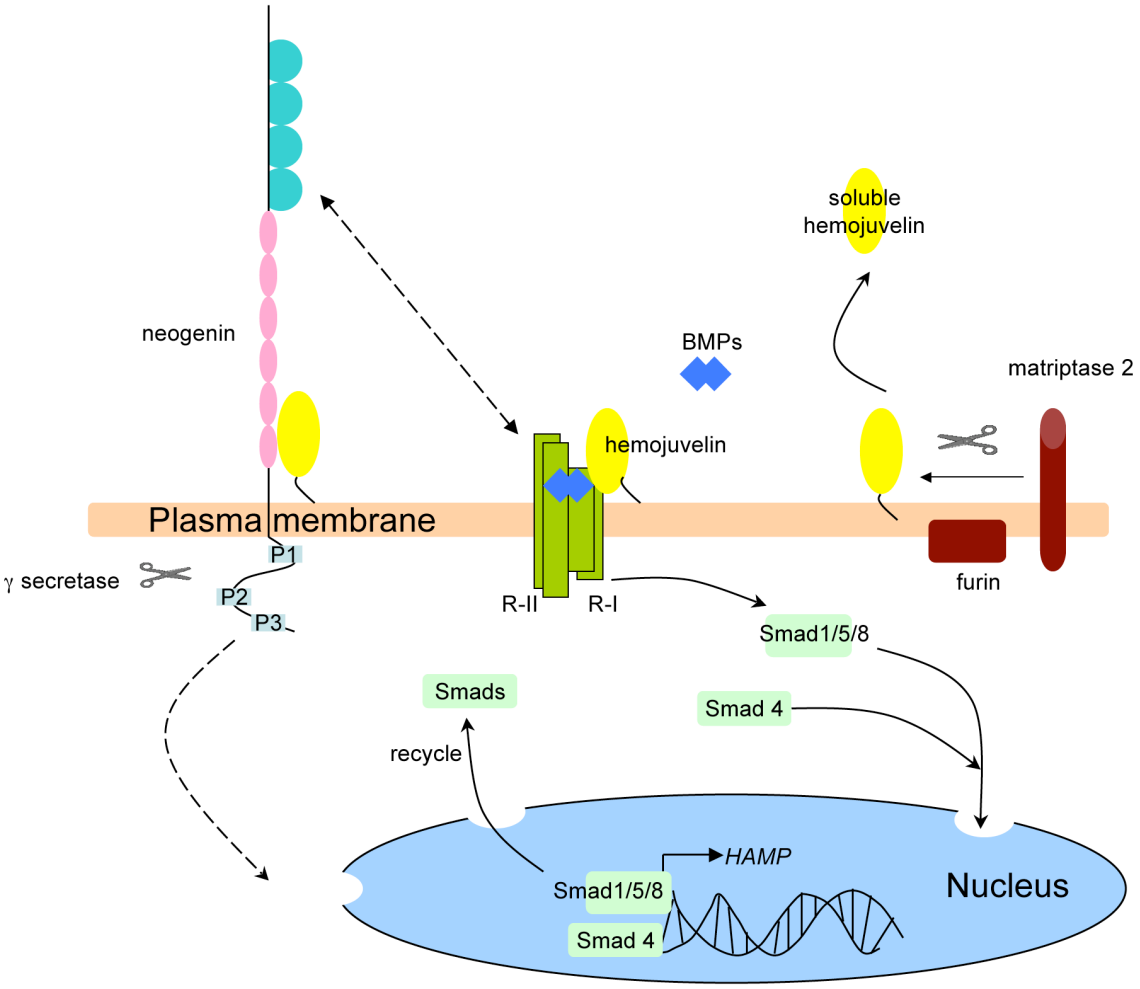

Figure 3. Molecular network of hemojuvelin-induced hepcidin expression. P1, P2 and P3 are the conserved regions on neogenin intracellular domain. R-I and R-II are type I and type II transmembrane serine/threoinine kinase receptors for BMP. γ-secretase is responsible for releasing the intracellular domain of neogenin to the cytosol. Two dashed lines indicate potential interaction or pathway suggested by previous studies (*56, 58*).

Neural cell adhesion molecule L1

The L1 gene is located on the X-chromosome (*59*) and mutations in the L1 gene are associated with a broad spectrum of neurological diseases (*60*) including mental retardation (*61*), MASA syndrome (*62*), X-linked hydrocephalus (*63*), impairment of sensorimotor gating (*64*). The positions of these pathological mutations were mapped onto a structural model of the L1 ectodomain (*65*), based on the crystal structures of domains in telokin (*66*) and neuroglian (*67*), where the latter is the *Drosophila* homologue of human L1. Over half of the mutations are clustered at N-termini of individual domains as well as the C-D strand region on the Ig-like domain, potentially causing the phenotype by destabilizing the protein (*65*).

Primarily expressed in the developing and adult nervous system, L1 consists of six Ig-like domains, five FNIII domains, a single transmembrane domain and a cytoplasmic tail of just over 100 amino acids (*68*) (Figure 2). The multi-domain structure of L1 enables it to interact with distinct partners such as integrins, fibroblast growth factor receptor and other cell adhesion molecules (*69*), resulting in dynamic regulation of cell adhesion in response to different ligands. The cytoplasmic domain of L1 contains a conserved region capable of binding to the cytoskeletal protein ankyrin (*68*), and a conserved tyrosine residue within this region was found to control binding by its phosphorylation (*70*). Downstream signaling induced by L1 after ankyrin binding is complicated, including recruitment of the microtubule-associated protein doublecortin (DCX) and sequential activation of a series of kinases (*69, 71, 72*).

L1-mediated homophilic adhesion

How L1 achieves homophilic adhesion has been under intensive study for many years. The first four Ig domains are critical in homophilic adhesion and neurite outgrowth but the potency of molecules containing only these domains is lower than the intact molecule (*73*). Based on existing crystal structures of the L1 homologues hemolin (*74*) and axonin-1 (*75*), the first four Ig domains of L1 are believed to form a horseshoe-shaped structure, with the first and second Ig domains folding back to interact with the third and fourth Ig domains. The FNIII domain region of the molecule appears to adopt a relatively extended conformation (*76*).

Severals models have been proposed to predict how the horseshoe pairs arrange with respect to each other in homophilic adhesion. Previous models, including a domain swapping model (*74*) and a zipper model (*75*), were based on crystal structures of proteins closely related to L1. Regularly spaced adhesion spots were observed in the more recent electron tomography studies and it was proposed that the separation distance is controlled by interactions either between negatively charged carbohydrates and positive surfaces of the neighboring protein or between uncharged carbohydrate pairs (*77*).

Giant unilamellar vesicle as model membranes

We sought to address some thermodynamic and kinetic issues related to L1-mediated homophilic adhesion. For example, what is the average adhesion energy for one pair of L1 molecules or the energy for a given L1 density? Is there cooperativity in L1-mediated adhesion? Does the adhesion zone actively recruit L1 from other regions of a

membrane? In order to address these questions, we used L1 incoporated into giant unilamellar vesicles as the experimental platform.

As an essential component of all biomembranes, the lipid bilayer has the unique feature of two-dimensional fluidity, which is critical in lipid/protein diffusion, distribution, and local enrichment (*78, 79*). Due to the complex nature of biomembranes in cells, researchers have used lipid model systems to understand basic membrane activities (*80*). These cell-free assays make it possible to track down essential components of the membrane trafficking processes and distinguish the order of events, while at the same time preserving the two-dimensional fluidity of cellular membranes. One of the most broadly used model membranes is spherical liposome, also known as vesicle. Many methods have been established to prepare liposomes using natural or synthetic lipids while varying the chemical composition of the lipid bilayer. Giant unilamellar vesicles (GUVs) are particularly of interest due to their cell-size dimensions (*81*). Although the observations from these *in vitro* experiments involving GUVs does not always translate into what happens in cells because cellular membranes are more rigid due the cytoskeleton, they often provide great insight essential to understanding events taking places on these membranes at a molecular level (*82, 83*). Chapter 4 summarizes our work on L1-mediated homophilic adhesion using both theoretical and experimental approaches involving GUVs.

References:

1. Williams, A. F., and Barclay, A. N. (1988) The immunoglobulin superfamily domains for cell surface recognition, *Annu Rev Immunol 6*, 381-405.

2. Kornblihtt, A. R., Umezawa, K., Vibe-Pedersen, K., and Baralle, F. E. (1985) Primary structure of human fibronectin: differential splicing may generate at least 10 polypeptides from a single gene, *EMBO J 4*, 1755-1759.

3. Vaughn, D. E., and Bjorkman, P. J. (1996) The (Greek) key to structures of neural adhesion molecules, *Neuron 16*, 261-273.

4. Aplin, A. E., Howe, A., Alahari, S. K., and Juliano, R. L. (1998) Signal transduction and signal modulation by cell adhesion receptors: the role of integrins, cadherins, immunoglobulin-cell adhesion molecules, and selectins, *Pharmacol Rev 50*, 197-263.

5. Brummendorf, T., and Rathjen, F. G. (1996) Structure/function relationships of axon-associated adhesion receptors of the immunoglobulin superfamily, *Curr Opin Neurobiol 6*, 584-593.

6. Rougon, G., and Hobert, O. (2003) New insights into the diversity and function of neuronal immunoglobulin superfamily molecules, *Annu Rev Neurosci 26*, 207-238.

7. Wilson, N. H., and Key, B. (2007) Neogenin: one receptor, many functions, *Int J Biochem Cell Biol 39*, 874-878.

8. Andrews, N. C. (2000) Iron homeostasis: insights from genetics and animal models, *Nat Rev Genet 1*, 208-217.

9. Hentze, M. W., Muckenthaler, M. U., and Andrews, N. C. (2004) Balancing acts: molecular control of mammalian iron metabolism, *Cell 117*, 285-297.

10. Pietrangelo, A. (2004) Medical progress - Hereditary hemochromatosis - A new look at an old disease, *New Engl J Med 350*, 2383-2397.

11. Feder, J. N., Gnirke, A., Thomas, W., Tsuchihashi, Z., Ruddy, D. A., Basava, A., Dormishian, F., Domingo, R., Ellis, M. C., Fullan, A., Hinton, L. M., Jones, N. L., Kimmel, B. E., Kronmal, G. S., Lauer, P., Lee, V. K., Loeb, D. B., Mapa, F. A., McClelland, E., Meyer, N. C., Mintier, G. A., Moeller, N., Moore, T., Morikang, E., Prass, C. E., Quintana, L., Starnes, S. M., Schatzman, R. C., Brunke, K. J., Drayna, D. T., Risch, N. J., Bacon, B. R., and Wolff, R. K. (1996) A novel MHC class I-like gene is mutated in patients with hereditary haemochromatosis, *Nature Genetics 13*, 399-408.

12. Camaschella, C., Roetto, A., Cali, A., De Gobbi, M., Garozzo, G., Carella, M., Majorano, N., Totaro, A., and Gasparini, P. (2000) The gene TFR2 is mutated in a new type of haemochromatosis mapping to 7q22, *Nature Genetics 25*, 14-15.

13. Abboud, S., and Haile, D. J. (2000) A novel mammalian iron-regulated protein involved in intracellular iron metabolism, *Journal of Biological Chemistry 275*, 19906-19912.

14. Donovan, A., Brownlie, A., Zhou, Y., Shepard, J., Pratt, S. J., Moynihan, J., Paw, B. H., Drejer, A., Barut, B., Zapata, A., Law, T. C., Brugnara, C., Kingsley, P. D., Palis, J., Fleming, M. D., Andrews, N. C., and Zon, L. I. (2000) Positional cloning of zebrafish ferroportin1 identifies a conserved vertebrate iron exporter, *Nature 403*, 776-781.

15. McKie, A. T., Marciani, P., Rolfs, A., Brennan, K., Wehr, K., Barrow, D., Miret, S., Bomford, A., Peters, T. J., Farzaneh, F., Hediger, M. A., Hentze, M. W., and Simpson, R. J. (2000) A novel duodenal iron-regulated transporter, IREG1, implicated in the basolateral transfer of iron to the circulation, *Mol Cell 5*, 299-309.

16. Njajou, O. T., Vaessen, N., Joosse, M., Berghuis, B., van Dongen, J. W. F., Breuning, M. H., Snijders, P. J. L. M., Rutten, W. P. F., Sandkuijl, L. A., Oostra, B. A., van Duijn, C. M., and Heutink, P. (2001) A mutation in SLC11A3 is associated with autosomal dominant hemochromatosis, *Nature Genetics 28*, 213-214.

17. Krause, A., Neitz, S., Magert, H. J., Schulz, A., Forssmann, W. G., Schulz-Knappe, P., and Adermann, K. (2000) LEAP-1, a novel highly disulfide-bonded human peptide, exhibits antimicrobial activity, *Febs Lett 480*, 147-150.

18. Park, C. H., Valore, E. V., Waring, A. J., and Ganz, T. (2001) Hepcidin, a urinary antimicrobial peptide synthesized in the liver, *Journal of Biological Chemistry 276*, 7806-7810.

19. Roetto, A., Papanikolaou, G., Politou, M., Alberti, F., Girelli, D., Christakis, J., Loukopoulos, D., and Camaschella, C. (2003) Mutant antimicrobial peptide hepcidin is associated with severe juvenile hemochromatosis, *Nature Genetics 33*, 21-22.

20. Papanikolaou, G., Samuels, M. E., Ludwig, E. H., MacDonald, M. L., Franchini, P. L., Dube, M. P., Andres, L., MacFarlane, J., Sakellaropoulos, N., Politou, M., Nemeth, E., Thompson, J., Risler, J. K., Zaborowska, C., Babakaiff, R., Radomski, C. C., Pape, T. D., Davidas, O., Christakis, J., Brissot, P., Lockitch, G., Ganz, T., Hayden, M. R., and Goldberg, Y. P. (2004) Mutations in HFE2 cause iron overload in chromosome 1q-linked juvenile hemochromatosis, *Nat Genet 36*, 77-82.

21. Lee, P. L., and Beutler, E. (2009) Regulation of hepcidin and iron-overload disease, *Annu Rev Pathol 4*, 489-515.

22. Nemeth, E., and Ganz, T. (2006) Regulation of iron metabolism by hepcidin, *Annu Rev Nutr 26*, 323-342.

23. Lebron, J. A., Bennett, M. J., Vaughn, D. E., Chirino, A. J., Snow, P. M., Mintier, G. A., Feder, J. N., and Bjorkman, P. J. (1998) Crystal structure of the hemochromatosis protein HFE and characterization of its interaction with transferrin receptor, *Cell 93*, 111-123.

24. Lebron, J. A., West, A. P., Jr., and Bjorkman, P. J. (1999) The hemochromatosis protein HFE competes with transferrin for binding to the transferrin receptor, *J Mol Biol 294*, 239-245.

25. West, A. P., Jr., Giannetti, A. M., Herr, A. B., Bennett, M. J., Nangiana, J. S., Pierce, J. R., Weiner, L. P., Snow, P. M., and Bjorkman, P. J. (2001) Mutational analysis of the transferrin receptor reveals overlapping HFE and transferrin binding sites, *J Mol Biol 313*, 385-397.

26. Kawabata, H., Yang, R., Hirama, T., Vuong, P. T., Kawano, S., Gombart, A. F., and Koeffler, H. P. (1999) Molecular cloning of transferrin receptor 2. A new member of the transferrin receptor-like family, *J Biol Chem 274*, 20826-20832.

27. Andrews, N. C. (2008) Forging a field: the golden age of iron biology, *Blood 112*, 219-230.

28. Bennett, M. J., Lebron, J. A., and Bjorkman, P. J. (2000) Crystal structure of the hereditary haemochromatosis protein HFE complexed with transferrin receptor, *Nature 403*, 46-53.

29. Chen, J., Chloupkova, M., Gao, J., Chapman-Arvedson, T. L., and Enns, C. A. (2007) HFE modulates transferrin receptor 2 levels in hepatoma cells via interactions that differ from transferrin receptor 1-HFE interactions, *J Biol Chem 282*, 36862-36870.

30. Goswami, T., and Andrews, N. C. (2006) Hereditary hemochromatosis protein, HFE, interaction with transferrin receptor 2 suggests a molecular mechanism for mammalian iron sensing, *J Biol Chem 281*, 28494-28498.

31. Huang, F. W., Pinkus, J. L., Pinkus, G. S., Fleming, M. D., and Andrews, N. C. (2005) A mouse model of juvenile hemochromatosis, *J Clin Invest 115*, 2187-2191.

32. Lin, L., Goldberg, Y. P., and Ganz, T. (2005) Competitive regulation of hepcidin mRNA by soluble and cell-associated hemojuvelin, *Blood 106*, 2884-2889.

33. Matsunaga, E., Tauszig-Delamasure, S., Monnier, P. P., Mueller, B. K., Strittmatter, S. M., Mehlen, P., and Chedotal, A. (2004) RGM and its receptor neogenin regulate neuronal survival, *Nat Cell Biol 6*, 749-755.

34. Rajagopalan, S., Deitinghoff, L., Davis, D., Conrad, S., Skutella, T., Chedotal, A., Mueller, B. K., and Strittmatter, S. M. (2004) Neogenin mediates the action of repulsive guidance molecule, *Nat Cell Biol 6*, 756-762.

35. Zhang, A. S., West, A. P., Jr., Wyman, A. E., Bjorkman, P. J., and Enns, C. A. (2005) Interaction of hemojuvelin with neogenin results in iron accumulation in human embryonic kidney 293 cells, *J Biol Chem 280*, 33885-33894.

36. Meyerhardt, J. A., Look, A. T., Bigner, S. H., and Fearon, E. R. (1997) Identification and characterization of neogenin, a DCC-related gene, *Oncogene 14*, 1129-1136.

37. Zhang, A. S., Anderson, S. A., Meyers, K. R., Hernandez, C., Eisenstein, R. S., and Enns, C. A. (2007) Evidence that inhibition of hemojuvelin shedding in response to iron is mediated through neogenin, *J Biol Chem 282*, 12547-12556.

38. Vielmetter, J., Chen, X. N., Miskevich, F., Lane, R. P., Yamakawa, K., Korenberg, J. R., and Dreyer, W. J. (1997) Molecular characterization of human neogenin, a DCC-related protein, and the mapping of its gene (NEO1) to chromosomal position 15q22.3-q23, *Genomics 41*, 414-421.

39. Keino-Masu, K., Masu, M., Hinck, L., Leonardo, E. D., Chan, S. S., Culotti, J. G., and Tessier-Lavigne, M. (1996) Deleted in Colorectal Cancer (DCC) encodes a netrin receptor, *Cell 87*, 175-185.

40. Srinivasan, K., Strickland, P., Valdes, A., Shin, G. C., and Hinck, L. (2003) Netrin-1/neogenin interaction stabilizes multipotent progenitor cap cells during mammary gland morphogenesis, *Dev Cell 4*, 371-382.

41. Fitzgerald, D. P., Seaman, C., and Cooper, H. M. (2006) Localization of Neogenin protein during morphogenesis in the mouse embryo, *Dev Dyn 235*, 1720-1725.

42. Kang, J. S., Yi, M. J., Zhang, W., Feinleib, J. L., Cole, F., and Krauss, R. S. (2004) Netrins and neogenin promote myotube formation, *J Cell Biol 167*, 493-504.

43. Hogan, B. L. (1996) Bone morphogenetic proteins: multifunctional regulators of vertebrate development, *Genes Dev 10*, 1580-1594.

44. Wozney, J. M., Rosen, V., Celeste, A. J., Mitsock, L. M., Whitters, M. J., Kriz, R. W., Hewick, R. M., and Wang, E. A. (1988) Novel regulators of bone formation: molecular clones and activities, *Science 242*, 1528-1534.

45. Chen, D., Zhao, M., and Mundy, G. R. (2004) Bone morphogenetic proteins, *Growth Factors 22*, 233-241.

46. von Bubnoff, A., and Cho, K. W. (2001) Intracellular BMP signaling regulation in vertebrates: pathway or network?, *Dev Biol 239*, 1-14.

47. Massague, J. (2000) How cells read TGF-beta signals, *Nat Rev Mol Cell Biol 1*, 169-178.

48. Derynck, R., and Zhang, Y. E. (2003) Smad-dependent and Smad-independent pathways in TGF-beta family signalling, *Nature 425*, 577-584.

49. Babitt, J. L., Huang, F. W., Wrighting, D. M., Xia, Y., Sidis, Y., Samad, T. A., Campagna, J. A., Chung, R. T., Schneyer, A. L., Woolf, C. J., Andrews, N. C., and Lin, H. Y. (2006) Bone morphogenetic protein signaling by hemojuvelin regulates hepcidin expression, *Nat Genet 38*, 531-539.

50. Truksa, J., Peng, H. F., Lee, P., and Beutler, E. (2006) Bone morphogenetic proteins 2, 4, and 9 stimulate murine hepcidin 1 expression independently of Hfe, transferrin receptor 2 (Tfr2), and IL-6, *P Natl Acad Sci USA 103*, 10289-10293.

51. Casanovas, G., Mleczko-Sanecka, K., Altamura, S., Hentze, M. W., and Muckenthaler, M. U. (2009) Bone morphogenetic protein (BMP)-responsive elements located in the proximal and distal hepcidin promoter are critical for its response to HJV/BMP/SMAD, *J Mol Med-Jmm 87*, 471-480.

52. Truksa, J., Lee, P., and Beutler, E. (2009) Two BMP responsive elements, STAT, and bZIP/HNF4/COUP motifs of the hepcidin promoter are critical for BMP, SMAD1, and HJV responsiveness, *Blood 113*, 688-695.

53. Andriopoulos, B., Jr., Corradini, E., Xia, Y., Faasse, S. A., Chen, S., Grgurevic, L., Knutson, M. D., Pietrangelo, A., Vukicevic, S., Lin, H. Y., and Babitt, J. L. (2009) BMP6 is a key endogenous regulator of hepcidin expression and iron metabolism, *Nat Genet 41*, 482-487.

54. Xia, Y., Babitt, J. L., Sidis, Y., Chung, R. T., and Lin, H. Y. (2008) Hemojuvelin regulates hepcidin expression via a selective subset of BMP ligands and receptors independently of neogenin, *Blood 111*, 5195-5204.

55. Zhang, A. S., Yang, F., Wang, J., Tsukamoto, H., and Enns, C. A. (2009) Hemojuvelin-neogenin interaction is required for bone morphogenic protein-4-induced hepcidin expression, *J Biol Chem 284*, 22580-22589.

56. Yang, F., West, A. P., Jr., Allendorph, G. P., Choe, S., and Bjorkman, P. J. (2008) Neogenin interacts with hemojuvelin through its two membrane-proximal fibronectin type III domains, *Biochemistry 47*, 4237-4245.

57. Lee, D. H., Zhou, L. J., Zhou, Z., Xie, J. X., Jung, J. U., Liu, Y., Xi, C. X., Mei, L., and Xiong, W. C. (2010) Neogenin inhibits HJV secretion and regulates BMP-induced hepcidin expression and iron homeostasis, *Blood 115*, 3136-3145.

58. Goldschneider, D., Rama, N., Guix, C., and Mehlen, P. (2008) The neogenin intracellular domain regulates gene transcription via nuclear translocation, *Molecular and Cellular Biology 28*, 4068-4079.

59. Djabali, M., Mattei, M. G., Nguyen, C., Roux, D., Demengeot, J., Denizot, F., Moos, M., Schachner, M., Goridis, C., and Jordan, B. R. (1990) The Gene Encoding L1, a Neural Adhesion Molecule of the Immunoglobulin Family, Is Located on the X-Chromosome in Mouse and Man, *Genomics 7*, 587-593.

60. Kenwrick, S., Watkins, A., and De Angelis, E. (2000) Neural cell recognition molecule L1: relating biological complexity to human disease mutations, *Hum Mol Genet 9*, 879-886.

61. Wong, E. V., Kenwrick, S., Willems, P., and Lemmon, V. (1995) Mutations in the Cell-Adhesion Molecule L1 Cause Mental-Retardation, *Trends Neurosci 18*, 168-172.

62. Jouet, M., Rosenthal, A., Armstrong, G., MacFarlane, J., Stevenson, R., Paterson, J., Metzenberg, A., Ionasescu, V., Temple, K., and Kenwrick, S. (1994) X-linked spastic paraplegia (SPG1), MASA syndrome and X-linked hydrocephalus result from mutations in the L1 gene, *Nat Genet 7*, 402-407.

63. Jouet, M., Strain, L., Bonthron, D., and Kenwrick, S. (1996) Discordant segregation of Xq28 markers and a mutation in the L1 gene in a family with X linked hydrocephalus, *J Med Genet 33*, 248-250.

64. Irintchev, A., Koch, M., Needham, L. K., Maness, P., and Schachner, M. (2004) Impairment of sensorimotor gating in mice deficient in the cell adhesion molecule L1 or its close homologue, CHL1, *Brain Res 1029*, 131-134.

65. Bateman, A., Jouet, M., MacFarlane, J., Du, J. S., Kenwrick, S., and Chothia, C. (1996) Outline structure of the human L1 cell adhesion molecule and the sites where mutations cause neurological disorders, *EMBO J 15*, 6050-6059.

66. Holden, H. M., Ito, M., Hartshorne, D. J., and Rayment, I. (1992) X-Ray Structure Determination of Telokin, the C-Terminal Domain of Myosin Light Chain Kinase, at 2.8 Angstrom Resolution, *Journal of Molecular Biology 227*, 840-851.

67. Huber, A. H., Wang, Y. M., Bieber, A. J., and Bjorkman, P. J. (1994) Crystal structure of tandem type III fibronectin domains from Drosophila neuroglian at 2.0 A, *Neuron 12*, 717-731.

68. Hortsch, M. (1996) The L1 family of neural cell adhesion molecules: old proteins performing new tricks, *Neuron 17*, 587-593.

69. Maness, P. F., and Schachner, M. (2007) Neural recognition molecules of the immunoglobulin superfamily: signaling transducers of axon guidance and neuronal migration, *Nat Neurosci 10*, 19-26.

70. Garver, T. D., Ren, Q., Tuvia, S., and Bennett, V. (1997) Tyrosine phosphorylation at a site highly conserved in the L1 family of cell adhesion molecules abolishes ankyrin binding and increases lateral mobility of neurofascin, *J Cell Biol 137*, 703-714.

71. Schaefer, A. W., Kamiguchi, H., Wong, E. V., Beach, C. M., Landreth, G., and Lemmon, V. (1999) Activation of the MAPK signal cascade by the neural cell adhesion molecule L1 requires L1 internalization, *J Biol Chem 274*, 37965-37973.

72. Schmid, R. S., and Maness, P. F. (2008) L1 and NCAM adhesion molecules as signaling coreceptors in neuronal migration and process outgrowth, *Current Opinion in Neurobiology 18*, 245-250.

73. Haspel, J., Friedlander, D. R., Ivgy-May, N., Chickramane, S., Roonprapunt, C., Chen, S., Schachner, M., and Grumet, M. (2000) Critical and optimal Ig domains for promotion of neurite outgrowth by L1/Ng-CAM, *J Neurobiol 42*, 287-302.

74. Su, X. D., Gastinel, L. N., Vaughn, D. E., Faye, I., Poon, P., and Bjorkman, P. J. (1998) Crystal structure of hemolin: a horseshoe shape with implications for homophilic adhesion, *Science 281*, 991-995.

75. Freigang, J., Proba, K., Leder, L., Diederichs, K., Sonderegger, P., and Welte, W. (2000) The crystal structure of the ligand binding module of axonin-1/TAG-1 suggests a zipper mechanism for neural cell adhesion, *Cell 101*, 425-433.

76. Schurmann, G., Haspel, J., Grumet, M., and Erickson, H. P. (2001) Cell adhesion molecule L1 in folded (horseshoe) and extended conformations, *Mol Biol Cell 12*, 1765-1773.

77. He, Y., Jensen, G. J., and Bjorkman, P. J. (2009) Cryo-electron tomography of homophilic adhesion mediated by the neural cell adhesion molecule L1, *Structure 17*, 460-471.

78. Edidin, M. (2003) Timeline - Lipids on the frontier: a century of cell-membrane bilayers, *Nat Rev Mol Cell Bio 4*, 414-418.

79. Vereb, G., Szollosi, J., Matko, J., Nagy, P., Farkas, T., Vigh, L., Matyus, L., Waldmann, T. A., and Damjanovich, S. (2003) Dynamic, yet structured: The cell membrane three decades after the Singer-Nicolson model, *P Natl Acad Sci USA 100*, 8053-8058.

80. Chan, Y. H., and Boxer, S. G. (2007) Model membrane systems and their applications, *Curr Opin Chem Biol 11*, 581-587.

81. Wesolowska, O., Michalak, K., Maniewska, J., and Hendrich, A. B. (2009) Giant unilamellar vesicles - a perfect tool to visualize phase separation and lipid rafts in model systems, *Acta Biochim Pol 56*, 33-39.

82. Romer, W., Berland, L., Chambon, V., Gaus, K., Windschiegl, B., Tenza, D., Aly, M. R. E., Fraisier, V., Florent, J. C., Perrais, D., Lamaze, C., Raposo, G., Steinem, C., Sens, P., Bassereau, P., and Johannes, L. (2007) Shiga toxin induces tubular membrane invaginations for its uptake into cells, *Nature 450*, 670-U673.

83. Ramamurthi, K. S., Lecuyer, S., Stone, H. A., and Losick, R. (2009) Geometric cue for protein localization in a bacterium, *Science 323*, 1354-1357.

Chapter 2:
Neogenin Interacts with Hemojuvelin through Its Two Membrane-Proximal Fibronectin Type III Domains

Published as Yang F, West AP Jr, Allendorph GP, Choe S, Bjorkman PJ. (2008) Neogenin Interacts with Hemojuvelin through Its Two Membrane-Proximal Fibronectin Type III Domains. *Biochemistry* **47**(14):4237-45.

Biochemistry **2008,** *47,* 4237–4245

Neogenin Interacts with Hemojuvelin through Its Two Membrane-Proximal Fibronectin Type III Domains[†]

Fan Yang,[‡] Anthony P. West, Jr.,[§] George P. Allendorph,[||] Senyon Choe,[||] and Pamela J. Bjorkman*[,§,⊥]

Graduate Option in Chemistry, Division of Biology, and Howard Hughes Medical Institute, California Institute of Technology, Pasadena, California 91125, and Structural Biology Laboratory, The Salk Institute, La Jolla, California 92037

Received January 8, 2008; Revised Manuscript Received February 19, 2008

ABSTRACT: Hemojuvelin is a recently identified iron-regulatory protein that plays an important role in affecting the expression of hepcidin, a key iron regulatory hormone. Although the underlying mechanism of this process is not clear, several hemojuvelin-binding proteins, including the cell surface receptor neogenin and bone morphogenetic protein (BMP) cytokines, have been identified. The ectodomain of neogenin is composed of four immunoglobulin-like (Ig) domains followed by six fibronectin type III-like (FNIII) domains. Here we report expression of soluble versions of hemojuvelin and neogenin for biochemical characterization of their interaction and the interaction of HJV with BMP-2. Hemojuvelin normally undergoes an autocatalytic cleavage, and as *in vivo*, recombinant hemojuvelin exists as a mixture of cleaved and uncleaved forms. Neogenin binds to cleaved and noncleaved hemojuvelin, as verified by its binding to an uncleaved mutant hemojuvelin. We localized the hemojuvelin binding site on neogenin to the membrane-proximal fifth and sixth FNIII domains and the juxtamembrane linker and showed that a fragment containing only this region binds 2–3 orders of magnitude more tightly than the entire neogenin ectodomain. Binding to the most membrane-proximal region of neogenin may play a role in regulating the levels of soluble and membrane-bound forms of hemojuvelin, which in turn would influence the amount of free BMP-2 available for binding to its receptors and triggering transcription of the hepcidin gene. Our finding that BMP-2 and neogenin bind simultaneously to hemojuvelin raises the possibility that neogenin is part of a multiprotein complex at the hepatocyte membrane involving BMP, its receptors, and hemojuvelin.

Iron is a vital nutrient for almost all organisms. The ability to convert between ferric (Fe^{3+}) and ferrous (Fe^{2+}) states allows iron to function as an electron donor and acceptor in many essential biochemical processes (*1*). However, this feature also makes iron reactive to lipids, proteins, and DNA, resulting in damage to cells. Due to its toxicity and indispensability, iron levels in mammals are under tight control. The transferrin/transferrin receptor system is responsible for the regulated delivery of iron to most vertebrate cells (*2*). In the past decade, other crucial iron-regulatory genes including *HFE* (encoding HFE) (*3*), *TfR2* (encoding transferrin receptor 2) (*4*), *SLC40A1* (encoding ferroportin) (*5–8*), *HAMP* (encoding hepcidin) (*9–11*), and *HFE2* (encoding hemojuvelin or HJV)[1] (*12*) have been discovered, and studies of their physiological roles have revealed additional aspects of mammalian iron homeostasis. Mutations in these genes cause hereditary hemochromatosis (HH), characterized by excess absorption and storage of iron in tissues and organs, eventually leading to irreversible organ damage (*13*).

The gene encoding HJV was identified using a positional cloning strategy in patients with juvenile hemochromatosis (JH) (*12*). Expressed in fetal and adult liver, heart, and skeletal muscle, human HJV is a protein of 426 amino acids, including a hydrophobic N-terminal signal peptide, a conserved RGD triamino acid motif, a partial von Willebrandt factor domain, and a glycosylphosphatidylinisotol (GPI) anchor (*12*). HJV shares sequence similarities with repulsive guidance molecules (RGMs), which are expressed in the central nervous system and function as guidance cues for axons (*14, 15*). HJV and RGMs can undergo autocleavage at a conserved Asp−Pro bond (residues 172–173 in human HJV), resulting in two fragments held together by disulfide bond(s) (*16, 17*). Whether this cleavage is required for HJV function(s) is unknown. The lack of an intracellular domain suggests that HJV acts indirectly to influence cellular activities, perhaps through binding to other receptors at the cell surface. Membrane-bound HJV can be released by a furin-like proprotein convertase (*18*); thus HJV exists in both membrane-bound and soluble forms, giving it the potential to interact with receptors locally and on distant cells.

Disease-causing mutations have been found throughout the HJV sequence (*19*). Patients with HJV mutations were found

[†] This work was supported by the National Institutes of Health (1 R01 DK60770 to P.J.B.).

* To whom correspondence should be addressed at the Division of Biology, 114-96, California Institute of Technology. Tel: 626-395-8350. Fax: 626-792-3693. E-mail: bjorkman@caltech.edu.

[‡] Graduate Option in Chemistry, California Institute of Technology.

[§] Division of Biology, California Institute of Technology.

[||] Structural Biology Laboratory, The Salk Institute.

[⊥] Howard Hughes Medical Institute, California Institute of Technology.

[1] Abbreviations: AU, absorbance unit; BMP, bone morphogenetic protein; CNBr, cyanogen bromide; FNIII, fibronectin type III; HEPES, 4-(2-hydroxyethyl)piperazine-1-ethanesulfonic acid; HJV, hemojuvelin; Ig, immunoglobulin; JH, juvenile hemochromatosis; MW, molecular weight; NTA, nitrilotriacetic acid; RGM, repulsive guidance molecule; RU, resonance unit; SPR, surface plasmon resonance; Tris, tris(hydroxymethyl)aminomethane; UV, ultraviolet; wt, wild type.

10.1021/bi800036h CCC: $40.75
Published on Web 03/13/2008

to have low concentrations of urinary hepcidin (*12*), a key iron-regulatory peptide of 20–25 amino acids that is mainly secreted by the liver (*10*), suggesting that HJV influences hepcidin levels. Consistent with this suggestion, hepcidin mRNA is almost undetectable in $HJV^{-/-}$ mouse hepatocytes (*20*). Although HJV transcripts were found in high levels in skeletal muscle from healthy individuals (*12*), no significant developmental abnormalities were observed in $HJV^{-/-}$ mice other than iron overload (*20*). HJV expression in skeletal muscle is proposed to function to provide a pool of soluble HJV, which competes with the cell-associated form in regulatory pathways (*16*).

Recent studies revealed that neogenin, an immunoglobulin (Ig) superfamily member that is widely expressed in various tissues including brain, kidney, liver, and skeletal muscle (*21, 22*), is a high-affinity receptor for RGMs and that this ligand–receptor complex regulates neuronal survival (*14, 23*). Like its RGM relatives, wild-type HJV (wt HJV) also binds to neogenin, but the most prevalent JH mutant (G320V) does not (*17*). The extracellular portion of human neogenin is composed of four Ig-like domains and six fibronectin type III (FNIII) repeats, and the intracellular domain contains 13 potential serine/threonine phosphorylation sites (*21*). A recent study demonstrated that HJV's involvement in regulatory processes is complex, as HJV was also identified to be a coreceptor for bone morphogenetic proteins 2 and 4 (BMP-2 and BMP-4), cytokines that function in various aspects of cell growth, proliferation, and apoptosis (*24, 25*). The BMP−HJV interaction was found to trigger hepatic hepcidin expression through the classic BMP signaling pathway (*26*). It has been proposed that neogenin regulates the ratio of membrane-bound versus soluble HJV, with the soluble form of HJV competing with the membrane-bound form for binding to BMPs (*27*). How the neogenin−HJV interaction responds to body iron levels and what signaling cascade it receives and/or activates remain to be determined.

In this study, we characterized the interaction between soluble forms of HJV and neogenin by determining the stoichiometry of the complex, its affinity, and the binding epitope on neogenin for HJV. We demonstrated that the HJV-binding epitope of neogenin consists of the two FNIII domains that are closest to the cell membrane and the juxtamembrane linker. Unexpectedly, a truncated form of neogenin containing only this region bound to HJV with an affinity that was 2–3 orders of magnitude higher than the affinity of the intact neogenin ectodomain for HJV. The differences in equilibrium and kinetic constants for the interaction of HJV with the two forms of neogenin suggested that intact neogenin could exist in two conformations: an HJV-binding conformation mimicked by the truncated FNIII construct and a conformation in which the HJV binding site is occluded. In addition, we demonstrated that BMP-2 and neogenin did not compete for binding to HJV, which is consistent with the observation that neither BMP-2 nor its antagonist affects neogenin-mediated HJV shedding from the cell membrane (*28*). These results were interpreted in terms of a model in which neogenin binding affects the levels of soluble versus membrane-bound HJV as part of regulating iron homeostasis.

EXPERIMENTAL PROCEDURES

Construction of Expression Plasmids. Human HJV and neogenin cDNAs were obtained from Caroline Enns at the Oregon Health and Sciences University. The cDNA encoding the ectodomain of HJV (residues 1–401) with a C-terminal 6×-His tag was subcloned into the pVL1393 baculovirus transfer vector (BD Biosciences). A noncleavable HJV mutant D172A, in which residue 172 was changed from aspartate to alanine, was generated using the QuikChange site-directed mutagenesis kit (Qiagen). To make the neogenin ectodomain, DNA encoding the hydrophobic signal sequence (residues 1 – 33), the ectodomain (residues 34−1103), and a C-terminal 6×-His tag was PCR-amplified and ligated into pVL1393. Truncated forms of neogenin consisting of the six FNIII repeats (FNIII 1–6, residues 439–1103) and the last two FNIII repeats (FNIII 5–6, residues 851–1103) were generated by applying the Seamless cloning strategy (Stratagene) to the neogenin ectodomain construct such that both preserved the original hydrophobic signal peptide. As in the neogenin ectodomain construct, the ectodomain tail (residues 1062–1103) was also included in these two truncated neogenin constructs. Individual FNIII domains from neogenin were constructed by subcloning the DNA encoding residues 852–961 (FNIII 5) or residues 952–1103 (FNIII 6), each with a C-terminal 6×-His tag, into the pAcGP67A baculovirus transfer vector (BD Biosciences), which includes a gp67 hydrophobic signal peptide. Shorter versions of FNIII 5–6, FNIII 5, and FNIII 6 were constructed using different beginning and ending residues, which were determined using NMR structures of single neogenin FNIII domains (PDB IDs 1x5j and 1x5k). The shorter versions, sFNIII 5–6, sFNIII 5, and sFNIII 6, consisted of residues 853–1054, 853–952, and 952–1054, respectively. All DNA constructs were verified by sequencing.

Expression and Purification of Recombinant Proteins. Recombinant proteins were purified from the supernatants of baculovirus-infected High Five (Hi-5) cells using Ni-NTA and gel filtration chromatography. Neogenin supernatants were exchanged into 50 mM Tris, pH 7.4, and 150 mM NaCl, and then adjusted to 300 mM NaCl, 10% glycerol, and 10 mM imidazole before being loaded on a Ni-NTA Superflow column (Qiagen). The eluates were then concentrated and loaded onto a Superdex 200 10/30 or Superdex 75 10/30 gel filtration column (GE Healthcare) using a 20 mM Tris, pH 7.4, 150 mM NaCl, and 2 mM EDTA running buffer. The purification of wild-type and mutant HJV was done similarly, except that the buffers contained a higher concentration of NaCl (300 mM for the first buffer exchange, 500 mM for loading of the Ni-NTA column, and 300 mM for the gel filtration column). Human BMP-2 was expressed in *Escherichia coli* as inclusion bodies, purified, and refolded as described (*29*).

Proteolysis of Neogenin. Neogenin FNIII 1–6 was incubated with trypsin (Sigma), papain (Sigma), endoproteinase Glu-C (Sigma), thermolysin (Sigma), or thrombin (Roche) at various enzyme-to-substrate ratios in buffers selected according to the manufacturers' instructions (100 mM Tris−acetate, pH 7.6, 100 mM Bis-Tris, pH 6.5, 100 mM Tris, pH 8.0, 50 mM Tris, pH 8.0, and 50 mM Tris, pH 7.4, respectively). All reactions were stopped by incubation at 100 °C for 5 min. Digested products were analyzed on 11%

SDS−PAGE gels and visualized by staining with Coomassie blue (Bio-Rad). For Western blot analyses, the gels were electroblotted onto Hybond-ECL nitrocellulose membranes (GE Healthcare). The membranes were then incubated with the anti-pentaHis mouse monoclonal antibody (Qiagen) at a 1:2000 dilution and visualized using goat anti-mouse IgG/IgM peroxidase-linked secondary antibody (Jackson ImmunoResearch) at a 1:5000 dilution. After extensive washing, bound antibodies were detected by adding a substrate solution including 3,3′-diaminobenzidine tetrahydrochloride (Sigma) and hydrogen peroxide. Endoproteinase Glu-C digested products were blotted to polyvinylidene difluoride (PVDF) membranes (Millipore), and N-terminal sequencing data were obtained on a Procise protein microsequencer (Applied Biosystems) at the Caltech Protein/Peptide Microanalysis Laboratory (PPMAL). To determine which fragments retained binding to HJV, an HJV affinity column was constructed by coupling several milligrams of HJV to CNBr-activated Sepharose 4B (GE Healthcare) following the manufacturer's instructions.

SPR-Based Affinity Measurements. A BIACORE 2000 or T100 biosensor system (Biacore AB) was used to assay the interactions between HJV, neogenin, and BMP-2 proteins at 25 °C in 20 mM HEPES, pH 7.4, 150 mM NaCl, 2 mM EDTA, and 0.005% surfactant P20 (v/v). Potential aggregates were removed by running protein samples over size exclusion columns immediately before the experiments. Protein concentrations were determined using molar extinction coefficients calculated on the basis of their amino acid sequences using the Expasy ProtParam tool (*30*). HJV was immobilized on a CM5 chip (research grade; Biacore AB) using standard primary amine coupling chemistry (BIACORE manual) at densities of several hundred resonance units (RUs). In some experiments, the noncleavable HJV mutant D172A was coupled on an adjacent flow cell. For kinetics-based experiments, complications due to mass transport (*31*) were avoided by injecting dilutions of various versions of neogenin over the flow cells at flow rates of 50 or 70 μL/min, which were chosen on the basis of the results of flow rate tests to assess mass transport. HJV-coupled chips were regenerated by three pulses of 100 μL of 2 M $MgCl_2$ when needed. Due to a loss of activity of immobilized HJV, different pairs of interactions were conducted on different sensor chips. Raw sensorgrams were preprocessed using the Scrubber software package (http://www.cores.utah.edu/interaction/scrubber.html). The on- and off-rates, k_a and k_d, were obtained by simultaneous fitting of the association and dissociation phases of all curves in the working set to a 1:1 binding model using the program Clamp99 (*32*). K_D values were calculated as k_d/k_a.

The affinity of BMP-2 for HJV was derived using an equilibrium-based binding assay in which binding reactions were allowed to reach equilibrium by using slow flow rates (1−5 μL/min). HJV was injected at various concentrations over immobilized BMP-2 (coupling density ~790 RUs), which was coupled as described for HJV. In some experiments HJV was injected in the presence of 4 μM FNIII 5–6. The binding response at equilibrium (R_{eq}) was plotted as a function of HJV concentration, and best-fit binding curves and K_D values were derived by nonlinear regression analysis using MATLAB (v7.4, The MathWorks). In the competition experiments in which HJV was injected together with 4 μM FNIII 5–6, residual association between FNIII 5–6 and the BMP-2 chip was accounted for by subtracting the signal obtained by injecting 4 μM FNIII 5–6 in the absence of HJV over the BMP-2 chip (172 RUs, whereas 109 RUs was observed in the blank flow cell). The competition assay was repeated using a lower concentration of FNIII 5–6, at which no residual association was observed between FNIII 5–6 and the BMP-2 chip. In this experiment, 500 nM HJV, 400 nM FNIII 5–6, or 500 nM HJV plus 400 nM FNIII 5–6 was injected over the BMP-2 chip.

Determination of Oligomeric States of Proteins and Protein–Protein Complexes. The oligomeric states of HJV and neogenin sFNIII 5–6 were determined by size exclusion chromatography with in-line static light scattering and refractive index monitoring using the ÄKTA chromatography system (GE Healthcare) equipped with a DAWN HELEOS multiangle light scattering detector and Optilab rEX refractometer (Wyatt Technology Corp.). Purified HJV, neogenin sFNIII 5–6, or a 1:1 mixture of HJV plus neogenin sFNIII 5–6 was run over a Superdex 75 10/30 column (GE Healthcare) in 10 mM Tris, pH 8.0, 300 mM NaCl, and 5 mM EDTA. Bovine serum albumin (BSA; gel filtration calibration kit from GE Healthcare) was used as a calibration standard. Data were interpreted using the ASTRA V software (Wyatt Technology Corp.).

Oligomeric states were verified by sedimentation velocity analytical ultracentrifugation using an Optima XL-I analytical ultracentrifuge with an An60 Ti four-hole rotor (Beckman Coulter). Blank buffer (440 μL) and the filtered protein sample (420 μL) were filled into a standard double-sector centerpiece with sapphire windows and spun at 50000 rpm. Absorbance data were collected at 280 nm in the continuous mode with radial increments of 0.03 cm. Buffer properties and the partial specific volume for each protein were calculated by SEDNTERP (*33*). The meniscus and bottom of each set of data were assigned independently using the program SEDFIT (*34*), which also fits the data to a c(s) distribution with the sedimentation coefficient as the x-axis or a c(M) distribution plotted against molecular weight (MW).

RESULTS

Production and Purification of HJV and Neogenin Proteins. The ectodomain of HJV was expressed as a soluble protein in baculovirus-infected insect cells. Purified wt HJV migrated as three bands with apparent molecular masses of 40, 26, and 14 kDa on reducing SDS−PAGE (Figure 1A, lane 2), similar to the partial cleavage pattern observed for HJV existing in natural sources (*16*). The 40 kDa band corresponds to the intact protein while the two lower molecular mass bands represent fragments resulting from an autocleavage at the D172–P173 bond (*16, 17*). These fragments are normally linked by disulfide bond(s) (*16*), as verified by SDS−PAGE analysis under nonreducing conditions (Figure 1B). To produce a homogeneous form of HJV that does not undergo autocleavage, we generated a mutant in which Asp172 at the cleavage site was mutated to alanine (HJV D172A). The purified HJV D172A mutant migrated as a single band with an apparent molecular mass of 40 kDa on reducing SDS−PAGE (Figure 1A, lane 3).

Several forms of neogenin were expressed as described in Experimental Procedures: the full-length ectodomain, the

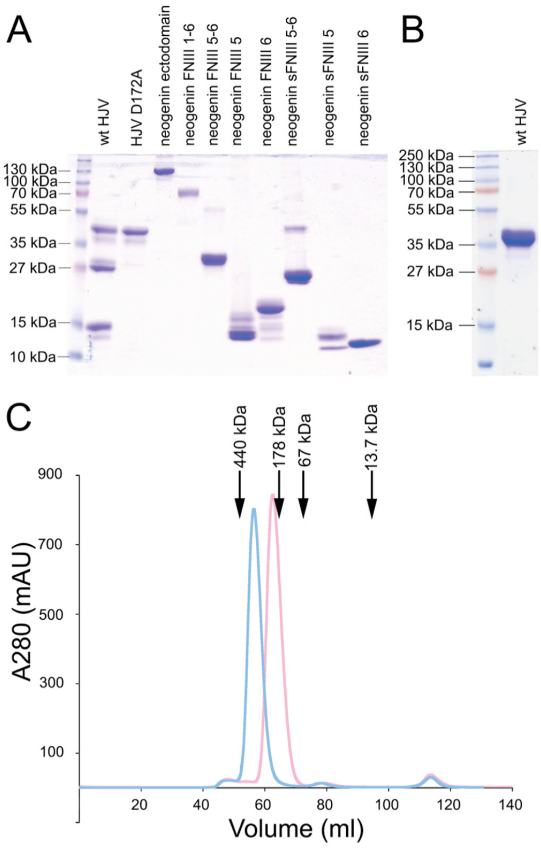

FIGURE 1: Characterizations of HJV and neogenin proteins. (A) Purified HJV and neogenin proteins were separated by 13% reduced SDS−PAGE and stained with Coomassie blue. Molecular masses of standard proteins are indicated on the left. (B) Purified wt HJV analyzed by 13% nonreduced SDS−PAGE. (C) Size exclusion chromatography traces of the neogenin ectodomain (cyan) and neogenin FNIII 1–6 (pink) with absorbance at 280 nm (in absorbance unit, AU) plotted against retention volume (in milliliters). From left to right, black arrows point to the retention volumes of molecular mass standards: ferritin (440 kDa, 53.0 mL), aldolase (158 kDa, 65.0 mL), albumin (67 kDa, 72.7 mL), and ribonuclease A (13.7 kDa, 95.1 mL).

FNIII domains only (FNIII 1–6), FNIII domains 5 and 6 (in two forms, FNIII 5–6 and the *s*horter sFNIII 5–6), FNIII domain 5 only (FNIII 5 and sFNIII 5), and FNIII domain 6 only (FNIII 6 and sFNIII 6). With the exception of neogenin FNIII 6 and sFNIII 6, the neogenin sequences all included potential N-linked glycosylation sites, accounting for their migration as multiple closely spaced bands when analyzed by SDS−PAGE (Figure 1A, lanes 4–11).

Neogenin FNIII 1–6 and the Full-Length Neogenin Ectodomain Bind HJV Equally Well. The FNIII repeats of neogenin have been shown to be the binding site for chicken RGM (*14*), a homologue of HJV. In order to determine if the HJV binding site on neogenin also involved the FNIII repeats, we determined binding affinities for the interaction between HJV and intact neogenin versus FNIII 1–6 using a surface plasmon resonance assay. Affinities were determined from the ratios of kinetic constants derived using a 1:1 binding model (Table 1, Figure 2A,B). The affinities for the neogenin/HJV and FNIII 1–6/HJV interactions were both ~500 nM (Table 1); thus the four Ig-like domains of neogenin were unlikely to be involved in the binding interaction. A higher affinity (9 nM) was reported for the binding of chicken RGM to the ectodomain of chicken neogenin (*14*), suggesting that HJV relatives in other vertebrate species bind more tightly to neogenin than observed for the interaction between human HJV and human neogenin.

Both intact neogenin and FNIII 1–6 also bound to immobilized HJV D172A (Table 1). In addition, when saturated with excess neogenin, immobilized wt HJV (a mixture of intact and cleaved protein) showed the same maximum response as a function of coupling density as immobilized noncleavable HJV D172A, suggesting that neogenin binds to both cleaved and uncleaved forms of HJV and rationalizing why only a single affinity was required to describe the wt HJV interaction with intact neogenin and FNIII 1–6.

HJV Binds to a Proteolytic Fragment of Neogenin Including the Two C-Terminal FNIII Domains. Neogenin is a member of a family of monomeric cell surface proteins with flexible and extended ectodomains that contain multiple Ig and FNIII domains arranged in tandem (*35*). Consistent with an extended structure for neogenin and FNIII 1–6, both proteins migrated with larger apparent molecular masses than corresponding globular proteins when analyzed by gel filtration chromatography (Figure 1C). Reasoning that HJV is unlikely to contact all six domains in an extended FNIII 1–6 structure, we subjected purified FNIII 1–6 to treatment with various proteases in order to find smaller stable fragments and test them for binding to HJV. Endoproteinase Glu-C digestion gave rise to two major proteolytic products, while other proteases either generated many fragments (trypsin, papain, and thermolysin) or did not cleave FNIII 1–6 (thrombin), as assayed by SDS−PAGE (Supporting Information Figure S1A). The two endoproteinase Glu-C produced fragments migrated with apparent molecular masses of 45 and 30 kDa in reducing SDS−PAGE. Western blotting using an anti-poly-His antibody showed that the smaller fragment retained the C-terminal 6×-His tag, thus representing a C-terminal fragment of neogenin FNIII 1–6 (Supporting Information Figure S1B). By using HJV-coupled Sepharose beads in a pull-down assay followed by SDS−PAGE, we found that only the smaller fragment showed detectable binding to HJV (Supporting Information Figure S1C). N-Terminal sequencing of the smaller fragment revealed the sequence VDLFVI, which uniquely identified the cleavage site to be after a glutamate residue located at the end of fourth FNIII domain. These results localized the HJV-binding site to FNIII 5, FNIII 6, and/or the residues C-terminal to FNIII 6.

Neogenin FNIII 5–6 Binds Tightly to HJV with Critical Interactions Contributed by FNIII 6. To further characterize the HJV-binding epitope on neogenin, we expressed FNIII 5–6, a recombinant form of the HJV-binding proteolytic fragment produced from FNIII 1–6. The affinity obtained for neogenin FNIII 5–6 binding to immobilized wt HJV was higher than the affinity obtained for intact neogenin, with a K_D in the subnanomolar range (Figure 2C).

To further map the HJV binding site on FNIII 5–6, we tested the binding of single domain constructs, FNIII 5 and

Table 1: SPR Analyses of the Binding of Neogenin Proteins to Immobilized HJV[a]

	K_D (M)	k_a (M^{-1} s^{-1})	k_d (s^{-1})
neogenin ectodomain → wt HJV	(5.1, 5.0) × 10^{-7}	(2.5, 3.3) × 10^4	(1.3, 1.6) × 10^{-2}
neogenin FNIII 1–6 → wt HJV	(5.6, 5.3) × 10^{-7}	(2.3, 2.7) × 10^4	(1.3, 1.4) × 10^{-2}
neogenin FNIII 5–6 → wt HJV	(2.2 ± 1.5) × 10^{-10}	(4.7 ± 2.0) × 10^6	(1.0 ± 0.7) × 10^{-3}
neogenin FNIII 5th → wt HJV	NB		
neogenin FNIII 6th → wt HJV	(1.8, 2.1) × 10^{-8}	(3.1, 2.8) × 10^5	(5.6, 5.9) × 10^{-3}
neogenin sFNIII 5–6 → wt HJV	(3.6 ± 0.6) × 10^{-9}	(2.3 ± 0.6) × 10^6	(8.0 ± 1.1) × 10^{-3}
neogenin sFNIII 5th → wt HJV	NB		
neogenin sFNIII 6th → wt HJV	(1.9 ± 0.08) × 10^{-6}	(1.4 ± 0.19) × 10^5	(2.6 ± 0.35) × 10^{-1}
neogenin ectodomain → HJV D172A	2.1 × 10^{-6}	3.0 × 10^4	6.4 × 10^{-2}
neogenin FNIII 1–6 → HJV D172A	3.0 × 10^{-6}	1.3 × 10^4	3.8 × 10^{-2}

[a] K_Ds are shown as the average and standard deviation derived from three or four independent measurements or as one or two K_D values for interactions that were measured in single or duplicate experiments. NB indicates that no binding was detected at concentrations up to 8 μM.

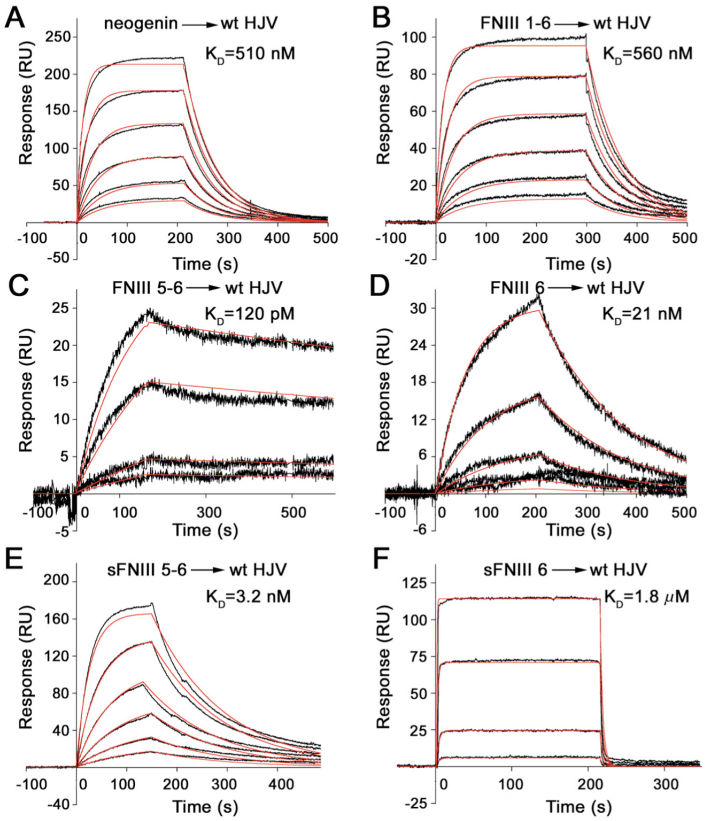

FIGURE 2: Representative SPR data for neogenin proteins binding to immobilized wild-type HJV. In each panel, the protein that was injected over immobilized wt HJV is indicated before the arrow. Proteins were injected as a series of 2-fold dilutions, with the highest injected concentrations being 2 μM, 2 μM, 1.2 nM, 40 nM, 20 nM, and 10 μM for panels A−F, respectively. Sensorgrams (black lines) are overlaid with the simulated response (red lines) derived using a 1:1 binding model. The K_D values shown in each panel are the calculated affinities for the single experiment shown, whereas Table 1 reports average values derived from multiple experiments.

FNIII 6, to HJV. No binding to immobilized HJV was observed at concentrations up to 8 μM for FNIII 5, whereas FNIII 6 bound to HJV with an affinity of ~20 nM (Figure 2D), which is ~100-fold weaker than the affinity of FNIII 5–6, but 25-fold stronger than the affinity of FNIII 1–6. These results suggest that the HJV-binding epitope is primarily located on FNIII 6, with minor contributions from the hinge region between FNIII 5 and FNIII 6 and/or from FNIII 5.

The C-Terminal Linking Region of the Neogenin Ectodomain Contributes to HJV Binding. Unlike other Ig superfamily cell surface receptors such as L1 (*36*), neogenin contains a long linking region (42 residues) between the end of the last FNIII domain and the beginning of the transmembrane region. The sequence is highly conserved among neogenins from different species including human, mouse, rat, and chicken, but no significant similarities were found to any other known proteins by searching in the NCBI database. To determine the effects of this linking region on binding to HJV, we compared the affinities of neogenin FNIII constructs with and without the linking region. The binding of two forms of neogenin FNIII domains lacking the linking region (sFNIII 5–6 and sFNIII 6) to HJV was compared to the binding of

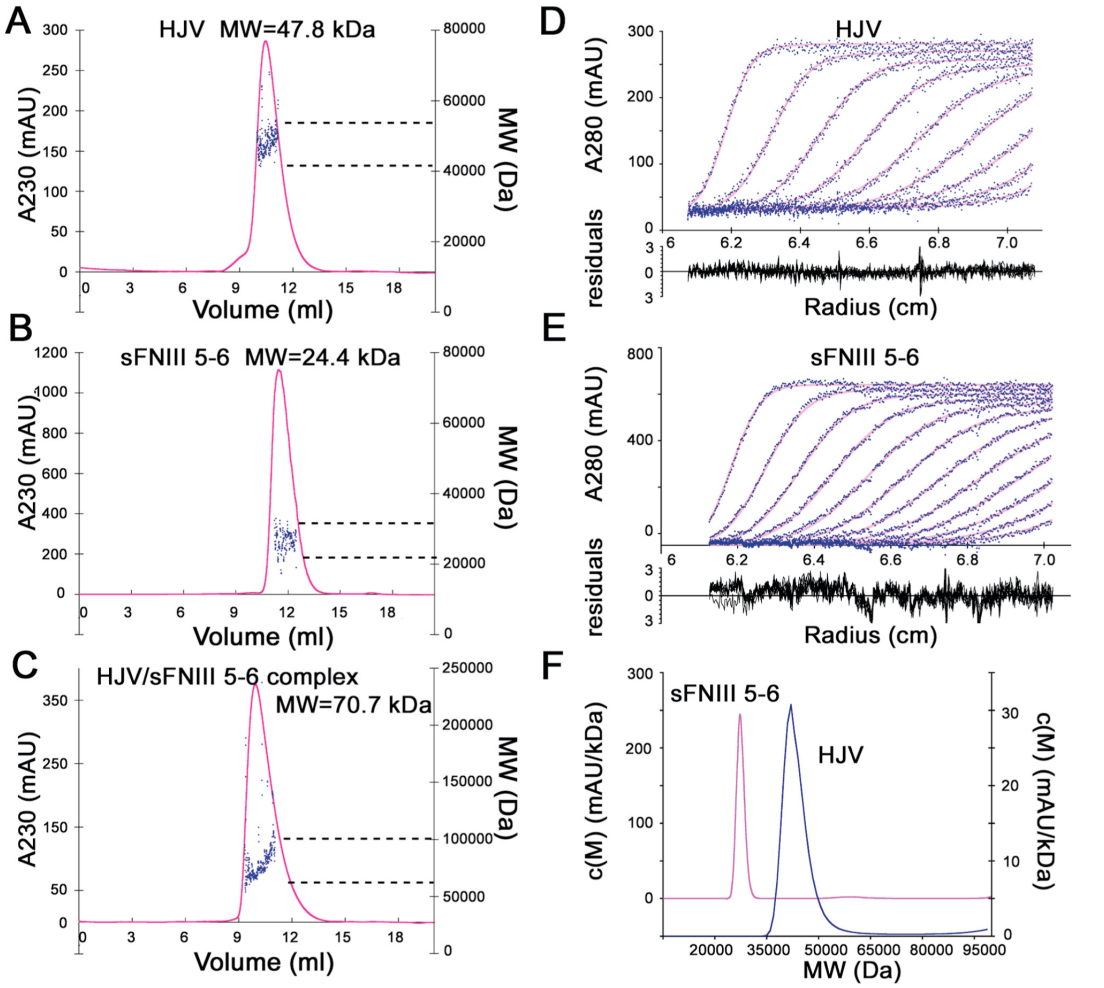

FIGURE 3: Multiangle light scattering and sedimentation velocity analytical ultracentrifugation experiments to determine the oligomeric states of sFNIII 5–6 and HJV. (A−C) Multiangle light scattering data were obtained by injecting protein samples into a size exclusion chromatography system with in-line light scattering and refractive index monitors. Traces of UV absorbance at 230 nm are shown as continuous pink lines. Calculated molecular masses based on multiangle light scattering data are indicated as blue dots with units shown on the right axis. (A) wt HJV. (B) Neogenin sFNIII 5–6. (C) HJV/sFNIII 5–6 complex. (D−F) Sedimentation velocity analytical ultracentrifugation data. (D, E) Sedimentation velocity scans of the absorbance distributions (blue dots) collected for wt HJV (panel D) and neogenin sFNIII 5–6 (panel E) and their best-fit modeled curves (pink continuous line) generated by SEDFIT. Residuals are shown below the curves in black. For clarity, only one out of every ten scans was included in the plots although all scans were used in modeling. (F) Derived molecular mass distributions for wt HJV (blue line, with units shown on right axis) and neogenin sFNIII 5–6 (pink line, with units shown on left axis). c(M) is the unnormalized probability density function of molecular mass, and the integration of c(M) over molecular mass equals to the absorbance of the protein sample.

two forms containing the linking region (FNIII 5–6 and FNIII 6). In both cases, the forms containing the C-terminal tail bound 10–100-fold more tightly to HJV than the shorter forms lacking the tail (Figure 2 and Table 1).

HJV and Neogenin Are Monomers That Form a 1:1 Complex. We used in-line static multiangle light scattering and analytical ultracentrifugation to determine the oligomeric states of sFNIII 5–6, HJV, and their complex (Figure 3). As shown in Figure 3A,B, sFNIII 5–6 and HJV were monomers based on a comparison of their molecular masses calculated from their amino acid sequences (23.9 and 39.8 kDa, not including N-linked glycans) with experimentally determined molecular masses derived from multiangle light scattering data (24.4 and 47.8 kDa). A comparable light scattering experiment demonstrated that the neogenin FNIII 1–6 domain construct was also monomeric (Supporting Information Figure 2). The molecular masses of the sFNIII 5–6 and HJV proteins were also derived by sedimentation velocity analytical ultracentrifugation (Figure 3D,E), yielding single peaks centered at 27 kDa (sFNIII 5–6) and 42 kDa (HJV) in a mass distribution plot (Figure 3F), consistent with the results obtained by multiangle light scattering.

To determine the stoichiometry of the HJV/sFNIII 5–6 complex, we repeated the in-line multiangle light scattering experiment by running a 1:1 mixture of HJV and sFNIII 5–6 over the size exclusion column. Only one peak was found

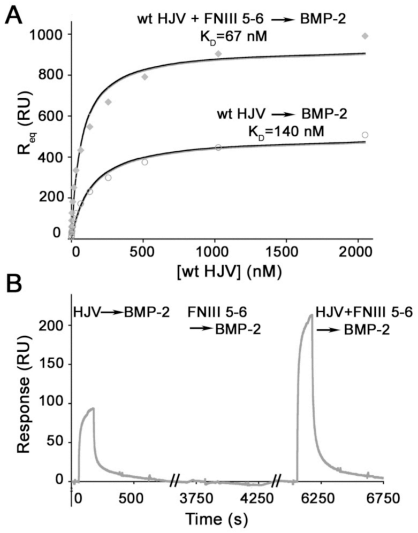

FIGURE 4: Neogenin FNIII 5–6 and BMP-2 do not compete for HJV binding. (A) Plots of equilibrium binding response (R_{eq}) versus the concentration of injected HJV. BMP-2 was immobilized on a sensor chip, and different concentrations of wt HJV were injected in the absence (hollow circles) or presence (solid diamonds) of a saturating concentration (4 μM) of FNIII 5–6. Best-fit binding curves (continuous lines) and K_D values were derived by nonlinear regression analysis. K_D values obtained from an independently conducted experiment using a different BMP-2-coupled flow cell were 130 nM in the absence of FNIII 5–6 and 59 nM in the presence of FNIII 5–6. (B) Sensorgrams from injections of HJV, FNIII 5–6, or their complex over immobilized BMP-2. Left: Injection of 500 nM HJV. Middle: Injection of 400 nM neogenin FNIII 5–6. Right: Injection of a mixture of 500 nM HJV and 400 nM neogenin FNIII 5–6.

in the column profile for the mixture (Figure 3C). The average molecular mass determined for this peak was 70.7 kDa, indicating that the complex was formed at a molar ratio of one HJV to one sFNIII 5–6. These results rule out avidity effects resulting from multimerization of sFNIII 5–6 as an explanation for its tight binding to HJV (Figure 2) and justify the use of 1:1 binding models for fitting the biosensor binding data.

BMP-2 and Neogenin Bind to Nonoverlapping Sites on HJV. To determine the effects of BMP-2 on the binding of HJV to neogenin, we first determined the affinity of HJV for BMP-2. Using an equilibrium-based biosensor binding assay in which HJV was injected over immobilized BMP-2, the affinity was derived as ~140 nM (Figure 4A), ~30–50-fold weaker than the affinities reported in previous studies involving interactions between various RGM-Fc fusion proteins and immobilized BMP-2 (*27, 37*). The higher affinities reported previously are likely to be due to avidity effects resulting from cross-linking of the bivalent RGM-Fc fusion protein to the immobilized BMP-2 dimer. Given that HJV is not normally dimeric (Figure 3B), the lower affinity derived in the present studies is relevant to the physiological situation in which monomeric HJV interacts with BMP-2.

We next repeated the HJV/BMP-2 binding assay in the presence of a saturating concentration (4 μM) of FNIII 5–6. After subtracting the residual response due to injecting a high concentration of FNIII 5–6 over the BMP-2 surface, we observed a higher maximal binding response for HJV in the presence of FNIII 5–6 than in its absence but no significant change in the derived affinity (K_D = 67 nM) (Figure 4A). This result suggested that an FNIII 5–6/HJV complex was binding to immobilized BMP-2, implying that FNIII 5–6 and BMP-2 bind to nonoverlapping sites on HJV.

To verify that neogenin and BMP-2 can bind simultaneously to HJV, we repeated the competition binding experiment using a lower concentration of FNIII 5–6, so that there was no detectable interaction between FNIII 5–6 and the BMP-2 surface. In this experiment, 500 nM HJV was injected in the presence and absence of 400 nM neogenin FNIII 5–6 over immobilized BMP-2. As expected, HJV bound to the BMP-2 surface, but no binding was observed when FNIII 5–6 was injected over immobilized BMP-2 (Figure 4B). Next, a mixture of HJV and neogenin FNIII 5–6 was injected over the same BMP-2 surface. A higher maximum response was observed for the binding of the FNIII 5–6/HJV mixture to immobilized BMP-2 (Figure 4B, the third injection) than for the binding of HJV alone (Figure 4B, the first injection). Since neogenin FNIII 5–6 did not bind BMP-2 directly, the signal increase resulted from an FNIII 5–6/HJV complex binding to immobilized BMP-2 via the HJV protein, demonstrating that BMP-2 and neogenin can bind simultaneously to nonoverlapping sites on HJV to form a ternary complex.

DISCUSSION

HJV is an iron-regulatory protein primarily expressed in skeletal muscle and liver that functions as an upstream modulator of the expression of hepcidin, a liver-synthesized peptide responsible for regulating iron levels in mammals (*12*). How the body iron status affects HJV and how HJV in turn regulates hepcidin expression are unclear. Recent work suggests a two-step process by which serum iron status, as determined by the concentration of iron-loaded transferrin, modulates hepcidin expression as follows: (1) low iron-loaded transferrin levels cause increased neogenin-mediated HJV shedding (*28*), resulting in increased serum HJV and reduced membrane-bound HJV on hepatocytes, and (2) soluble HJV binds to BMP-2 in the blood, preventing its binding to cell surface receptors, thereby reducing BMP signaling and hepcidin expression in hepatocytes (*26*).

Here we used a biochemical approach to characterize the interactions between HJV, neogenin, and BMP-2. We focused initially on the neogenin-HJV interaction, finding that HJV binds to the membrane-proximal region of neogenin, an extended protein with 10 extracellular domains. This finding is of interest given that HJV and its RGM relatives can engage in both *cis* (on the same cell) and *trans* (between cells) interactions with neogenin. For example, neogenin/RGM interactions in axon guidance occur in *trans* (*38*), whereas the HJV/neogenin interaction on muscle cells probably occurs in *cis*. Assuming similar binding of neogenin by HJV and the RGMs, which are closely related by sequence to HJV (*12*), HJV and/or RGMs would be required to access the membrane-proximal region of neogenin whether the proteins are bound to the same or different cells, implying flexibility in one or both of the binding partners. During a *cis* interaction between HJV and neogenin on muscle cells, membrane-bound HJV may be required to bend over to

access its binding epitope on the membrane-proximal FNIII 5–6 domains, thereby possibly exposing it to cleavage. Thus the mapping of the HJV binding epitope on neogenin to its most membrane-proximal domain may help to explain the correlation between neogenin binding and HJV shedding (*28*).

We also discovered that HJV bound to the C-terminal extracellular domains of neogenin 2–3 orders of magnitude more tightly than to the entire neogenin ectodomain. This affinity difference was consistent with differences in the concentrations of each protein required to inhibit HJV shedding from cells expressing intact neogenin and HJV proteins (An-Sheng Zhang and Caroline A. Enns, personal communication). One mechanism to account for the affinity difference is that HJV binds preferentially to an HJV-accessible conformation of neogenin (mimicked by the FNIII 5–6 protein) that is in equilibrium with a nonaccessible conformation, and that addition of HJV shifts the equilibrium to favor the accessible conformation. This model predicts that HJV would bind to the entire neogenin ectodomain with a slower association rate than it binds to FNIII 5–6, while the dissociation rates would be similar. These predictions are consistent with the kinetic data in Table 1, in which it is shown that the association rate for the intact neogenin ectodomain was 2 orders of magnitude lower than that for FNIII 5–6, while the dissociation rates were similar.

Although mutations in HJV in juvenile hemochromatosis patients and deletion of HJV in mice resulted in abnormally low hepcidin expression (*20*), it is unlikely that the interaction between HJV and neogenin is directly involved in regulating hepcidin levels. Instead, recent findings demonstrating that HJV binds some BMPs and that incubation of hepatocytes with exogenous BMP-2 upregulates hepcidin expression (*26*) suggest a more direct role for the HJV−BMP interaction in regulating hepcidin. The BMP signaling pathway is activated by the binding of BMPs to the type II and type I BMP receptor kinases, which in turn induces Smad activation and nuclear translocation, resulting in ligand-specific transcription (*39*). Membrane-bound HJV has been shown to act as a BMP coreceptor (*26*); thus complexes of BMP with its classic receptors and with HJV are likely to exist on the hepatocyte membrane. Here we show that BMP-2 and neogenin could bind simultaneously to HJV, consistent with previous observations that neither BMP-2 nor its antagonist noggin affects neogenin-mediated HJV shedding (*28*). Thus the possibility that neogenin is a component in a cell surface complex that includes BMP receptors, HJV, and BMP must be considered in models for how BMP and HJV affect hepcidin levels to regulate iron homeostasis.

ACKNOWLEDGMENT

We thank Caroline Enns and An-Sheng Zhang (Oregon Health and Sciences University) for cDNAs, sharing unpublished data, and critical reading of the manuscript, Inderjit Nangiana at the Caltech Protein Expression Center for assistance with protein expression, G. Hathaway and the Caltech PPMAL for N-terminal sequencing, Richard Olson for help with analytical ultracentrifugation, and Adrian Rice for assistance with light scattering experiments.

SUPPORTING INFORMATION AVAILABLE

Figure S1 showing the results of proteolytic digests of the neogenin ectodomain and identification of the endoproteinase Glu-C digested products by Western blot and a pull-down assay and Figure S2 showing the data for the determination of the oligomeric state of neogenin FNIII 1–6 using gel filtration chromatography with in-line light scattering. This material is available free of charge via the Internet at http://pubs.acs.org.

REFERENCES

1. Hentze, M. W., Muckenthaler, M. U., and Andrews, N. C. (2004) Balancing acts: molecular control of mammalian iron metabolism. *Cell 117*, 285–297.
2. Dautry-Varsat, A., Ciechanover, A., and Lodish, H. F. (1983) pH and the recycling of transferrin during receptor-mediated endocytosis. *Proc. Natl. Acad. Sci. U.S.A. 80*, 2258–2262.
3. Feder, J. N., Gnirke, A., Thomas, W., Tsuchihashi, Z., Ruddy, D. A., Basava, A., Dormishian, F., Domingo, R., Jr., Ellis, M. C., Fullan, A., Hinton, L. M., Jones, N. L., Kimmel, B. E., Kronmal, G. S., Lauer, P., Lee, V. K., Loeb, D. B., Mapa, F. A., McClelland, E., Meyer, N. C., Mintier, G. A., Moeller, N., Moore, T., Morikang, E., Prass, C. E., Quintana, L., Starnes, S. M., Schatzman, R. C., Brunke, K. J., Drayna, D. T., Risch, N. J., Bacon, B. R., and Wolff, R. K. (1996) A novel MHC class I-like gene is mutated in patients with hereditary haemochromatosis. *Nat. Genet. 13*, 399–408.
4. Camaschella, C., Roetto, A., Cali, A., De Gobbi, M., Garozzo, G., Carella, M., Majorano, N., Totaro, A., and Gasparini, P. (2000) The gene TFR2 is mutated in a new type of haemochromatosis mapping to 7q22. *Nat. Genet. 25*, 14–15.
5. Abboud, S., and Haile, D. J. (2000) A novel mammalian iron-regulated protein involved in intracellular iron metabolism. *J. Biol. Chem. 275*, 19906–19912.
6. Donovan, A., Brownlie, A., Zhou, Y., Shepard, J., Pratt, S. J., Moynihan, J., Paw, B. H., Drejer, A., Barut, B., Zapata, A., Law, T. C., Brugnara, C., Lux, S. E., Pinkus, G. S., Pinkus, J. L., Kingsley, P. D., Palis, J., Fleming, M. D., Andrews, N. C., and Zon, L. I. (2000) Positional cloning of zebrafish ferroportin1 identifies a conserved vertebrate iron exporter. *Nature 403*, 776–781.
7. McKie, A. T., Marciani, P., Rolfs, A., Brennan, K., Wehr, K., Barrow, D., Miret, S., Bomford, A., Peters, T. J., Farzaneh, F., Hediger, M. A., Hentze, M. W., and Simpson, R. J. (2000) A novel duodenal iron-regulated transporter, IREG1, implicated in the basolateral transfer of iron to the circulation. *Mol. Cell 5*, 299–309.
8. Njajou, O. T., Vaessen, N., Joosse, M., Berghuis, B., van Dongen, J. W., Breuning, M. H., Snijders, P. J., Rutten, W. P., Sandkuijl, L. A., Oostra, B. A., van Duijn, C. M., and Heutink, P. (2001) A mutation in SLC11A3 is associated with autosomal dominant hemochromatosis. *Nat. Genet. 28*, 213–214.
9. Krause, A., Neitz, S., Magert, H. J., Schulz, A., Forssmann, W. G., Schulz-Knappe, P., and Adermann, K. (2000) LEAP-1, a novel highly disulfide-bonded human peptide, exhibits antimicrobial activity. *FEBS Lett. 480*, 147–150.
10. Park, C. H., Valore, E. V., Waring, A. J., and Ganz, T. (2001) Hepcidin, a urinary antimicrobial peptide synthesized in the liver. *J. Biol. Chem. 276*, 7806–7810.
11. Roetto, A., Papanikolaou, G., Politou, M., Alberti, F., Girelli, D., Christakis, J., Loukopoulos, D., and Camaschella, C. (2003) Mutant antimicrobial peptide hepcidin is associated with severe juvenile hemochromatosis. *Nat. Genet. 33*, 21–22.
12. Papanikolaou, G., Samuels, M. E., Ludwig, E. H., MacDonald, M. L., Franchini, P. L., Dube, M. P., Andres, L., MacFarlane, J., Sakellaropoulos, N., Politou, M., Nemeth, E., Thompson, J., Risler, J. K., Zaborowska, C., Babakaiff, R., Radomski, C. C., Pape, T. D., Davidas, O., Christakis, J., Brissot, P., Lockitch, G., Ganz, T., Hayden, M. R., and Goldberg, Y. P. (2004) Mutations in HFE2 cause iron overload in chromosome 1q-linked juvenile hemochromatosis. *Nat. Genet. 36*, 77–82.
13. Franchini, M., and Veneri, D. (2005) Recent advances in hereditary hemochromatosis. *Ann. Hematol. 84*, 347–352.
14. Rajagopalan, S., Deitinghoff, L., Davis, D., Conrad, S., Skutella, T., Chedotal, A., Mueller, B. K., and Strittmatter, S. M. (2004)

Neogenin mediates the action of repulsive guidance molecule. *Nat. Cell Biol. 6*, 756–762.
15. Matsunaga, E., and Chedotal, A. (2004) Repulsive guidance molecule/neogenin: a novel ligand-receptor system playing multiple roles in neural development. *Dev. Growth Differ. 46*, 481–486.
16. Lin, L., Goldberg, Y. P., and Ganz, T. (2005) Competitive regulation of hepcidin mRNA by soluble and cell-associated hemojuvelin. *Blood 106*, 2884–2889.
17. Zhang, A. S., West, A. P., Jr., Wyman, A. E., Bjorkman, P. J., and Enns, C. A. (2005) Interaction of hemojuvelin with neogenin results in iron accumulation in human embryonic kidney 293 cells. *J. Biol. Chem. 280*, 33885–33894.
18. Lin, L., Nemeth, E., Goodnough, J. B., Thapa, D. R., Gabayan, V., and Ganz, T. (2008) Soluble hemojuvelin is released by proprotein convertase-mediated cleavage at a conserved polybasic RNRR site. *Blood Cells Mol. Dis. 40*, 122–131.
19. Lanzara, C., Roetto, A., Daraio, F., Rivard, S., Ficarella, R., Simard, H., Cox, T. M., Cazzola, M., Piperno, A., Gimenez-Roqueplo, A. P., Grammatico, P., Volinia, S., Gasparini, P., and Camaschella, C. (2004) Spectrum of hemojuvelin gene mutations in 1q-linked juvenile hemochromatosis. *Blood 103*, 4317–4321.
20. Huang, F. W., Pinkus, J. L., Pinkus, G. S., Fleming, M. D., and Andrews, N. C. (2005) A mouse model of juvenile hemochromatosis. *J. Clin. Invest. 115*, 2187–2191.
21. Vielmetter, J., Chen, X. N., Miskevich, F., Lane, R. P., Yamakawa, K., Korenberg, J. R., and Dreyer, W. J. (1997) Molecular characterization of human neogenin, a DCC-related protein, and the mapping of its gene (NEO1) to chromosomal position 15q22.3-q23. *Genomics 41*, 414–421.
22. Meyerhardt, J. A., Look, A. T., Bigner, S. H., and Fearon, E. R. (1997) Identification and characterization of neogenin, a DCC-related gene. *Oncogene 14*, 1129–1136.
23. Matsunaga, E., Tauszig-Delamasure, S., Monnier, P. P., Mueller, B. K., Strittmatter, S. M., Mehlen, P., and Chedotal, A. (2004) RGM and its receptor neogenin regulate neuronal survival. *Nat. Cell Biol. 6*, 749–755.
24. Chen, D., Zhao, M., and Mundy, G. R. (2004) Bone morphogenetic proteins. *Growth Factors 22*, 233–241.
25. Wagner, T. U. (2007) Bone morphogenetic protein signaling in stem cells—one signal, many consequences. *FEBS J. 274*, 2968–2976.
26. Babitt, J. L., Huang, F. W., Wrighting, D. M., Xia, Y., Sidis, Y., Samad, T. A., Campagna, J. A., Chung, R. T., Schneyer, A. L., Woolf, C. J., Andrews, N. C., and Lin, H. Y. (2006) Bone morphogenetic protein signaling by hemojuvelin regulates hepcidin expression. *Nat. Genet. 38*, 531–539.
27. Xia, Y., Yu, P. B., Sidis, Y., Beppu, H., Bloch, K. D., Schneyer, A. L., and Lin, H. Y. (2007) Repulsive guidance molecule RGMa alters utilization of bone morphogenetic protein (BMP) type II receptors by BMP2 and BMP4. *J. Biol. Chem. 282*, 18129–18140.
28. Zhang, A. S., Anderson, S. A., Meyers, K. R., Hernandez, C., Eisenstein, R. S., and Enns, C. A. (2007) Evidence that inhibition of hemojuvelin shedding in response to iron is mediated through neogenin. *J. Biol. Chem. 282*, 12547–12556.
29. Allendorph, G. P., Vale, W. W., and Choe, S. (2006) Structure of the ternary signaling complex of a TGF-beta superfamily member. *Proc. Natl. Acad. Sci. U.S.A. 103*, 7643–7648.
30. Gill, S. C., and von Hippel, P. H. (1989) Calculation of protein extinction coefficients from amino acid sequence data. *Anal. Biochem. 182*, 319–326.
31. Schuck, P. (1996) Kinetics of ligand binding to receptor immobilized in a polymer matrix, as detected with an evanescent wave biosensor. I. A computer simulation of the influence of mass transport. *Biophys. J. 70*, 1230–1249.
32. Morton, T. A., and Myszka, D. G. (1998) Kinetic analysis of macromolecular interactions using surface plasmon resonance biosensors. *Methods Enzymol. 295*, 268–294.
33. Laue, T. M., S., B. D., Ridgeway, T. M., and Pelletier, S. L. (1992) Computer-aided interpretation of analytical sedimentation data for proteins, in *Analytical Ultracentrifugation in Biochemistry and Polymer Science* (Harding, S. E., Rowe, A. J., and Horton, J. C., Eds.) pp 90−125, Publisher, Address.
34. Schuck, P. (2000) Size-distribution analysis of macromolecules by sedimentation velocity ultracentrifugation and lamm equation modeling. *Biophys. J. 78*, 1606–1619.
35. Kasper, C., Rasmussen, H., Kastrup, J. S., Ikemizu, S., Jones, E. Y., Berezin, V., Bock, E., and Larsen, I. K. (2000) Structural basis of cell-cell adhesion by NCAM. *Nat. Struct. Biol. 7*, 389–393.
36. Bateman, A., Jouet, M., MacFarlane, J., Du, J. S., Kenwrick, S., and Chothia, C. (1996) Outline structure of the human L1 cell adhesion molecule and the sites where mutations cause neurological disorders. *EMBO J. 15*, 6050–6059.
37. Halbrooks, P. J., Ding, R., Wozney, J. M., and Bain, G. (2007) Role of RGM coreceptors in bone morphogenetic protein signaling. *J. Mol. Signaling 2*, 4.
38. Yamashita, T., Mueller, B. K., and Hata, K. (2007) Neogenin and repulsive guidance molecule signaling in the central nervous system. *Curr. Opin. Neurobiol. 17*, 29–34.
39. Derynck, R., and Zhang, Y. E. (2003) Smad-dependent and Smad-independent pathways in TGF-beta family signalling. *Nature 425*, 577–584.

BI800036H

Figure S1

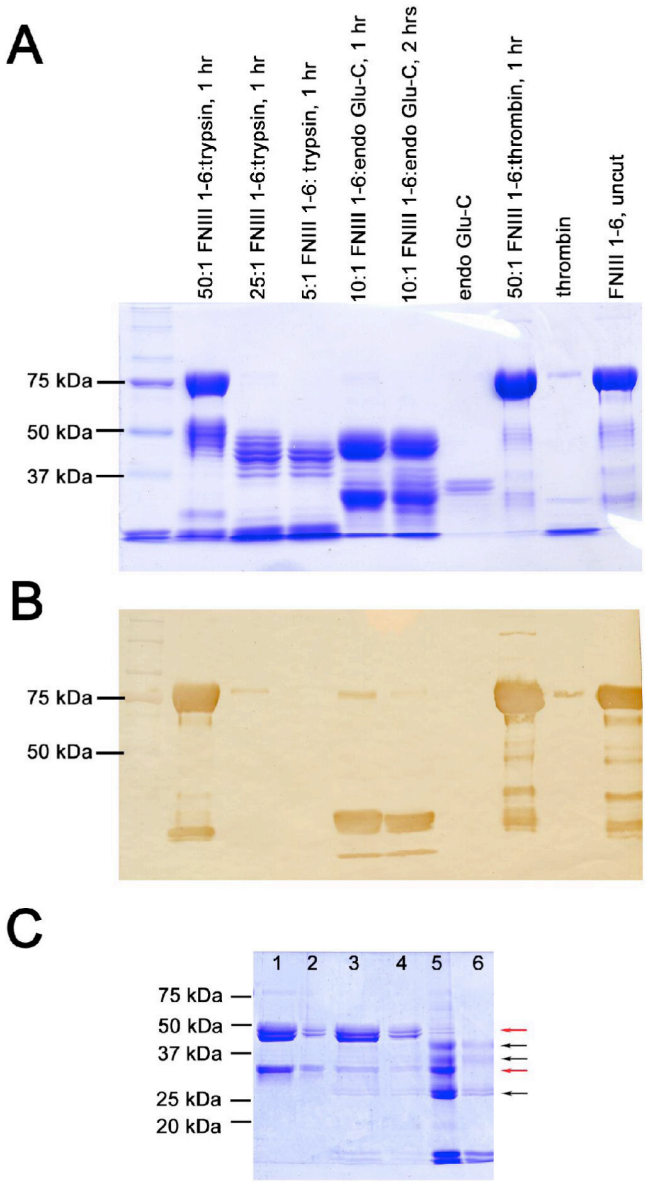

82x144mm (400 x 400 DPI)

Figure S2

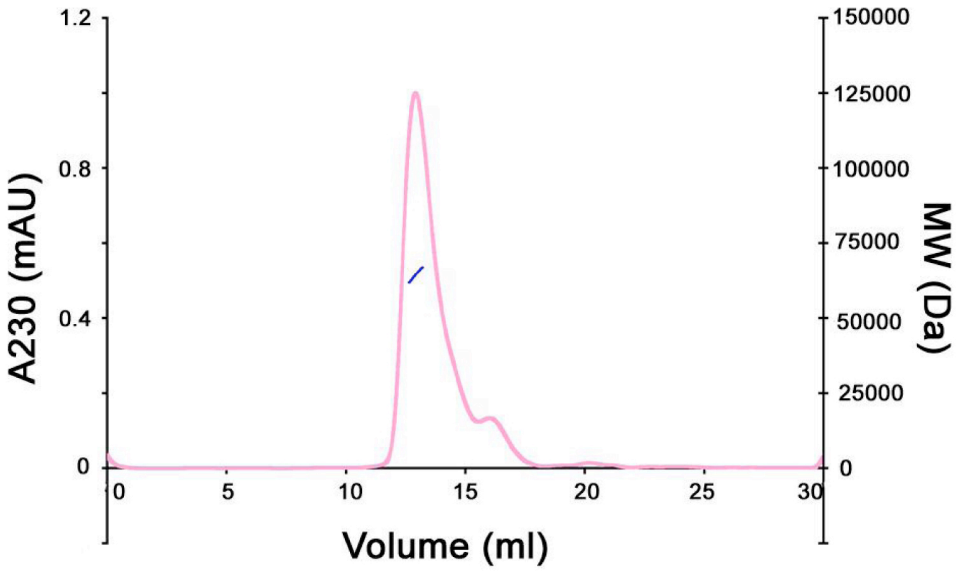

82x50mm (300 x 300 DPI)

Chapter 3:
Crystal structure of a hemojuvelin-binding fragment of neogenin at 1.8 Å

Published as Yang F, West AP Jr, Bjorkman PJ. (2010) Crystal structure of a hemojuvelin-binding fragment of neogenin at 1.8 Å (in press)

Abstract

Neogenin is a type I transmembrane glycoprotein with a large ectodomain containing tandem immunoglobulin-like and fibronectin type III (FNIII) domains. Closely related to the tumor suppressor gene DCC, neogenin functions in critical biological processes through binding to various ligands, including netrin, repulsive guidance molecules, and the iron regulatory protein hemojuvelin. We previously reported that neogenin binds to hemojuvelin through its membrane-proximal fifth and sixth FNIII domains (FN5-6), with domain 6 (FN6) contributing the majority of critical binding interactions. Here we present the crystal structure of FN5-6, the hemojuvelin-binding fragment of human neogenin, at 1.8 Å. The two FNIII domains are orientated nearly linearly, a domain arrangement most similar to that of a tandem FNIII-containing fragment within the cytoplasmic tail of the β4 integrin. By mapping surface-exposed residues that differ between neogenin FN5-6 and the comparable domains from DCC, which does not bind hemojuvelin, we identified a potential hemojuvelin-binding site on neogenin FN6. Neogenin FN5, which does not bind hemojuvelin in isolation, exhibits a highly electropositive surface, which may be involved in interactions with negatively-charged polysaccharides or phospholipids in the membrane bilayer. The neogenin FN5-6 structure can be used to facilitate a molecular understanding of neogenin's interaction with hemojuvelin to regulate iron homeostasis and with hemojuvelin-related repulsive guidance molecules to mediate axon guidance.

1. Introduction

Neogenin is a type I transmembrane glycoprotein expressed in multiple tissues including brain, kidney, liver, and skeletal muscle (Meyerhardt et al., 1997; Vielmetter et al., 1997). Closely-related to the tumor suppressor molecule DCC (Deleted in Colorectal Cancer) (Vielmetter et al., 1994), neogenin is composed of four immunoglobulin (Ig)-like domains followed by six fibronectin type III (FNIII) domains, a transmembrane region, and a cytoplasmic domain (Vielmetter et al., 1994; Vielmetter et al., 1997). Neogenin functions in a variety of developmental and metabolic processes (Wilson and Key, 2007), and several ligands have been identified, including netrin, repulsive guidance molecules (RGMs) (Matsunaga and Chedotal, 2004; Matsunaga et al., 2004; Rajagopalan et al., 2004), and the iron regulatory protein hemojuvelin (Zhang et al., 2005).

While netrin-1 and neogenin mediate chemoattractive axon guidance, the neogenin/RGMa interaction functions specifically in axon repulsion (Wilson and Key, 2006). Neogenin has also been implicated as a dependence receptor (Bredesen et al., 2005), such that it triggers apoptosis in the absence of a ligand RGM molecule, whereas the ligand-bound state inhibits this effect (Matsunaga and Chedotal, 2004; Matsunaga et al., 2004). Downstream signaling elicited by the binding of neogenin to RGMa involves the Rho family of small GTP-binding proteins, which regulate cytoskeletal dynamics by controlling actin filaments and causing growth cone collapse (Conrad et al., 2007). Pre-incubation of netrin-1 inhibits this signaling, indicating either that netrin-1 occludes the RGMa-binding site on neogenin, or that a different signaling cascade is initiated to counteract the Rho-mediated signaling (Conrad et al., 2007).

In hepatocytes and perhaps also skeletal muscle, neogenin is involved in iron homeostasis through interactions with hemojuvelin, also known as HFE2 or RGMc (Zhang et al., 2005). Hemojuvelin is a glycosylphosphatidylinositol (GPI)-anchored protein that shares sequence similarity with RGMa and RGMb, which, unlike hemojuvelin (RGMc), are expressed predominantly in the nervous system (Schmidtmer and Engelkamp, 2004). Hemojuvelin is an upstream modulator of hepcidin, a peptide hormone that regulates iron flux in mammals (Lin et al., 2005). Interaction with neogenin has been suggested to initiate retrograde trafficking of membrane-bound hemojuvelin to the Golgi and trans-Golgi network for further processing before soluble hemojuvelin is released from the cell (Maxson et al., 2009; Zhang et al., 2007; Zhang et al., 2008). The ratio of membrane-bound and soluble forms of hemojuvelin is believed to be important for determining the amount of signal sent to the nucleus through the bone morphogenetic protein (BMP)/hemojuvelin pathway, which regulates hepcidin expression levels (Babitt et al., 2006).

We previously described biochemical studies using neogenin ectodomain deletion mutants to localize the hemojuvelin-binding site to the two membrane-proximal FNIII domains (FN5-6) (Yang et al., 2008). The FN5-6 fragment was as effective as the intact neogenin ectodomain in competing with cell membrane neogenin, both *in vitro* (Zhang et al., 2008) and *in vivo* (Zhang et al., 2009), suggesting that the FN5-6 region contains the hemojuvelin-binding region on neogenin. While FN5 did not bind detectably to hemojuvelin, FN6 alone bound hemojuvelin, although more weakly than FN5-6, suggesting a potential contribution from the domain linking region in the binding interaction (Yang et al., 2008).

Here we report the crystal structure of the hemojuvelin-binding fragment of human neogenin, FN5-6, at 1.8 Å resolution. Each domain adopts the canonical FNIII fold, with the two domains arranged nearly linearly, surprisingly similar to the arrangement of a pair of tandem FNIII domains from the cytoplasmic tail of the β4 integrin. The neogenin FN5 domain displays a highly positively-charged surface, a feature shared with DCC FN5 and other proteins known to bind heparan sulfate (Bennett et al., 1997; McLellan et al., 2006). In addition to the possibility of interacting with negatively-charged carbohydrate or protein ligands, we suggest that the positive surface on the neogenin FN5 domain may promote interactions with negatively-charged phospholipids to facilitate exposure of the hemojuvelin-binding FN6 domain to hemojuvelin proteins on the surface of another cell. To gain insight into which portion of neogenin FN5-6 interacts with hemojuvelin, we mapped non-conserved residues from the comparable domains of DCC, which does not bind hemojuvelin, onto the neogenin FN5-6 structure. One side of the FN6 domain, comprising strands C, C', F, and G, contains a high concentration of non-conserved surface residues, suggesting that this face of the molecule contains the potential hemojuvelin-binding site.

2. Materials and Methods

2.1 Crystallization and data collections

Neogenin FN5-6, corresponding to the fifth and sixth FNIII domains of human neogenin (residues 853-1054) plus a C-terminal 6x-His tag, was expressed in baculovirus-infected insect cells and purified from supernatants as previously described (Yang et al., 2008). This version of neogenin FN5-6 was previously referred to as sFNIII

5-6 to distinguish it from a longer version of these domains (FNIII 5-6; residues 851-1103). The longer version bound to hemojuvelin with ~18 fold higher affinity than FN5-6 (Yang et al., 2008), but did not crystallize, presumably due to disorder of the C-terminal extension. The best crystals were obtained from FN5-6 purified from culture media supplemented with 0.5 mg/L tunicamycin (Sigma) to inhibit addition of N-linked glycans. Crystallization screening was done using a Mosquito nanoliter handling system (TTP LabTech) with drops containing 200 nL protein plus an equal volume of reservoir solution. Initial crystals grew in mother liquor containing 0.1 M Tris, pH 8.5, 0.2 M ammonium sulfate, 25% PEG-3350 at 20˚C. Larger crystals were obtained in a Qiagen 24-well screw-top hanging drop plate using the same mother liquor. A single crystal was cryo-preserved in mother liquor supplemented with 5% glycerol and a native data set was collected on an R-AXIS-VI rotating anode X-ray generator (Rigaku) at 100 K.

2.2 Structure determination and model refinement

Data were processed by Denzo and scaled using Scalepack (Otwinowski and Minor, 1997) in the orthorhombic space group $C222_1$ (a = 52.6 Å, b = 112.9 Å, c = 80.9 Å). The calculated Matthews coefficient (V_M=2.5 $Å^3$/Da) (Matthews, 1968) suggested a solvent content of 51% and one molecule per asymmetric unit. The structure was solved by molecular replacement using the program Phaser (McCoy et al., 2007) and search models derived from NMR structures of individual domains of neogenin (PDB codes 1X5J and 1X5K) in which residues not present in our construct were deleted. Solvent-flattened electron density maps for model building were generated using the program DM (CCP4, 1994). After rigid body refinement, the model was iteratively improved using

cycles of refinement using CNS (Brunger et al., 1998) and manual rebuilding using COOT (Emsley and Cowtan, 2004) into $2F_o$-F_c annealed omit maps. The final model (R_{cryst}= 20.0% and R_{free} = 23.4%) consists of neogenin residues 853-899 and 903-1052 (residues 900-902 were disordered), and 293 water molecules (Table 1). For analyses of contacts and buried surface areas, FN5 was defined as residues 853-949, and FN6 was defined as residues 952-1052. The CCP4 program Areaimol (CCP4, 1994; Lee and Richards, 1971; Saff and Kuijlaars, 1997) was used to calculate buried surface area using a 1.4 Å probe and to identify interacting residues using the following criteria: a distance of <3.5 Å and a hydrogen bond angle of >90° for hydrogen bonds and a maximum distance of 4.0 Å for van der Waals interactions. Figures were prepared by Pymol (DeLano, 2002).

3. Results

3.1 Overview of the neogenin FN5-6 structure

Initial crystallization trials with insect cell-expressed neogenin FN5-6 yielded crystals that diffracted to only 15 Å. The expression of FN5-6 was repeated in the presence of tunicamycin, an inhibitor of N-linked glycosylation. Neogenin FN5-6 derived from tunicamycin-treated cells migrated as a slightly smaller apparent molecular weight than its untreated counterpart, consistent with successful inhibition of glycan attachment to the single predicted N-linked glycosylation site in FN5-6 (data not shown), and crystals obtained from the treated protein diffracted to 1.8 Å. A molecular replacement solution was obtained by searching simultaneously for the two individual FNIII domains.

The structure of neogenin FN5-6 reveals two domains arranged in an extended conformation (Figure 1A). The neogenin FNIII domains share the canonical FNIII folding topology, with each FNIII domain containing two anti-parallel β-sheets, one formed by β-strands A, B, and E and the other by β-strands C', C, F, and G. Preceding strand G in both domains is a polyproline II helix, a common feature of FNIII domains (Huber et al., 1994). Another polyproline II helix (residue 1-5) is present in strand A in the FN5 domain and a short 3_{10} helix is found between strands C and C' in the FN6 domain. The two domains interact via a hydrogen bonding network (Figure 1B) that stabilizes the extended conformation observed for the structure in the crystals. The hydrogen bonding network, taken together with a lack of obvious crystal contacts that would promote the observed interdomain conformation, suggest that the domain arrangement in the crystals would be preserved in solution.

3.2 Comparison with other FNIII domain structures

The DaliLite server (Holm et al., 2008) was used to compare the neogenin FN5-6 structure with other FNIII domains. In isolation, the closest structural homolog of neogenin FN5 is the FN1 domain from the plectin-bound β4 integrin (de Pereda et al., 2009), and neogenin FN6 is most closely related to DCC FN6 (PDB code 2EDE; to be published). We also compared neogenin FN5-6 to available tandem FNIII structures including the β4 integrin cytoplasmic domain (de Pereda et al., 1999), neuroglian FN1-2 (Huber et al., 1994), NCAM FN1-2 (Carafoli et al., 2008), fibronectin FN7-10 (Leahy et al., 1996), NCAM2 FN1-2 (PDB code 2JLL; to be published), and Ihog FN1-2 (McLellan et al., 2006). The neogenin FN5-6 domain arrangement was most similar to

the arrangement of FNIII domains in the intracellular region of the β4 integrin (Supplementary Figure 1A), both in the interdomain tilt angle and the relative rotation angle (Table 2). A total of ~500 $Å^2$ was buried between the two neogenin FNIII domains, an intermediate value for buried surface areas in tandem FNIII domain structures, which ranged from 280 Å for NCAM2 FN1-2 to 1170 Å for Ihog FN1-2.

Electrostatic potential calculations revealed that neogenin FN5 is highly positively charged (Figure 1C), a feature shared with only a few other FNIII domains with structures available in the Protein Data Bank: of 80 available structures of FNIII domains, the only highly positively-charged domains were from the FN5 domain of DCC (PDB code 2EDD; to be published) (Figure 1C), FN1 from Ihog (McLellan et al., 2006), and FNIII domains from four other unpublished structures (PDB codes 1X4Z, 1UEN, 1WFT, and 1UJT). Calculated electrostatic potential surfaces for a subset of these FNIII structures (the available tandem FNIII domain structures) are shown in Supplementary Figure 1B.

3.3 Sequence comparison with DCC molecule and implications for ligand binding

We previously showed that isolated neogenin FN6 (sFNIII 6; residues 952-1054) bound to hemojuvelin with an affinity of ~2 μM, almost 1000-fold more weakly than neogenin FN5-6, whereas isolated neogenin FN5 (sFNIII 5; residues 853-952) showed no detectable binding to hemojuvelin (Yang et al., 2008). These results suggested that the hemojuvelin-binding epitope (and by analogy, the RGM-binding epitope) on neogenin is primarily located in FN6. To gain insight into potential hemojuvelin/RGM-binding interface(s) on neogenin, we mapped residues from DCC onto the neogenin FN5-6

structure. Previous studies demonstrated that hemojuvelin does not bind DCC, although neogenin FN5-6 and DCC FN5-6 share 64% sequence identity and 83% similarity (Figure 2A) and DCC is the closest homolog of neogenin (Zhang et al., 2005). Thus a concentration of non-conserved residues could represent a potential hemojuvelin/RGM binding interface on neogenin. A portion of FN6 comprising the 3_{10} helix in the C-C' loop, the C' strand, and the loop between strands E and F is enriched in non-conserved surface residues, suggesting its potential involvement in binding hemojuvelin (Figure 2B).

The highly positive nature of the neogenin FN5 domain (Figure 1C) suggests a model (Figure 3) in which the FN5 domain interacts with negatively-charged phospholipids on the membrane bilayer to expose the membrane-proximal FN6 domain of neogenin for trans (between cells) interactions with RGMs (Yamashita et al., 2007). Alternatively, the basic patch on FN5 could bind to an as yet unidentified highly negatively-charged protein ligand or to negatively-charged polysaccharide chains, such as heparan sulfate, as has been demonstrated for DCC FN5 (Bennett et al., 1997) and for Ihog (McLellan et al., 2006).

4. Discussion

Tandem FNIII domains are found in many signal-transducing cell surface receptors, including gp130, Ihog, neuroglian, and neogenin. Although a FNIII fold can be identified from sequence information alone, the arrangement of tandem FNIII domains cannot be predicted from a sequence. Structures of tandem FNIII domains have revealed a variety of domain arrangements, ranging from nearly linear (e.g., β4 integrin) to

slightly or completely bent (e.g., NCAM, neuroglian, fibronectin, and Ihog FNIII domains) (Supplementary Figure 1A). The crystal structure of the hemojuvelin-binding neogenin FN5-6 fragment reported here reveals a nearly linear domain arrangement. Surprisingly, this arrangement is most similar to the arrangement of intracellular FNIII domains in the cytoplasmic tail of the β4 integrin. The significance of the structural similarity between tandem FNIII domains in the extracellular region of neogenin and the intracellular region of an integrin is unknown.

The neogenin FN5-6 structure revealed an unusually electropositive surface, which is shared by only a few other FNIII domains, including DCC FN5 and Ihog FN1. Both DCC FN5 and Ihog FN1 bind to heparan sulfate (Bennett et al., 1997; McLellan et al., 2006), suggesting that neogenin FN5 may also interact with heparan or other negatively-charged polysaccharide chains. Alternatively, or perhaps in addition to, binding to heparan sulfate, the positive charges on neogenin FN5 could facilitate ligand (hemojuvelin or RGM) access to the membrane-proximal FN6 domain through interactions between FN5 and negatively-charged lipids on the membrane bilayer (Figure 3). The surface of DCC FN5 is also highly positive (Figure 1C) and the basic residues in the DCC and neogenin FN5 domains are mostly conserved (Figure 2A), suggesting a similar function for DCC FN5. Consistent with this idea, the netrin-binding site on DCC has been mapped to a nearby region; either FN4 or FN5 (Geisbrecht et al., 2003; Kruger et al., 2004).

The discovery of hemojuvelin as a co-receptor for BMP during activation of hepcidin expression (Babitt et al., 2006) suggested the possibility of using BMP antagonists for the treatment of anemia (Browne and Reddan, 2009). Alternatively, since

the neogenin FN5-6 fragment described here has been shown to suppress BMP-mediated hepcidin expression both in vitro and in vivo (Zhang et al., 2009), it may be possible to treat anemia by using this fragment. Identification of a potential hemojuvelin-binding site on neogenin FN6 (Figure 2B) may be informative in designing such a drug if modifications are needed.

Protein Data Bank Accession Code

Coordinates and structure factors for neogenin FN5-6 have been deposited with RCSB Protein Data Bank with code 3P4L.

Acknowledgements

We thank Inder Nangiana and the Caltech Protein Expression Center for assistance with protein expression, Pavle Nickolovski and the Caltech Molecular Observatory for assistance with automated crystallization, Dr. Leonard Thomas for help with X-ray data collection, and members of the Bjorkman lab for critical reading of the manuscript. The authors acknowledge the Gordon and Betty Moore Foundation for support of the Molecular Observatory at Caltech.

Abbreviations used:

DCC, deleted in colorectal cancer; Ig, immunoglobulin; FNIII, fibronectin type III; RGM, repulsive guidance molecule; BMP, bone morphogenetic protein; Ihog, interference hedgehog.

References

Babitt, J.L., F.W. Huang, D.M. Wrighting, Y. Xia, Y. Sidis, T.A. Samad, J.A. Campagna, R.T. Chung, A.L. Schneyer, C.J. Woolf, N.C. Andrews, and H.Y. Lin, 2006. Bone morphogenetic protein signaling by hemojuvelin regulates hepcidin expression. Nat Genet 38: 531-9.

Baker, N.A., D. Sept, S. Joseph, M.J. Holst, and J.A. McCammon, 2001. Electrostatics of nanosystems: application to microtubules and the ribosome. Proc Natl Acad Sci U S A 98: 10037-41.

Bennett, K.L., J. Bradshaw, T. Youngman, J. Rodgers, B. Greenfield, A. Aruffo, and P.S. Linsley, 1997. Deleted in colorectal carcinoma (DCC) binds heparin via its fifth fibronectin type III domain. J Biol Chem 272: 26940-6.

Bredesen, D.E., P. Mehlen, and S. Rabizadeh, 2005. Receptors that mediate cellular dependence. Cell Death and Differentiation 12: 1031-1043.

Browne, S.A., and D. Reddan, 2009. Potential role of bone morphogenetic protein (BMP) signalling as a potential therapeutic target for modification of iron balance. Nephrol Dial Transplant 24: 28-30.

Brunger, A.T., P.D. Adams, G.M. Clore, W.L. DeLano, P. Gros, R.W. Grosse-Kunstleve, J.S. Jiang, J. Kuszewski, M. Nilges, N.S. Pannu, R.J. Read, L.M. Rice, T. Simonson, and G.L. Warren, 1998. Crystallography & NMR system: A new software suite for macromolecular structure determination. Acta Crystallogr D Biol Crystallogr 54: 905-21.

Carafoli, F., J.L. Saffell, and E. Hohenester, 2008. Structure of the tandem fibronectin type 3 domains of neural cell adhesion molecule. J Mol Biol 377: 524-34.

CCP4, 1994. The CCP4 suite: programs for protein crystallography. Acta Crystallogr D Biol Crystallogr 50: 760-3.

Conrad, S., H. Genth, F. Hofmann, I. Just, and T. Skutella, 2007. Neogenin-RGMa signaling at the growth cone is bone morphogenetic protein-independent and involves RhoA, ROCK, and PKC. Journal of Biological Chemistry 282: 16423-16433.

de Pereda, J.M., G. Wiche, and R.C. Liddington, 1999. Crystal structure of a tandem pair of fibronectin type III domains from the cytoplasmic tail of integrin alpha 6 beta 4. Embo Journal 18: 4087-4095.

de Pereda, J.M., M.P. Lillo, and A. Sonnenberg, 2009. Structural basis of the interaction between integrin alpha 6 beta 4 and plectin at the hemidesmosomes, Embo Journal 28: 1180-1190.

DeLano, W.L., 2002. The PyMOL Molecular Graphics System DeLano Scientific, San Carlos, CA.

Emsley, P., and K. Cowtan, 2004. Coot: model-building tools for molecular graphics. Acta Crystallogr D Biol Crystallogr 60: 2126-32.

Geisbrecht, B.V., K.A. Dowd, R.W. Barfield, P.A. Longo, and D.J. Leahy, 2003. Netrin binds discrete subdomains of DCC and UNC5 and mediates interactions between DCC and heparin. J Biol Chem 278: 32561-8.

Holm, L., S. Kaariainen, P. Rosenstrom, and A. Schenkel, 2008. Searching protein structure databases with DaliLite v.3. Bioinformatics 24: 2780-1.

Huber, A.H., Y.M. Wang, A.J. Bieber, and P.J. Bjorkman, 1994. Crystal structure of tandem type III fibronectin domains from Drosophila neuroglian at 2.0 A. Neuron 12: 717-31.

Kruger, R.P., J. Lee, W. Li, and K.L. Guan, 2004. Mapping netrin receptor binding reveals domains of Unc5 regulating its tyrosine phosphorylation. J Neurosci 24: 10826-34.

Leahy, D.J., I. Aukhil, and H.P. Erickson, 1996. 2.0 A crystal structure of a four-domain segment of human fibronectin encompassing the RGD loop and synergy region. Cell 84: 155-64.

Lee, B., and F.M. Richards, 1971. The interpretation of protein structures: estimation of static accessibility. J Mol Biol 55: 379-400.

Lin, L., Y.P. Goldberg, and T. Ganz, 2005. Competitive regulation of hepcidin mRNA by soluble and cell-associated hemojuvelin. Blood 106: 2884-9.

Matsunaga, E., and A. Chedotal, 2004. Repulsive guidance molecule/neogenin: a novel ligand-receptor system playing multiple roles in neural development. Dev Growth Differ 46: 481-6.

Matsunaga, E., S. Tauszig-Delamasure, P.P. Monnier, B.K. Mueller, S.M. Strittmatter, P. Mehlen, and A. Chedotal, 2004. RGM and its receptor neogenin regulate neuronal survival. Nat Cell Biol 6: 749-55.

Matthews, B.W., 1968. Solvent content of protein crystals. J Mol Biol 33: 491-7.

Maxson, J.E., C.A. Enns, and A.S. Zhang, 2009. Processing of hemojuvelin requires retrograde trafficking to the Golgi in HepG2 cells. Blood 113: 1786-93.

McCoy, A.J., R.W. Grosse-Kunstleve, P.D. Adams, M.D. Winn, L.C. Storoni, and R.J. Read, 2007. Phaser crystallographic software. J Appl Crystallogr 40: 658-674.

McLellan, J.S., S. Yao, X. Zheng, B.V. Geisbrecht, R. Ghirlando, P.A. Beachy, and D.J. Leahy, 2006. Structure of a heparin-dependent complex of Hedgehog and Ihog. Proc Natl Acad Sci U S A 103: 17208-13.

Meyerhardt, J.A., A.T. Look, S.H. Bigner, and E.R. Fearon, 1997. Identification and characterization of neogenin, a DCC-related gene. Oncogene 14: 1129-36.

Otwinowski, Z., and W. Minor, 1997. Processing of X-ray Diffraction Data Collected in Oscillation Mode, p. 307-326, Methods in Enzymology, Academic Press.

Rajagopalan, S., L. Deitinghoff, D. Davis, S. Conrad, T. Skutella, A. Chedotal, B.K. Mueller, and S.M. Strittmatter, 2004. Neogenin mediates the action of repulsive guidance molecule. Nat Cell Biol 6: 756-62.

Saff, E.B., and A.B.J. Kuijlaars, 1997. Distributing many points on a sphere. Mathematical Intelligencer 19: 5-11.

Schmidtmer, J., and D. Engelkamp, 2004. Isolation and expression pattern of three mouse homologues of chick Rgm. Gene Expr Patterns 4: 105-10.

Su, X.D., L.N. Gastinel, D.E. Vaughn, I. Faye, P. Poon, and P.J. Bjorkman, 1998. Crystal structure of hemolin: a horseshoe shape with implications for homophilic adhesion. Science 281: 991-5.

Vielmetter, J., J.F. Kayyem, J.M. Roman, and W.J. Dreyer, 1994. Neogenin, an Avian Cell-Surface Protein Expressed during Terminal Neuronal Differentiation, is Closely-Related to the Human Tumor-Suppressor Molecule Deleted in Colorectal-Cancer. Journal of Cell Biology 127: 2009-2020.

Vielmetter, J., X.N. Chen, F. Miskevich, R.P. Lane, K. Yamakawa, J.R. Korenberg, and W.J. Dreyer, 1997. Molecular characterization of human neogenin, a DCC-related protein, and the mapping of its gene (NEO1) to chromosomal position 15q22.3-q23. Genomics 41: 414-21.

Wilson, N.H., and B. Key, 2006. Neogenin interacts with RGMa and netrin-1 to guide axons within the embryonic vertebrate forebrain. Dev Biol 296: 485-98.

Wilson, N.H., and B. Key, 2007. Neogenin: one receptor, many functions. Int J Biochem Cell Biol 39: 874-8.

Yamashita, T., B.K. Mueller, and K. Hata, 2007. Neogenin and repulsive guidance molecule signaling in the central nervous system. Current Opinion in Neurobiology 17: 29-34.

Yang, F., A.P. West, Jr., G.P. Allendorph, S. Choe, and P.J. Bjorkman, 2008. Neogenin interacts with hemojuvelin through its two membrane-proximal fibronectin type III domains. Biochemistry 47: 4237-45.

Zhang, A.S., A.P. West, Jr., A.E. Wyman, P.J. Bjorkman, and C.A. Enns, 2005. Interaction of hemojuvelin with neogenin results in iron accumulation in human embryonic kidney 293 cells. J Biol Chem 280: 33885-94.

Zhang, A.S., F. Yang, J. Wang, H. Tsukamoto, and C.A. Enns, 2009. Hemojuvelin-neogenin interaction is required for bone morphogenic protein-4-induced hepcidin expression. J Biol Chem 284: 22580-9.

Zhang, A.S., S.A. Anderson, K.R. Meyers, C. Hernandez, R.S. Eisenstein, and C.A. Enns, 2007. Evidence that inhibition of hemojuvelin shedding in response to iron is mediated through neogenin. J Biol Chem 282: 12547-56.

Zhang, A.S., F. Yang, K. Meyer, C. Hernandez, T. Chapman-Arvedson, P.J. Bjorkman, and C.A. Enns, 2008. Neogenin-mediated hemojuvelin shedding occurs after hemojuvelin traffics to the plasma membrane. J Biol Chem 283: 17494-502.

Table 1 Data collection and refinement statistics

Unit cell	Space group	$C222_1$
Cell dimensions	a, b, c (Å)	52.6, 112.9, 80.9
Data collection		
	Resolution (Å)	32.8-1.8 (1.86-1.80)
	[a]R_{merge} (%)	5.9 (37.8)
	Completeness	99.3 (98.2)
	I/σI	28.2 (4.2)
	Mean redundancy	3.8 (3.7)
	No. of unique/total reflections	22544/85823
Refinement statistics		
	Resolution (Å)	32.8-1.8
	No. reflections used	22481
	No. reflections in working/test set	21391/1090
	[b]R_{cryst}/ R_{free} (%)	20.0/23.4
No. Atoms (B factor: Å^2)		
	Protein	1577 (23.75)
	Water	293 (35.49)
RMS deviations		
	Bond length (Å)	0.010
	Angle (°)	1.596
Ramachandran plot (%)		
	Preferred	187 (96.4%)
	Allowed	7 (3.6%)
	Outlier	0 (0.0%)

[a]R_{merge} (%) = 100 × $\sum$ |I-<I>|/$\sum$I, where I is the integrated intensity of a given reflection. Numbers in parentheses are statistics for the highest resolution shell.

[b]R_{cryst} (%) = 100 × $\sum$ $|F_{obs}-F_{calc}|/\sum F_{obs}$, where the F_{obs} and F_{calc} are the observed and calculated structure factor amplitudes for all reflections in the working set.

[b]R_{free} was calculated as described for R_{cryst} but summed over the 5% of reflections that were not included in the refinement (Brunger, 1997).

Table 2. Interdomain tilt, rotation angles and buried surface area

	PDB code	Tilt (º)*	Rotation (º)	Buried surface area ($Å^2$) ***
neogenin FN5-6	TBD	169	148	501
neuroglian FN1-2	1CFB	104	172	308
fibronectin FN7-8	1FNF	129	112	601
fibronectin FN8-9	1FNF	134	158	540
fibronectin FN9-10	1FNF	157	42	338
β4 integrin	1QG3	155;156**	150;153	392
NCAM FN1-2	2VKW	57;59	140;140	530
NCAM2 FN1-2	2JLL	122	89	280
Ihog FN1-2	2IBB	42	137	1170

* Tilt angle (defined as the angle between the long axes of two adjacent domains) was calculated using the program Dom_angle (Su et al., 1998). Rotation angle (kappa in polar coordinates) was calculated using COOT by superimposing the secondary structures of the two domains.

** Two angles were calculated due to slight conformational differences between two copies of the same molecule.

*** Total buried surface areas were calculated using CCP4 program AREAIMOL and a 1.4 Å probe.

Figure legends

Figure 1. Crystal structure of neogenin FN5-6. (A) Ribbon diagram of the neogenin FN5-6 structure. N- and C-termini are labeled. β-strands A, B, and E are blue, strands C, C', F, and G are purple, polyproline helices are orange and a 3_{10} helix is green. A dashed line indicates the disordered loop missing in the final model. (B) Hydrogen bonding (dotted yellow lines) at the inter-domain interface. Oxygen atoms are red and nitrogen atoms are blue in the highlighted side-chains. (C) Electrostatic potential surfaces for neogenin FN5-6 and DCC FN5 (PDB code 2EDD). Electrostatic potentials were calculated using the APBS tool (Baker et al., 2001) and plotted from -7 kT/e (red, electronegative) to +7 kT/e (blue, electropositive).

Figure 2. Structure-based sequence alignment of the FN5-6 regions of human neogenin and DCC. (A) Sequence alignment of neogenin FN5-6 with the counterpart region of DCC (GenBank accession codes AAC51287 and NP_005206). Secondary structure elements determined from the structure of neogenin FN5-6 are indicated above the sequences (arrows for β-strands and springs for helices). Non-conserved residues representing potential interaction sites with hemojuvelin are highlighted in red, residues that are similar but not identical are highlighted in light brown, and conserved residues are not highlighted, with the exception of conserved positively-charged residues in FN5, which are marked with an asterisk. (B) Ribbon diagram and surface representation of neogenin FN5-6 using the color scheme from panel A to highlight non-conserved regions (red) as potential binding sites for hemojuvelin.

Figure 3. Hypothetical model for how interactions between neogenin FN5 and negatively-charged phospholipids on the surface of the neogenin-expressing cell could facilitate interactions between hemojuvelin on the surface of another cell and the hemojuvelin-binding site on neogenin FN6. The neogenin FN5-6 structure is shown as in Figure 1C as an electrostatic surface, with the highly positive FN5 domain (blue) interacting with negatively-charged lipids (red). The remaining domains of neogenin are represented as cyan (Ig-like domains) and pink shapes (FNIII domains). A black arrow points to the 3_{10} helix within the potential hemojuvelin binding site in the FN6 domain.

Figure 1

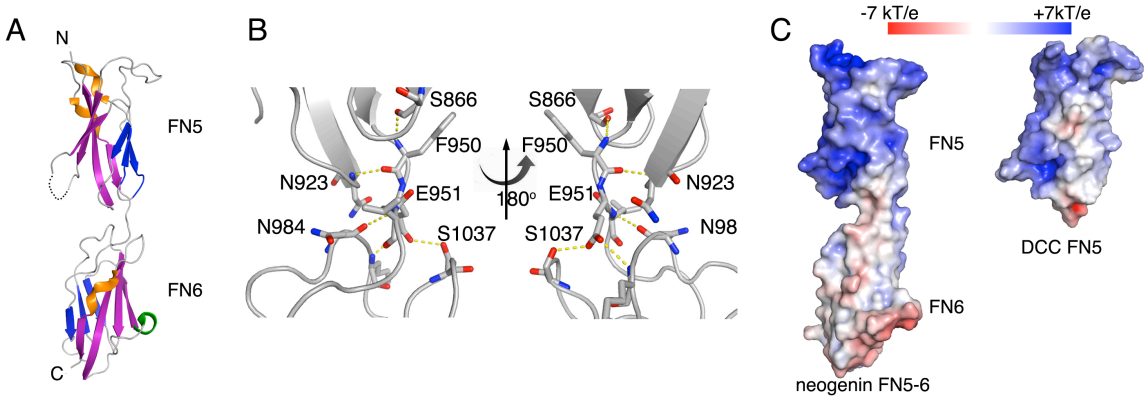

Figure 2

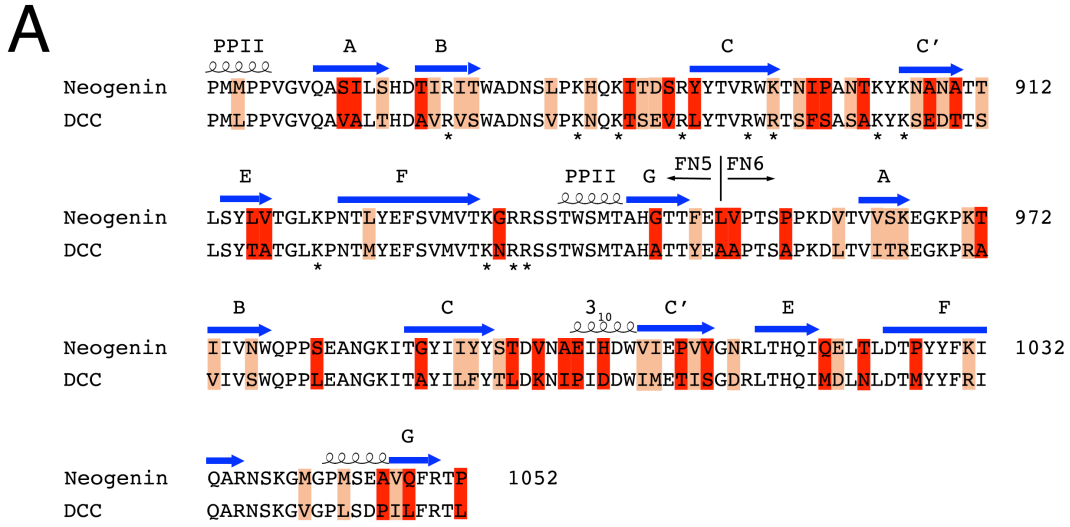

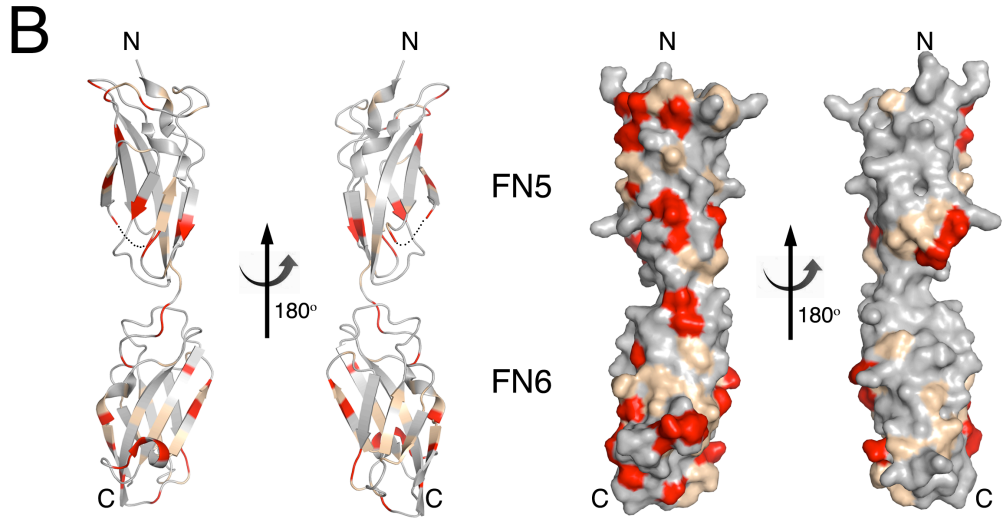

Figure 3

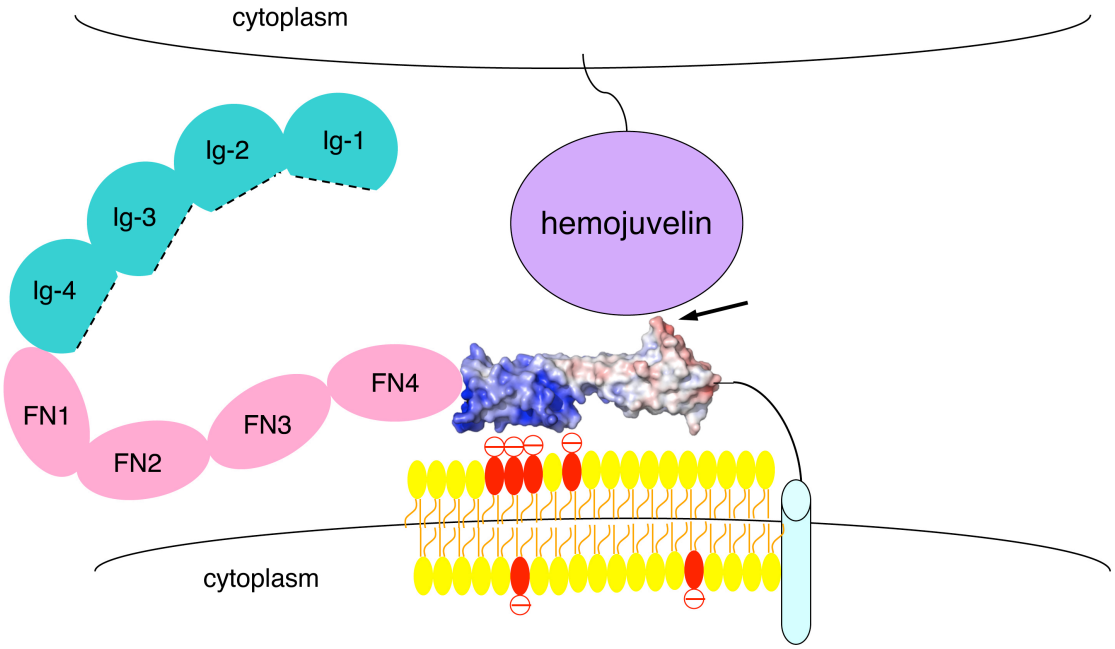
cytoplasm
Ig-1
Ig-2
Ig-3
Ig-4
hemojuvelin
FN1
FN2
FN3
FN4
cytoplasm

Supplementary Figure 1. Comparison of neogenin FN5-6 and other tandem FNIII domains in ribbon diagram (panel A) and electrostatic potential surface (panel B) representations. Coordinates are from neogenin FN5-6 (this paper), β4 integrin (PDB code 1QG3), neuroglian FN1-2 (PDB code 1CFB), NCAM FN1-2 (PDB code 2VKW), fibronectin FN7-10 (PDB code 1FNF), NCAM2 FN1-2 (PDB code 2JLL), and Ihog FN1-2 (PDB code 2IBB). Electrostatic potentials were calculated as described before in Figure 1C and plotted from -7 kT/e (red, electronegative) to +7 kT/e (blue, electropositive). The purple sphere in the neuroglian ribbon diagram represents a bound sodium ion.

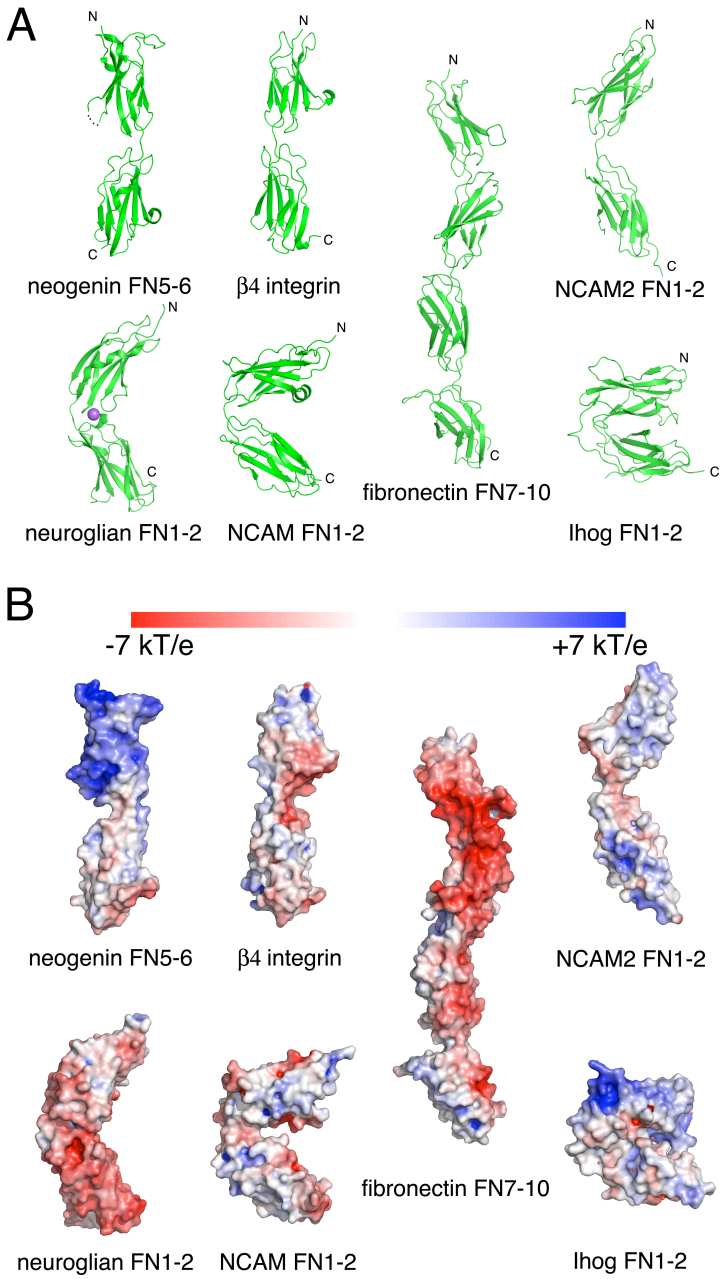

Chapter 4:

Biophysical studies of L1-mediated homophilic adhesion

Introduction

L1 is a transmembrane glycoprotein that mediates homophilic and heterophilic adhesion events in neural cell recognition (*1*). L1 is an immunoglobulin superfamily member composed of six Ig-like domains followed by five fibronectin type III (FNIII) domains, a transmembrane domain and a short but well-conserved intracellular domain (*2*). L1 interacts with various binding partners and plays important roles in neural development as well as in the adult nervous system, including neurite outgrowth, neuronal migration and survival, and synapse organization (*3, 4*). Mutants of L1 have been found to cause mental retardation, hydrocephalus, impairment of sensorimotor gating, abnormal cerebellar development, and many other phenotypes (*5*-*8*).

Studies have shown that the first four Ig domains of L1 form a horseshoe shaped structure, which has been reported to be critical in L1 homophilic adhesion (*9, 10*). Based on studies of its homologues, two models, the domain-swapped multimer model (*9*) and the zipper model (*11*), have been proposed to explain how homophilic interaction is achieved. In the domain-swapping model, transient opening of the horseshoe structure induces the formation of domain swapped dimers and multimers (Figure 4A), and the latter contains periodic adhesion sites with gaps in between. The zipper model, however, predicts a continuous linear array of horseshoes in the middle of the adjacent membranes (Figure 4B). The two models not only differ in the adhesion site pattern, but also in the inter-membrane distance. Dr. Yongning He, a postdoctoral scholar in the Bjorkman laboratory, initiated his electron microscopy studies to observe L1-mediated adhesion between liposomes and to verify or refute these models. His studies revealed a regularly spaced pattern formed by L1 molecules from neighboring membranes and found that

alterations of L1-associated carbohydrates, for example, recombinant L1 proteins from different expression systems, changed the adhesion interface, particularly the distance of adhesion sites. Based on all of these observations, he suggested a carbohydrate-modified interaction model, in which protein-protein interactions determine the *trans* interaction by pairs of horseshoe domains and carbohydrate-carbohydrate or carbohydrate-protein interactions regulate the *cis* spacing between neighboring L1 proteins on a membrane (*12*) (Figure 4C).

Additional questions regarding L1-mediated adhesion remain to be addressed. For example, what is the average binding strength between one pair of molecules (or average energies at different molecular densities)? Is there cooperativity in adhesive interactions between membranes? That is, is the total adhesion energy at an interface with 100 molecules exactly twice of that of an interaface with 50 molecules? Additionally, under physiological conditions, when L1 protein is present at relatively low densities, does an adhesion interface recruit molecules from other regions?

In order to adddress these questions, an appropriate model system is needed. Studies of membrane mechanics within the context of biology has long been a field that attracts physicists. Artificial lipid vesicles are often used as a model system for studying membrane mechanics because unlike biological membranes in cells, their lack of a cytoskeleton matrix and various membrane proteins makes it easier for researchers to understand underlying physical mechanisms and to provide important insights into complex biomembranes (*13*). Experimental and theoretical/numerical approaches have been applied to the study of red blood cell shape determination and transition (*14*),

budding (exocytosis) (*15*), and adhesion (*16, 17*). For a review of this field, please refer to (*13*).

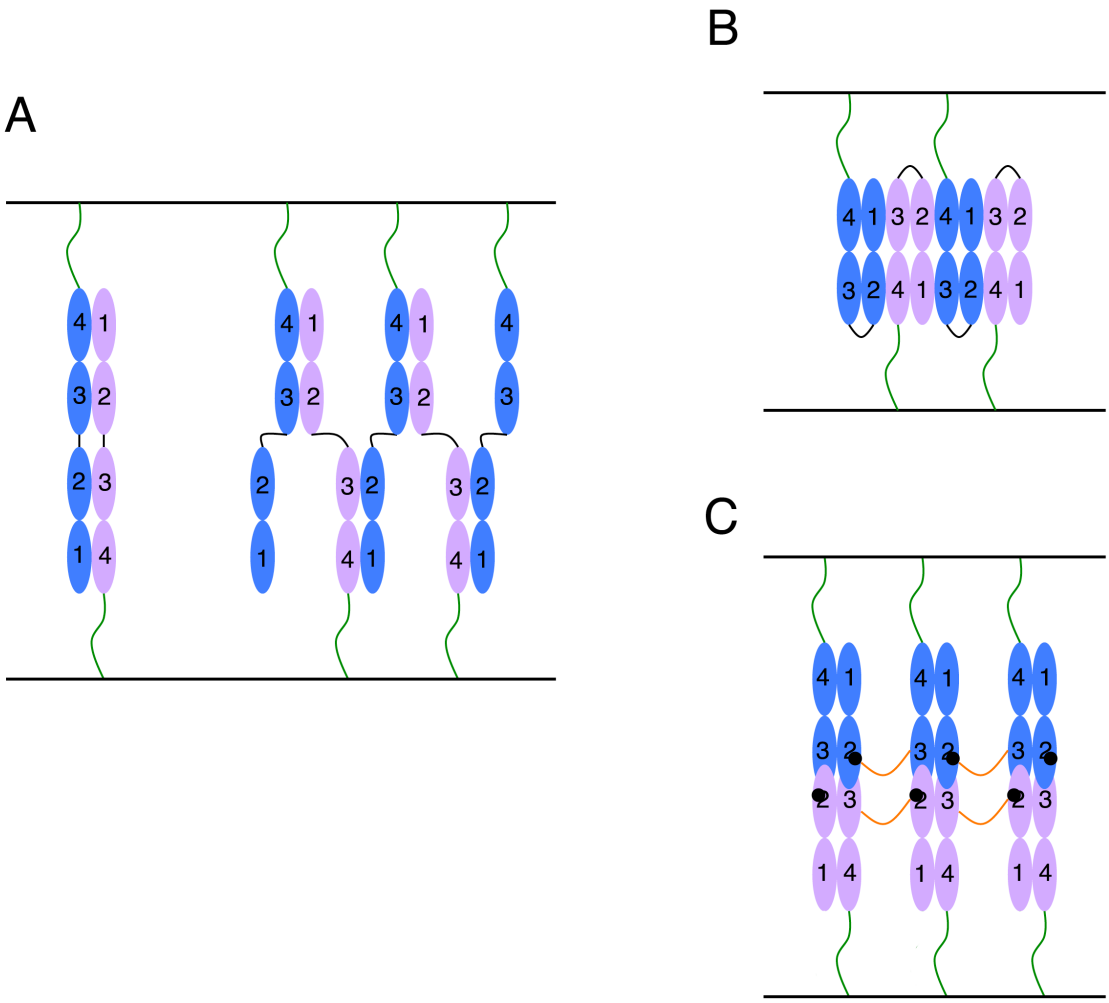

Figure 1. Three models of L1-mediated homophilic adhesion. (A) Domain-swapping model suggested by the structure of hemolin, an L1 homologue (*9*). (B) Zipper model based on the packing in crystals of axonin-1, another L1 homologue (*11*). (C) Carbohydrate-modified model proposed on the basis of electron tomography studies of L1-mediated adhesion in liposomes (*12*). Negatively-charged sialic acids on carbohydrates from one horseshoe interact with a positive patch (represented by a black dot) of a neighboring horseshoe to form a regularly spaced pattern. (Figure modified from (*12*).)

Our studies of L1-mediated adhesion have been a collaborative effort with Tristan Ursell, a former graduate student in the Phillips laboratory and now a postdoctoral scholar at Stanford. We aim to use biophysical approaches to answer the questions listed above using giant unilamellar vesicles (GUVs) as a platform. Tristan and I independently developed a basis shape model for the deformation for a GUV adhered to a flat substrate. In this general model, adhesion strength is defined on the interface but the nature of the adhesion force is not specified – it can be any interaction. Simulations were performed to show how adhesion energy density affects the shape of an adhered GUV. Experimentally, we developed a complete protocol in order to image L1-coated GUV adhering to L1-functionalized coverglass using confocal microscopy. Data processing scripts were written in order to reconstruct three dimensional shape configurations and adhesion energy density was derived from the shape profile. We also tested the applicability of a numerical simulation program, Surface Evolver, to calculate the shape of a vesicle adhering to a substrate. Although the numerical method is not amenable to the inverse problem of extracting model parameters, it did provide insight regarding the validity of our parameterized basis shape model; by fitting the simulated profile to our model, it was possible to map out the regime where the latter indeed serves as a faithful characterization of the full profile.

Materials and Methods

Molecular cloning and protein expression

A gene encoding the ectodomain of human L1 (residues M1-E1120 and a C-terminal 6x-His tag) was cloned into pcDNA3.1 vector (Invitrogen) by Yongning He as

described in (*12*). Supernatants collected from transiently-transfected 293T cells were buffer exchanged into 20 mM Tris, pH 7.4, 150mM NaCl before loading onto a Ni-NTA column (Qiagen). Eluates were further purified by size exclusion chromatography using a Superdex 200 10/30 column (GE Healthcare). Proteins were concentrated and stored at 4 °C in 20 mM Tris pH 7.4, 150 mM NaCl and 5 mM EDTA.

Preparation of giant unilamellar vesicles

1,2-Dioleoyl-sn-Glycero-3-phosphocholine (DOPC), 1,2-Dioleoyl-sn-Glycero-3-{[N(5-Amino-1-Carboxypentyl)iminodiAcetic Acid]Succinyl} (nickel salt) (DOGS-NTA-Ni), and 1,2-Dioleoyl-sn-Glycero-3-Phosphoethanolamine-N-(Lissamine Rhodamine B Sulfonyl) (Rhodmaine-PE) were purchased from Avanti Polar Lipids (Alabaster, AL). Lipid mixtures were made by mixing 5 mole % DOGS-NTA-Ni with 94.5 mole % DOPC and 0.5 mole % Rhodamine-PE to facilitate visualization. The final concentration of lipids was set to 2 mg/ml in chloroform. 2 μl lipid/chloroform solution was applied to pre-cleaned indium tin oxide (ITO) glass slide on a custom-made chamber (by Tristan Ursell) to form a thin layer. The chamber was desiccated for one hour before an ethanol-cleaned one-side-greased nitrile O-ring was carefully placed on top of the dried lipid layer. 140 μl of 220 mM sucrose solution was added in the O-ring on which the cover of the chamber was then placed. Applying 1-5V voltage at 10 Hz to the chamber for 3 hours destabilized the lipid film to form GUVs. The end product was removed from the chamber and transfer to an eppendorf tube. The quality and yield of GUVs was checked under a microscope before proceeding to the next step.

Attaching protein to GUVs and collecting confocal images

Protein samples were exchanged into buffer containing 20mM Tris, 100mM NaCl before use (EDTA in the storage buffer needed to be removed to ensure that the His-tagged protein bound efficiently to the Ni-NTA head groups). Copper NTA functionalized glass cover-slips were obtained from MicroSurfaces, Inc. The GUV stock was diluted by 10 fold in 20mM Tris, 100mM NaCl. Wildtype L1 (or a negative control His-tagged protein, scFv b12, courtesy of Rachel Galimidi) was incubated separately with the functionalized glass cover-slip and the diluted GUVs for 40 minutes in order to attach the His-tagged protein on both surfaces through His-tag metal-NTA chelation. L1-decorated GUVs were then incubated with the glass coverslips to allow the adhesion of GUVs onto the bottom of the coverslip. After 20 minutes of incubation, samples were placed on the stage of Perkin-Elmer Ultraview spinning disk microscope and confocal images were recorded using a 100X oil-immersed objective (αPlan-APOCHROMAT 1.46 Oil DIC, Zeiss) with 568nm laser as the excitation source. 3-D confocal stacks were sampled at 0.2 μm spacing in z direction with 200 milliseconds exposure time for each image.

Data analysis with Matlab

The following steps summarize how to extract an adhesion energy from z-stack images of a vesicle adhering to a flat surface.

(1) Format conversion

The confocal z-stack images had to be converted to TIFF using ImageJ PerkinElmer plugin in batch model. These images correspond to a series of optical sections covering the whole vesicle.

(2) Determination of axis of revolution

The images from the equatorial region of the vesicle normally have the best image quality in terms of signal to background ratio. It is thus possible to choose a threshold to convert the grayscale image to binary format, which displays background as black and the lipid bilayer as white. A circle could be fit using those points corresponding to the bilayer. Due to the high signal to background ratio, the exact choice of the threshold value did not have a significant impact on the fitting result. Ten images from the equatorial region were analyzed this way, and the coordinates of the center of the fitted circles were averaged to give the position of the revolution axis of the vesicle.

(3) Determination of shape profile

For images far from the equatorial region, it was difficult to find a threshold to differentiate bilayer and background; the vesicle boundary appeared to be a thick circle. In order to increase the signal to background ratio, a self-averaging approach, based on the axisymmetric property of the vesicle, was employed. To be specific, the image was divided into a series of concentric circular shells around the axis of revolution determined in the previous step. The average grayscale value in each shell was calculated and plotted as a function of its radial distance from the center. The peak of this radial profile indicated the position of vesicle boundary for this z-section.

(4) Determination of the geometric parameters

For each radial profile, a threshold was chosen as the maximum intensity minus the background. Points above that threshold had radial coordinates approximately the same as the radius of the vesicle at the z-section. Note that the z positions were corrected as described in detail in the next section (*Refractive index mismatch correction*). These experimentally determined vesicle profile points were used to determine the geometric parameters characterizing the vesicle shape. In particular, the theoretical profile of the vesicle is completely determined by three important parameters, namely, R_3, λ, and θ_c (for details of the model, see Figure 2). Given the experimental profile, a three-parameter search was carried out to find a set of parameters that minimized the square difference between the theoretical and the experimental points. Due to the existence of local minima, many random points in the three-dimensional parameter space were chosen as starting points of the optimization process. The theoretical curve based on the optimized parameters was checked visually against the experimental data as shown in the lower left corner of Figure 2.

(5) Determination of adhesion energy

In the adhesion model, the three geometric parameters are obtained by minimizing the system free energy given the adhesion energy, bilayer bending modulus, vesicle area and reduced volume. It is thus possible for us to deduce the adhesion energy using the parameters obtained in step 4. Furthermore, the vesicle area and reduced volume are fixed by a given set of shape parameters (R_3, λ, and θ_c) when the bilayer bending modulus for the DOPC lipid (the major component in our lipid mixture) is known. So the problem reduces to a one-dimensional search in the space of adhesion energy to

get the best agreement between geometric parameters determined from experiments and theory.

Refractive index mismatch correction

In order to reconstruct the three-dimensional shape of an adhered vesicles, the exact position along the z-axis is indispensable. Due to the difference of refractive indices between the cover-slip/immersion oil (n=1.52) and the imaging medium (here 20 mM Tris, pH 7.4, 100 mM NaCl, with n=1.34 (*18*)), the actual position of the focal plane differs from its nominal position since the direction of light changes as it enters the second medium from the first one. This effect worsens as the distance from the objective increases. For a thin specimen (less than 3 μm) or only minor differences in refractive indices between immersion and imaging media (for example, n_1=1.46, n_2=1.52), a linear correction factor can be used to account for the effects resulting from refractive index mismatch (*19*). In our case, the GUVs ranged from a few microns to tens of microns. Therefore, single parameter correction method was not appropriate. For every single confocal image, the position of actual focal plane was calculated based on a theory developed by Egner and Hell (*20*). The Matlab script for the correction is included in Appendix C.

Simulation using Surface Evolver

The initial shape is a cube on a flat surface and the bottom of the cube is confined to be on the surface. The vertices, edges, faces and body are defined, and the evolution of the vesicle shape is controlled by two energies: adhesion energy and bending energy. The

total area and total volume are fixed during evolution. The surface is first coarsely triangulated during the initial steps of evolution. After the shape starts to stabilize, the surface triangularization is refined to get finer details of the shape. The evolution sequence is normally composed of steps of first-order gradient search, facet management, refinement, and second-order Hessian search. The first-order gradient algorithm is robust but slow, so it is used to get close to the equilibrium point and provide a good starting point for second-order Hessian search. Facet management is required to get rid of extremely small edges and adjust the facet sizes to make them more uniform; robust calculation of curvature relies on this procedure. The grid density is adjusted by refinement to achieve the desired spatial resolution.

Results and Discussions

Parameterized basis shape model

As summarized in a classic review published in 1997 (*13*), there are three approaches that are often used to find the vesicle shape with the lowest energy: solving Euler-Lagrange equations, applying variational method to trial shapes, and minimizing the energy numerically on triangulated surfaces. We chose the second approach due to its relative simplicity, both analytically and numerically. The first method was attempted while I tried to repeat the results by Seifert in the two-dimensional adhering vesicle case (*17*) but the extension to three dimensions is nontrivial. The third strategy was later used to verify the validity of the current approach and will be described in later paragraphs.

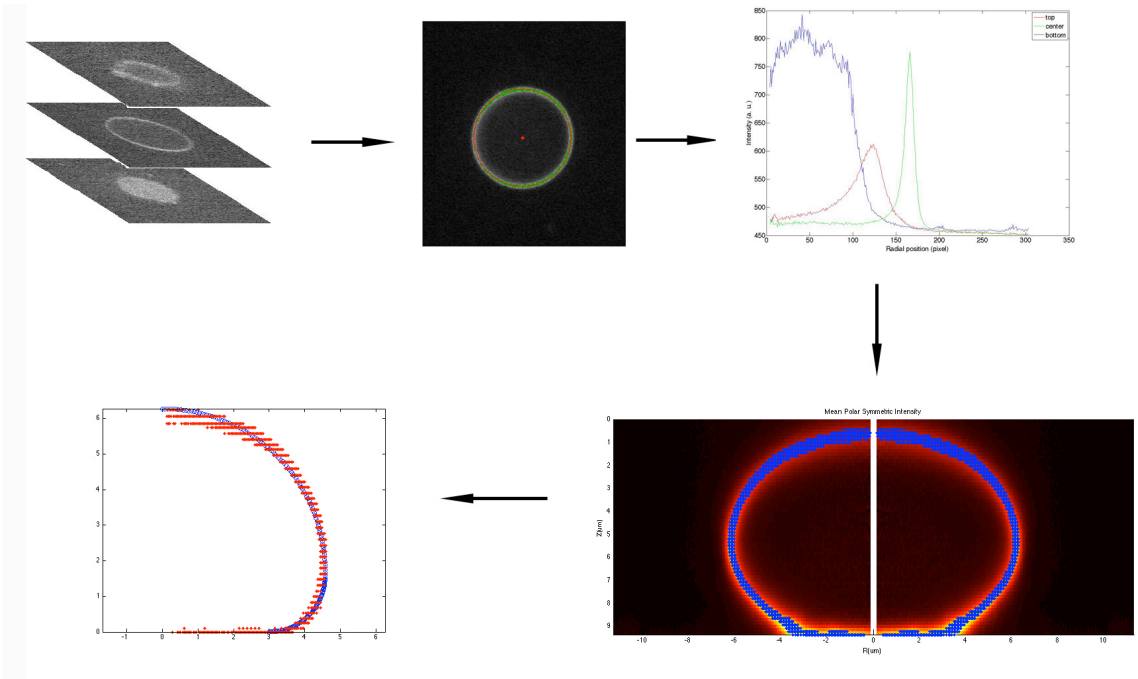

Figure 2. Flow chart showing how the confocal images were processed. Clockwise from top left: stacks of raw images, fitting equatorial data to find the revolution axis, plotting self-averaging intensity profile, extracting data points (blue) from background, fitting the data points to a 3-parameter shape profile.

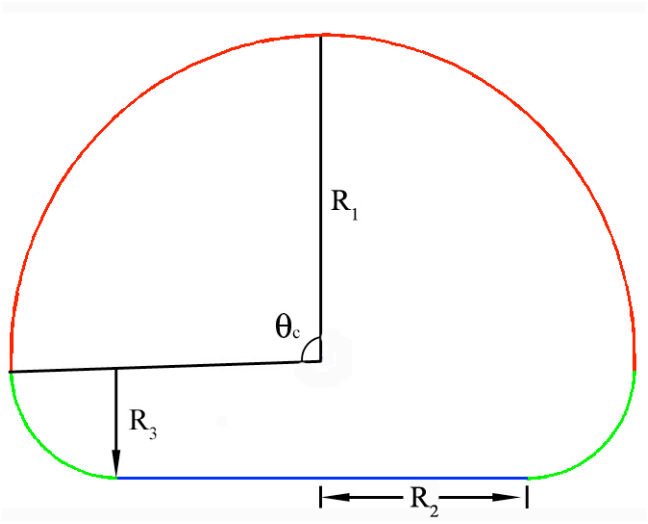

Figure 3. Schematic view of a vesicle adhering to a flat surface with the geometric parameters defined.

For simplicity, we consider a vesicle adhering to a flat surface. Due to the axisymmetric nature of the problem, one can use a cross section along the revolution axis to represent the 3-D object. Assume the initial state is a free GUV with total volume V_0 and total area A_0 ($A_0=4\pi R_0^2$, where R_0 is called characteristic length) and the final state is pictured below in Figure 3, parameterized by three radii R_1, R_2, R_3 and one angle θ_c. An adhered vesicle can be characterized by three regions: a spherical cap (in red), a adhering base (blue), and the connecting segment (green). Due to the boundary conditions, one radius can be expressed in terms of the other three parameters, leaving only three independent variables to fully describe the system. Let $\cos\theta_c=c$, and introduce $\lambda=R_2/R_3$, then we have

$$\begin{aligned} R_2 &= \lambda R_3 \\ R_1 &= R_3\left(\frac{\lambda}{\sqrt{1-c^2}}+1\right) \end{aligned}.$$

Now the system can be completely described by R_3, λ, and c. The total area and total volume can be expressed as

$$\begin{aligned} A &= A_{ba}+A_{sc}+A_{co} \\ &= \pi R_2^2 + 2\pi R_1^2(1-c) + 2\pi R_3[R_2\arccos(-c)+R_3(1+c)] \\ &= \pi R_3^2\left[\lambda^2+\frac{2(\lambda+\sqrt{1-c^2})^2}{1+c}+2\lambda\arccos(-c)+2(1+c)\right], \end{aligned}$$

$$\begin{aligned} V &= \frac{2}{3}\pi R_3^3\left(\frac{\lambda}{\sqrt{1-c^2}}+1\right)^3(1-c)+\frac{\pi}{3}R_3^3(\lambda+\sqrt{1-c^2})^2\left(\frac{\lambda}{\sqrt{1-c^2}}+1\right)(-c) \\ &\quad +\pi\times\left[(1+c)\lambda^2R_3^3+c\sqrt{1-c^2}\lambda R_3^3+(1+c)^2R_3^3-\frac{1}{3}(1+c)^3R_3^3+2\lambda R_3^3\arcsin\sqrt{\frac{1+c}{2}}\right]. \end{aligned}$$

The bending energy can be calculated as a summation of the contributions from the spherical cap and the connecting region

$$
\begin{aligned}
E_{bending} &= E^{sc}_{bending} + E^{co}_{bending} \\
&= \frac{\kappa}{2}\int_0^{2\pi} d\phi \int_0^{\theta_c} (\frac{2}{R_1})^2 R_1^2 \sin\theta d\theta + \frac{\kappa}{2}\int_0^{2\pi} d\phi \int_{\theta_c}^{\pi} (K_1+K_2)^2 R_3(R_2+R_3\sin\theta) d\theta \\
&= 4\pi\kappa(1-c) + \kappa\pi \int_{\theta_c}^{\pi} (\frac{1}{R_3} + \frac{\sin\theta}{R_2+R_3\sin\theta})^2 R_3(R_2+R_3\sin\theta) d\theta \\
&= 4\pi\kappa(1-c) + \kappa\pi \int_{\theta_c}^{\pi} \frac{(R_2+2R_3\sin\theta)^2}{R_3(R_2+R_3\sin\theta)} d\theta
\end{aligned}
$$

where K_1 and K_2 are the principal curvatures of the local surface. By definition, $R_2=\lambda R_3$, the bending energy becomes

$$E = 4\pi\kappa(1-c) + \kappa\pi \int_{\theta_1}^{\pi} \frac{(\lambda+2\sin\theta)^2}{(\lambda+\sin\theta)} d\theta .$$

Depending the value of λ, the above integral has analytical form as following:

$$
\begin{aligned}
\lambda > 1, I &= 4(1+c) + \frac{\lambda^2}{\sqrt{\lambda^2-1}} \left(\pi - 2\arctan\left(\frac{1+\lambda\sqrt{(1-c)/(1+c)}}{\sqrt{\lambda^2-1}}\right)\right) \\
\lambda = 1, I &= 4(1+c) + \frac{2}{1+\sqrt{\frac{1-c}{1+c}}} \\
\lambda < 1, I &= 4(1+c) + \frac{\lambda^2}{\sqrt{1-\lambda^2}} \log\left(\frac{(1+\sqrt{1-\lambda^2})(\lambda+\sqrt{1-c^2})}{\lambda(1-c\sqrt{1-\lambda^2}+\lambda\sqrt{1-c^2})}\right)
\end{aligned}
$$

We assume that both the total volume and area are conserved (due to balanced osmolarity and extremely high energy cost to stretch a bilayer), now the question becomes how to minimize the total energy expressed in three variables under both area ($A=A_0$) and volume constraints ($V=V_0$):

$$
\begin{aligned}
E &= E_{bending} + E_{adhesion} \\
&= \frac{\kappa}{2}\oint (K_1+K_2)^2 dA - WA^*
\end{aligned}
$$

Here W is the adhesion strength per unit area while A* is the area of the adhesion plane.

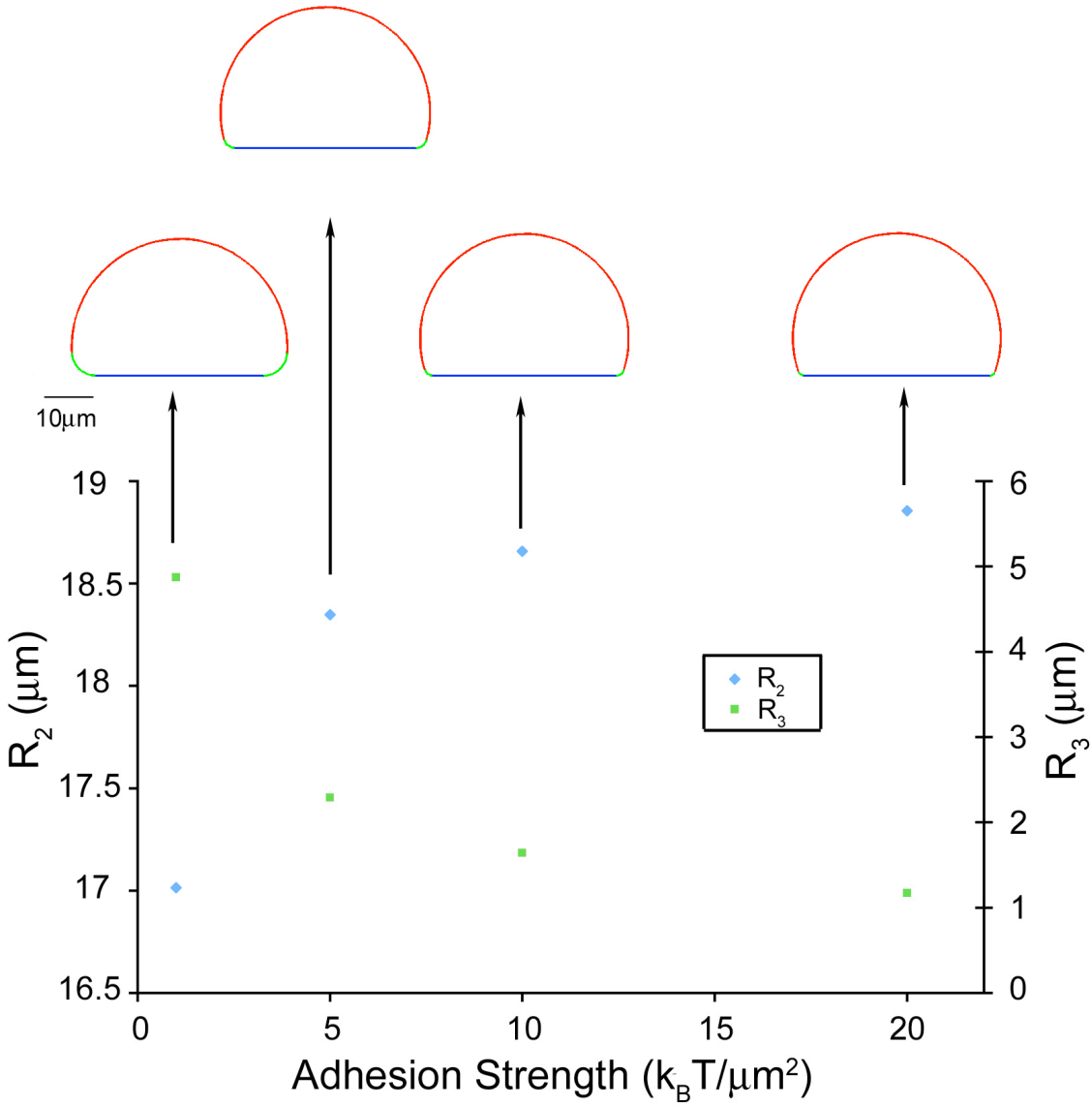

Figure 4. Representative simulation results based on energy minimization shows how the shape changes as adhesion strength increases. R_2 (blue, left axis) and R_3 (green, right axis) are plotted as functions of adhesion energy. The coloring scheme is the same in vesicle shape plots on the top of each set of data points (R_1 red, R_2 blue, and R_3 green). The initial state of the vesicle is represented by R_0=20 μm and reduced volume σ=0.9 while the bilayer bending modulus is κ=20 k_BT for DOPC bilayers (*21*).

Now that the model is complete, for any given adhesion strength W and initial volume and area, one can obtain a configuration (set of R_3, λ, and c) that gives minimal total energy. Inverting the problem, one can start from a final configuration and deduce the adhesion strength W. The latter case is what really happens in the experiments – one can take confocal images of an adhering vesicle, reconstruct its three-dimensional configuration, and then calculate the corresponding adhesion strengths, which we are interested in. Before collecting experimental data, I did a few rounds of simulations to calculate the shapes of typical sized GUVs under different adhesion strengths (Figure 4). What the simulation results tell us is that under high adhesion strength, the shape change becomes minimal so that one cannot confidently resolve the differences (for example, see the green regions of vesicles at adhesion strengths 10 and 20 $k_BT/\mu m^2$). In this case, one can still an obtain adhesion strength from experimental data but the confidence interval will be too big to be meaningful.

Deduction of adhesion strength from experimental data

With the model complete, we then proceeded to perform the adhesion experiments. Following the protocol in the Materials and Methods (see Figure 5A for the electroformation chamber), we generated GUVs with diameters ranging from a few microns to tens of microns (Figure 5B). After adding L1 protein and incubating for 30 minutes, the GUVs deformed significantly (Figure 5C and 5D). A strong rhodamine signal, created by two contacting membranes, was observed at the adhesion interface.

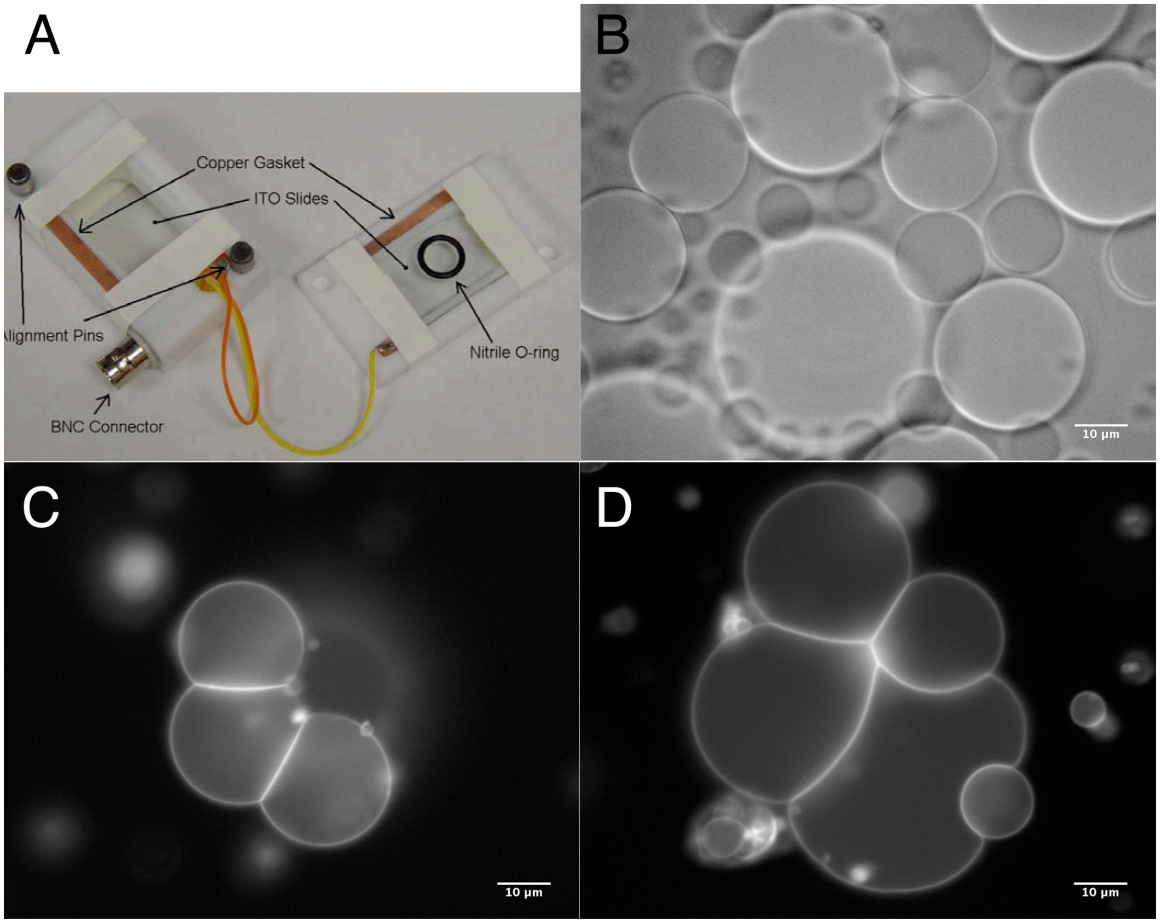

Figure 5. L1 adhesion induces significant deformations in adhering GUVs. (A) Electroformation chamber for GUV production (courtesy of Tristan Ursell). (B) DIC image of raw GUVs (before addition of L1) made from 5 mole % DOGS-NTA, 94.5% DOPC and 0.5% Rhodamine-PE. (C) and (D) fluorescent images of L1-mediated adhesion/deformation under rhodamine channel. All Scale bars are 10 µm.

Now that it was confirmed that adhesion could be observed on GUVs, we moved on to an experimental setup that mimics our model. As described in the Materials and Methods section, both GUVs and copper-NTA functionalized coverglass were incubated with L1 separately, and then the two were combined. We controlled the GUV density so that vesicle-vesicle adhesion was rarely observed and vesicle-coverglass adhesion was predominant. The sample was then imaged with a confocal microscope and stacks of images were taken on adhered GUVs along the z-axis, as described in the Materials and Methods section. The cross section of a typical adhered GUV is shown in Figure 6A; a negative control, in which no adhesion zone was observed, is shown in Figure 6B.

Data processing was carried out as described in the Materials and Methods section. At the end of this procedure, one set of parameters (R_3 λ c) is obtained using least square minimization to characterize the observed profile. Deriving adhesion energy from geometric parameters is simply the inverse problem of what was described in the previous simulation section. Calculated shape parameters and deduced adhesion energy densities from four different data sets are listed in Table 1 (see Figure 6C for fitting). These vesicles all had reduced volumes approaching unity, indicating that they were nearly spherical before adhesion occurred. This is consistent with the fact that the osmolarity difference between the inside and outside of vesicles was minimal because we used solutions of matching osmolarity to prepare and dilute the vesicles. The adhesion density varies greatly with vesicle size without an obvious trend. Obtaining more data may help reduce the confidence interval of the average adhesion energy density. It is also possible that adhesion energy does depend on the vesicle

size in a nontrivial way. One might think the redistribution of L1 molecule on GUV surface is able to cause the effect as long as the entropy cost can be compensated by adhesion. This hypothesis is based on the assumption that L1 protein is sparse enough on surface so that the adhesion zone needs more molecules to form. However, an analysis of the sizes of lipid molecule and L1 protein does not seem to support this theory. A lipid molecule normally occupies 0.25 nm^2 on surface (*22*) while a typical Ig domain or FNIII domain measures 3 nm in diameter and 5 nm along the long axis (data derived from crystal structures). This means that if the bilayer contains 5% DOGS-NTA as in our experiment, there are 5.7 DOGS-NTA molecules per the space one L1 molecule fills up. Since either the density of DOGS-NTA lipids or the steric effect of L1 itself determines the L1 density on GUV surface, it seems that there is no need for the adhesion zone to recruit L1 molecules from other regions of the GUV.

Table 1: Summary of information during data processing

	022409#2	022409#4	022409#5	022409#8
Data file	022409#2_stacks	022409#4_stacks	022409#5_stacks	022409#8_stacks
No. of images used	66	63	63	39
Centering images[1]	35-45	30-40	35-45	15-22
Data extraction threshhold[2]	1.3	1.3	1.8	1.5
No. of extracted data points	673	418	487	299
Index of best fit parameters	8	23	38	29
Error of best fit	0.0177	0.0153	0.0094	0.0116
Best fit parameters (R_3, λ, c)	(4.1860, 0.4654, 0.0503)	(3.1063, 0.4567, 0.0481)	(1.5555,1.9417, -0.0413)	(1.6210, 0.8669, 0.0980)
Total area A_x	435	237	226	100
Reduced volume Sigma_x	0.989	0.989	0.935	0.969
Center of spherical cap	(0, 4.09)	(0, 3.04)	(0, 1.68)	(0, 1.48)
Center of connecting region	(1.95, 4.19)	(1.42, 3.11)	(3.02, 1.56)	(1.41, 1.62)
Adhesion strength W[3]	1.3	2.4	9.1	7.9
Min f(x) during finding W	0.01423	0.01411	0.01915	0.00283

[1] Centering images were used to determine the axis of revolution.

[2] A pixel is considered to be a data point when its fluorescent value is greater than the mean value of fluorescence intensities for the current image plus the threshold times the standard deviation.

[3] The unit of adhesion strength W is $k_BT/\mu m^2$. The bending modulus was taken as 20 k_BT when calculating the adhesion strength. The unit of length is μm unless specified otherwise.

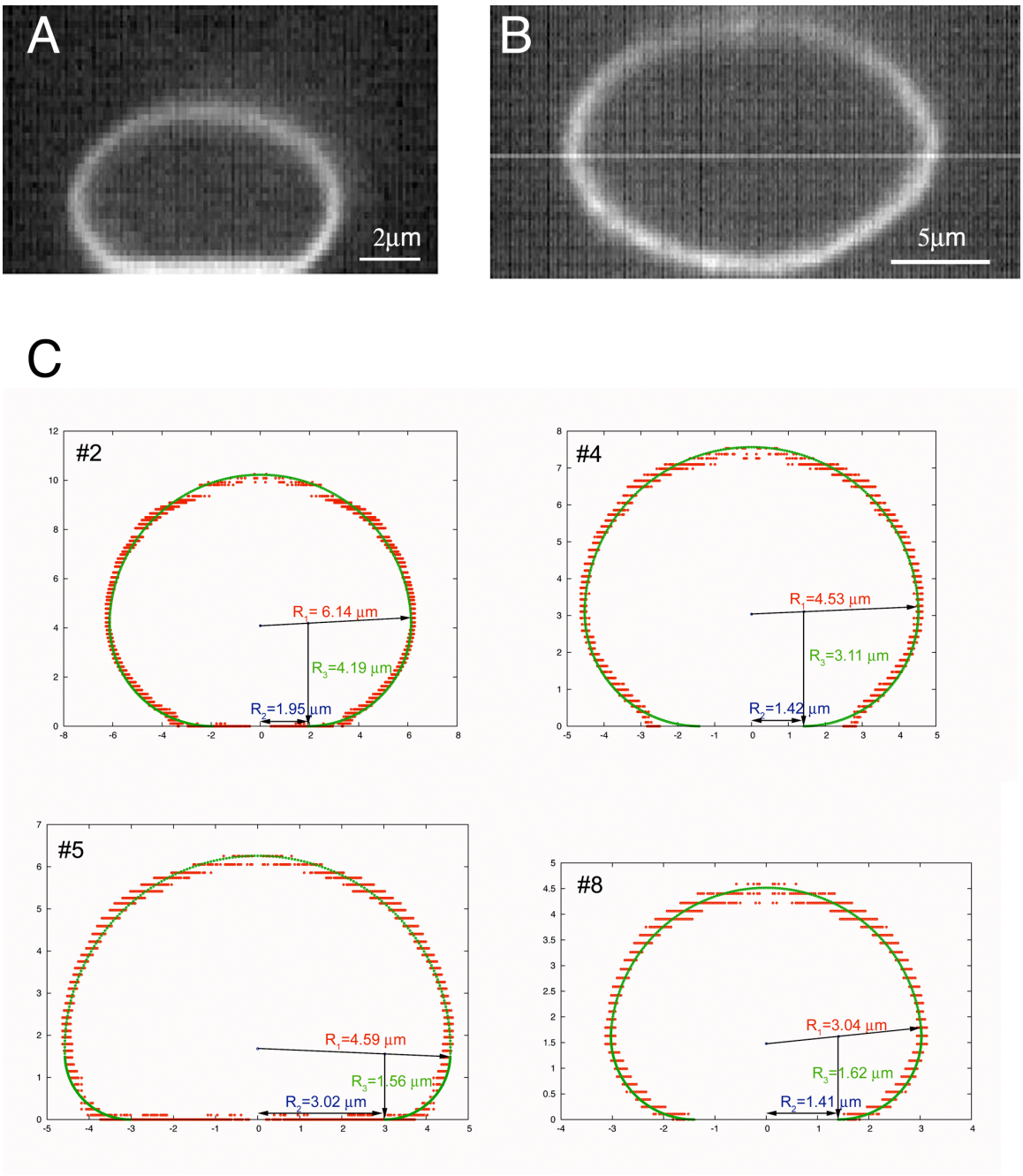

Figure 6. L1-mediated adhesion imaged by confocal microscopy. (A) Cross-section along yz plane of a GUV incubated with L1. (B) Cross section along yz plane of a GUV incubated with a control protein. Please note that z positions in A and B were not corrected with refractive index mismatch corrections. (C) Extracted confocal data (red) vs. fitting using our basis shape model (green) for all four data sets. The derived geometric parameters are shown in each panel and in Table 1.

Finally, the validity of the parameterized model should be verified to ensure the model was sufficient to describe the system under our experimental conditions. The next section describes my work on the validation of the basis shape model by checking it against numerically simulated profiles using Surface Evolver.

Surface evolver as a verification tool for the basis shape model

Surface Evolver (http://www.susqu.edu/brakke/evolver/) is a widely-used interactive software to simulate the shape statics of an object under mechanical forces (*23*). The software finds the optimal shape of an object by minimizing the total energy of the system. Normally, a user provides an initial shape and specifies the functional forms of various energies, and Surface Evolver then evolves the object shape along the gradient the energy hypersurface. The typical process of evolution is shown in Figure 7 and one can see how a cube becomes an adhered vesicle under the force determined by the gradient of the energy functional. Researchers have successfully applied this methodology in studying the formation of multicellular aggregates (*24*).

Surface Evolver simulation was carried out for different reduced adhesion strengths ($\gamma=WR_0^2/2\kappa$, in which W is the adhesion strength, R_0 is the characteristic length, and κ is the bending modulus). The numerical profile of deformed vesicles at γ=1, 2, 5, 10 were fitted to the basis shape model to evaluate its applicability. The comparison between the numerical result and the best fit model is shown in Figure 8. Qualitatively, vesicles under stronger adhesion (γ=5 and γ=10) seemed to be approximated better by the basis shape model. It should be noted that the numerical simulations are not always stable, especially for large adhesion strengths.

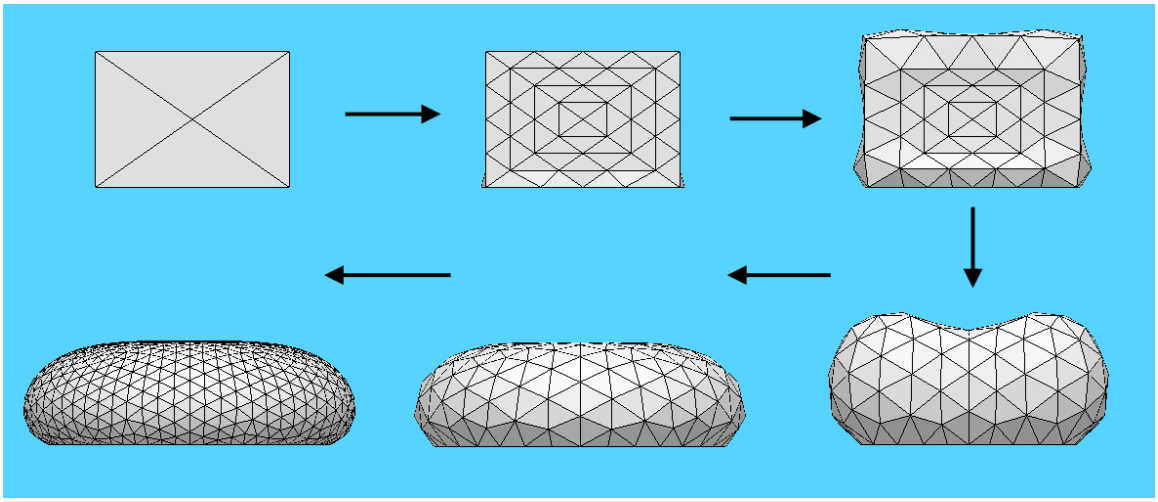

Figure 7. Typical evolution of a vesicle adhered to a flat substrate (total area A=6, total volume V=1, reduced volume $\sigma=V/[4\pi/3)(A/4\pi)^{3/2}=0.72]$.

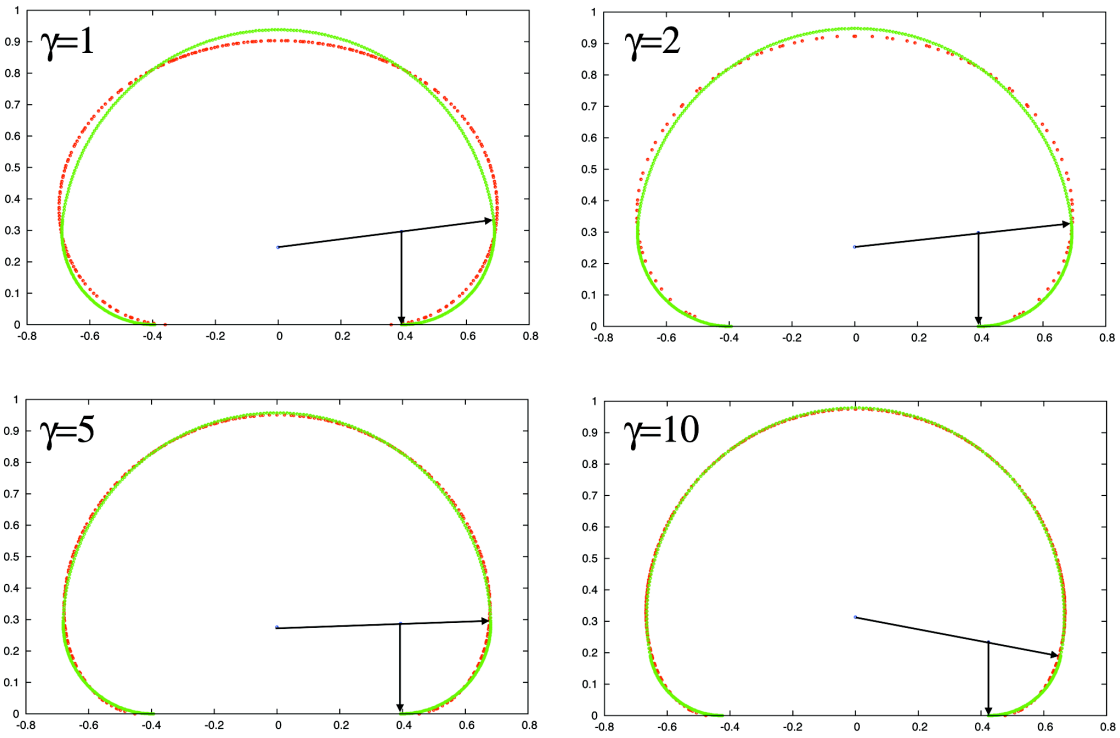

Figure 8. Comparison of numerical results by Surface Evolver (red) and best fitting using basis shape model. In all cases the reduced volume is 0.95, which is comparable with that in our experiment.

Future Directions

L1-GFP enables the direct visualization of L1 on GUVs

We described our observation of GUVs adhering to flat surface by monitoring the rhodamine signal within the lipid bilayer. However, this method does not give any information on the distribution of L1 protein on GUV surface and thus would not allow assessment of potential L1 relocalization once adhesion zone is initiated, one of the questions we aim to answer. In order to visualize the L1 protein, we designed a construct that has a GFP fused to the C-terminus of the L1 ectodomain. This protein, L1-GFP, was successfully expressed in mammalian cells and purified following the protocol used previously for L1 and its fluorescent signal was confirmed (Figure 9A). L1-GFP has also been proven to mediate adhesion between GUVs (Figure 9B). Therefore, we have now a tool to visualize the bilayer and the localization of L1 protein within the bilayer. We also tested the attachment of L1-GFP on copper-NTA functionalized coverglass and observed a fluorescent signal. After photobleaching, this signal did not recover (data not shown), indicating that this signal indeed came from immobilized L1-GFP, rather than residual protein in the aqueous phase.

Manipulation of lipid composition has proven to be feasible

Currently we use a lipid mixture containing 5% DOGS-NTA, which determines the maximum number of His-tagged L1 proteins the GUV can possibly attach. One possible assay is to monitor the GUV shape profiles while changing the percentage of DOGS-NTA lipids. We successfully made GUVs with 10% and 20% DOGS-NTA (Figure 10). However, lipid mixtures containing 50% DOGS-NTA failed to generate any GUVs.

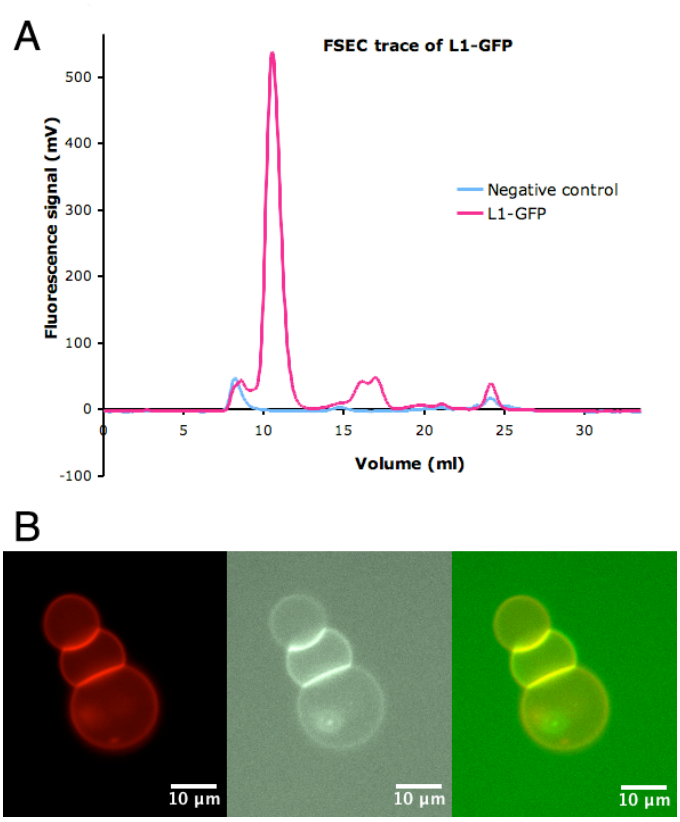

Figure 9. Recombinant L1-GFP is fluorescent and is able to induce vesicle deformation during adhesion. (A) Fluorescence size exclusion chromatography (FSEC) trace of purified L1-GFP. (B) GUV adhesion imaged under both rhodamine (left) and GFP (middle) channels, and the overlay of the two (right).

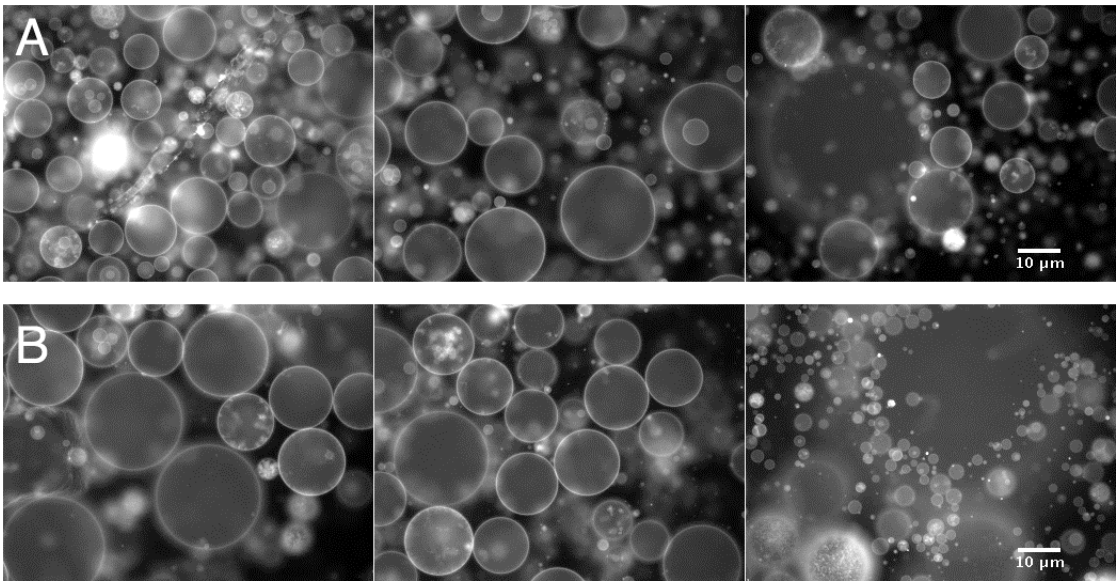

Figure 10. Successful production of GUVs from different lipid composition. (A) GUVs made from 10% DOGS-NTA. (B) GUVs made from 20% DOGS-NTA.

References:

1. Maness, P. F., and Schachner, M. (2007) Neural recognition molecules of the immunoglobulin superfamily: signaling transducers of axon guidance and neuronal migration, *Nat Neurosci 10*, 19-26.

2. Moos, M., Tacke, R., Scherer, H., Teplow, D., Fruh, K., and Schachner, M. (1988) Neural adhesion molecule L1 as a member of the immunoglobulin superfamily with binding domains similar to fibronectin, *Nature 334*, 701-703.

3. Brummendorf, T., Kenwrick, S., and Rathjen, F. G. (1998) Neural cell recognition molecule L1: from cell biology to human hereditary brain malformations, *Curr Opin Neurobiol 8*, 87-97.

4. Huang, Z. J. (2006) Subcellular organization of GABAergic synapses: role of ankyrins and L1 cell adhesion molecules, *Nat Neurosci 9*, 163-166.

5. Cohen, N. R., Taylor, J. S., Scott, L. B., Guillery, R. W., Soriano, P., and Furley, A. J. (1998) Errors in corticospinal axon guidance in mice lacking the neural cell adhesion molecule L1, *Curr Biol 8*, 26-33.

6. Kenwrick, S., Watkins, A., and De Angelis, E. (2000) Neural cell recognition molecule L1: relating biological complexity to human disease mutations, *Hum Mol Genet 9*, 879-886.

7. Irintchev, A., Koch, M., Needham, L. K., Maness, P., and Schachner, M. (2004) Impairment of sensorimotor gating in mice deficient in the cell adhesion molecule L1 or its close homologue, CHL1, *Brain Res 1029*, 131-134.

8. Wiencken-Barger, A. E., Mavity-Hudson, J., Bartsch, U., Schachner, M., and Casagrande, V. A. (2004) The role of L1 in axon pathfinding and fasciculation, *Cereb Cortex 14*, 121-131.

9. Su, X. D., Gastinel, L. N., Vaughn, D. E., Faye, I., Poon, P., and Bjorkman, P. J. (1998) Crystal structure of hemolin: a horseshoe shape with implications for homophilic adhesion, *Science 281*, 991-995.

10. Schurmann, G., Haspel, J., Grumet, M., and Erickson, H. P. (2001) Cell adhesion molecule L1 in folded (horseshoe) and extended conformations, *Mol Biol Cell 12*, 1765-1773.

11. Freigang, J., Proba, K., Leder, L., Diederichs, K., Sonderegger, P., and Welte, W. (2000) The crystal structure of the ligand binding module of axonin-1/TAG-1 suggests a zipper mechanism for neural cell adhesion, *Cell 101*, 425-433.

12. He, Y., Jensen, G. J., and Bjorkman, P. J. (2009) Cryo-electron tomography of homophilic adhesion mediated by the neural cell adhesion molecule L1, *Structure 17*, 460-471.

13. Seifert, U. (1997) Configurations of fluid membranes and vesicles, *Advances in Physics 46*, 13-137.

14. Svetina, S., and Zeks, B. (1989) Membrane Bending Energy and Shape Determination of Phospholipid-Vesicles and Red Blood-Cells, *European Biophysics Journal with Biophysics Letters 17*, 101-111.

15. Miao, L., Seifert, U., Wortis, M., and Dobereiner, H. G. (1994) Budding Transitions of Fluid-Bilayer Vesicles - the Effect of Area-Difference Elasticity, *Physical Review E 49*, 5389-5407.

16. Seifert, U., and Lipowsky, R. (1990) Adhesion of Vesicles, *Physical Review A 42*, 4768-4771.

17. Seifert, U. (1991) Adhesion of Vesicles in 2 Dimensions, *Physical Review A 43*, 6803-6814.

18. (1999) CRC handbook of chemistry and physics, Chapman and Hall/CRCnetBASE, Boca Raton, FL.

19. Huang, B., Jones, S. A., Brandenburg, B., and Zhuang, X. (2008) Whole-cell 3D STORM reveals interactions between cellular structures with nanometer-scale resolution, *Nat Methods 5*, 1047-1052.

20. Egner, A., and Hell, S. W. (1999) Equivalence of the Huygens-Fresnel and Debye approach for the calculation of high aperture point-spread functions in the presence of refractive index mismatch, *Journal of Microscopy-Oxford 193*, 244-249.

21. Fa, N., Lins, L., Courtoy, P. J., Dufrene, Y., Van Der Smissen, P., Brasseur, R., Tyteca, D., and Mingeot-Leclercq, M. P. (2007) Decrease of elastic moduli of DOPC bilayers induced by a macrolide antibiotic, azithromycin, *Biochim Biophys Acta 1768*, 1830-1838.

22. Phillips, R., Kondev, J., and Theriot, J. (2009) *Physical biology of the cell*, Garland Science, New York.

23. Brakke, K. A. (1996) The surface evolver and the stability of liquid surfaces, *Philosophical Transactions of the Royal Society of London Series a-Mathematical Physical and Engineering Sciences 354*, 2143-2157.

24. Ziherl, P., and Svetina, S. (2007) Flat and sigmoidally curved contact zones in vesicle-vesicle adhesion, *Proceedings of the National Academy of Sciences of the United States of America 104*, 761-765.

Appendix A

Published as Zhang AS, Yang F, Meyer K, Hernandez C, Chapman-Arvedson T, Bjorkman PJ, Enns CA. (2008) Neogenin-mediated Hemojuvelin Shedding Occurs after Hemojuvelin Traffics to the Plasma Membrane. *Journal of Biological Chemistry* **283**(25):17494-502.

THE JOURNAL OF BIOLOGICAL CHEMISTRY VOL. 283, NO. 25, pp. 17494–17502, June 20, 2008

Neogenin-mediated Hemojuvelin Shedding Occurs after Hemojuvelin Traffics to the Plasma Membrane*

Received for publication, December 26, 2007, and in revised form, April 29, 2008 Published, JBC Papers in Press, April 29, 2008, DOI 10.1074/jbc.M710527200

An-Sheng Zhang[‡1], Fan Yang[§], Kathrin Meyer[‡], Catalina Hernandez[‡], Tara Chapman-Arvedson[¶], Pamela J. Bjorkman[§‖], and Caroline A. Enns[‡]

From the [‡]Department of Cell and Developmental Biology, Oregon Health & Science University, Portland, Oregon 97239, the [§]Division of Biology, California Institute of Technology, Pasadena, California 91125, [¶]Amgen, Thousand Oaks, California 91320, and the [‖]Howard Hughes Medical Institute, California Institute of Technology, Pasadena, California 91125

HFE2 **(hemochromatosis type 2 gene) is highly expressed in skeletal muscle and liver hepatocytes. Its encoded protein, hemojuvelin (HJV), is a co-receptor for the bone morphogenetic proteins 2 and 4 (BMP2 and BMP4) and enhances the BMP-induced hepcidin expression. Hepcidin is a central iron regulatory hormone predominantly secreted from hepatocytes. HJV also binds neogenin, a membrane protein widely expressed in many tissues. Neogenin is required for the processing and release of HJV from cells. The role that neogenin plays in HJV trafficking was investigated, using HepG2 cells, a human hepatoma cell line. Knockdown of endogenous neogenin markedly suppresses HJV release but has no evident effect on HJV trafficking to the plasma membrane. The addition of a soluble neogenin ectodomain to cells markedly inhibits HJV release, indicating that the HJV shedding is not processed before trafficking to the cell surface. At the plasma membrane it undergoes endocytosis in a dynamin-independent but cholesterol-dependent manner. The additional findings that HJV release is coupled to lysosomal degradation of neogenin and that cholesterol depletion by filipin blocks both HJV endocytosis and HJV release suggest that neogenin-mediated HJV release occurs after the HJV-neogenin complex is internalized from the cell surface.**

Iron is an essential nutrient for a variety of biochemical processes. Iron uptake into the body via the intestines is controlled primarily by hepcidin (1). Hepcidin, a central iron-regulatory peptide hormone, is predominantly produced by hepatocytes, circulates in blood, and is excreted in urine (1–5). Hepatic hepcidin expression is regulated by dietary or parenteral iron loading, iron stores, erythropoietic activity, tissue hypoxia, and inflammation (1). Hepcidin deficiency resulting from the primary mutations in human *HFE* (hemochromatosis gene), *TFR2* (transferrin receptor 2 gene), hemochromatosis type 2 gene (*HFE2*), or the hepcidin gene itself (*HAMP*) is the major cause of hereditary hemochromatosis (6). This heterogeneous group of inherited iron overload disorders has a wide range of clinical severity.

HFE2 is a recently cloned gene in humans and encodes a protein termed hemojuvelin (HJV)[2] (7). Its ortholog in mice is called repulsive guidance molecule c (RGMc) because it is the third member of the RGM family to be cloned (7–10). RGMa and RGMb are expressed primarily in the developing and adult central nervous system, which do not overlap with *HFE2* expression (8–10).

The importance of HJV in iron homeostasis has been demonstrated by the observations that the homozygous or compound heterozygous mutations of *HFE2* gene cause the type 2A juvenile hemochromatosis, a particularly severe form of hereditary hemochromatosis (7, 11, 12). Disruption of both *HFE2* alleles ($Hjv^{-/-}$) in mice also causes a severe iron overload (5). The marked suppression of hepatic hepcidin expression detected in juvenile hemochromatosis patients with the *HFE2* mutation as well as in the $Hjv^{-/-}$ mice has implicated HJV as a key upstream regulator of hepatic hepcidin expression (5, 7, 13). In the liver, a recent study using lacZ as a marker indirectly showed a selective expression of HJV in periportal hepatocytes (5). The hepatocyte is, therefore, the principal site in which HJV exerts its regulatory role on hepcidin expression.

Like the other two RGM family members (RGMa and RGMb), HJV is a co-receptor for the bone morphogenetic proteins 2 and 4 (BMP2 and BMP4). HJV enhances hepatic hepcidin expression via the BMP signaling pathway (14). Neither RGMa nor RGMb appears to play a role in the regulation of hepcidin expression. BMPs are cytokines of the transforming growth factor β superfamily that exhibit multiple roles in a wide variety of processes through different signaling pathways (15, 16). BMP signaling is initiated upon ligand binding to BMP receptors, which leads to a sequential phosphorylation of receptor-activated Smads (Smad1, Smad5, and Smad8). The phosphorylated Smad1/5/8 form heteromeric complexes with Smad4. Upon formation, the complex translocates from the cytoplasm to the nucleus to regulate gene expression (17). Recent findings showing that liver-specific disruption of Smad4

* This work was supported, in whole or in part, by National Institutes of Health Grants DK080765 (to A.-S. Z.) and DK54488 (to C. A. E.). This work was also supported by funds from Amgen (to A.-S. Z.). The costs of publication of this article were defrayed in part by the payment of page charges. This article must therefore be hereby marked "*advertisement*" in accordance with 18 U.S.C. Section 1734 solely to indicate this fact.

[1] To whom correspondence should be addressed: Dept. of Cell and Developmental Biology L215, Oregon Health & Science University, 3181 SW Sam Jackson Park Rd., Portland, OR 97239. Tel.: 503-494-5846; Fax: 503-494-4253; E-mail: zhanga@ohsu.edu.

[2] The abbreviations used are: HJV, hemojuvelin; BMP, bone morphogenetic protein; CM, conditioned culture medium; ER, endoplasmic reticulum; GPI, glycosylphosphatidylinositol; PI-PLC, Phosphatidylinositol-specific phospholipase C; RGM, repulsive guidance molecule; Tf, transferrin; TGN, *trans*-Golgi network; MEM, minimum essential medium; siRNA, small interfering RNA; MesNa, sodium 2-mercaptoethanesulfonate; tTA, tetracycline transactivator.

markedly decreases hepcidin expression and causes iron accumulation in mice (18) also support the importance of BMP signaling in iron homeostasis.

The regulation of HJV appears to be primarily at the post-transcriptional level. *HFE2* is expressed highly in both skeletal and heart muscle and at lower levels in liver (7). *HFE2* mRNA levels do not vary with iron loading in the liver of mice or with iron depletion in the skeletal muscle of rats (19, 20). The levels of serum HJV do increase in the early phase of iron deficiency in rats (20). HJV is a GPI-anchored protein (21), and *in vitro* studies demonstrated that HJV undergoes active release (shedding) from the *HFE2*-transfected cells as well as from the differentiated C2 or C2C12 cells (mouse myoblast cell lines), which robustly express endogenous HJV (20, 22, 23). In agreement with the finding in iron-deficient rats, HJV release from the cell lines is inhibited by iron-saturated Tf (holo-Tf) or non-Tf iron salts (20, 22, 24, 25). The observations that no evident defect in muscle development is observed in juvenile hemochromatosis patients and $Hjv^{-/-}$ mice rule out the possibility that HJV has a primary role in muscle development (7, 11, 12). However, skeletal muscle, accounting for ~35–40% of body weight, has the highest expression of *HFE2* mRNA (7) and is also a significant iron consumer for myoglobin synthesis with serum Tf presumably as its source of iron. The findings that soluble HJV plays a critical role in the negative regulation of hepatic hepcidin expression through BMP signaling in hepatocytes support the idea that skeletal muscle may serve as a body iron sensor as well as the major source of serum HJV to indirectly modulate hepatic hepcidin expression by regulating the HJV release into the circulation (20, 22, 26, 27).

HJV also binds neogenin, a receptor for RGMa and netrins (28, 29). Neogenin is a membrane protein and widely expressed in most tissues, including liver and skeletal muscle (30–34). The interactions of neogenin with RGMa and netrins are essential for neural development (35, 36). Our previous study showed that the interaction with neogenin is required for HJV release from muscle cells (20). The G320V mutation in HJV accounts for approximately two-thirds of cases of type 2A juvenile hemochromatosis. This mutation disrupts the interaction of HJV with neogenin, blocks HJV release, and results in the decreased HJV targeting to the cell surface and the retention of HJV in the endoplasmic reticulum (ER) (7, 20, 21, 37). These findings imply that neogenin may play a critical role in HJV intracellular trafficking. How neogenin is involved in this process remains to be elucidated.

In this study, we investigated the role of neogenin in HJV trafficking in HepG2 cells. We found that knockdown of endogenous neogenin markedly suppresses HJV release but has no evident effect on HJV trafficking to the plasma membrane. Release of HJV requires not only neogenin but also endocytosis presumably by a cholesterol-sensitive and dynamin-independent pathway.

EXPERIMENTAL PROCEDURES

Cell Culture and Transfection—HepG2 cells were purchased from ATCC and maintained in MEM, 10% fetal calf serum, 1 mM pyruvate, 1× nonessential amino acids (complete medium). HepG2 cells stably expressing G320V (G320V-HepG2) were generated using Nucleofector kit V (Amaxa Biosystems) as previously described (20). The G320V mutant *HFE2* cDNA was prepared as previously reported (21). HepG2 cells stably transfected with wild type *HFE2* (HJV-HepG2) or pcDNA3 empty vector (control-HepG2) were generated previously (20). The stably transfected cells were maintained in complete medium with 800 μg/ml G418.

Knockdown of Endogenous Neogenin—Neogenin siRNA (Dharmacon) was used to knock down the endogenous neogenin in control and HJV-HepG2 cells as previously described (20). RNAiMAX reagent (Invitrogen) was used for the transfection. The negative control siRNA was the same as previously described (20). The cells were transfected with the siRNA twice on days 1 and 3 to maximize the efficacy of the knockdown. HJV in cell lysates and the conditioned medium (CM) and neogenin in cell lysates were analyzed by Western blot.

Flow Cytometry Analysis—Flow cytometry analysis was used to quantify the cell surface HJV in HJV-HepG2 cells with or without neogenin knockdown. Briefly, the cells were first detached from flasks with the cell dissociation buffer (Invitrogen). The cells were then incubated with affinity-purified rabbit anti-HJV antibody (4 μg/ml) in Hanks' buffer supplemented with 3% fetal bovine serum for 30 min at 4 °C, followed by incubation with phycoerythrin-conjugated goat anti-rabbit IgG (1:500 dilution; Caltag, Burlingame, CA) in the same buffer for 30 min at 4 °C. Flow cytometry analysis was performed on a Becton Dickinson FACSCalibur flow cytometer at the Core Facility of Oregon Health & Science University. Rabbit IgG and control-HepG2 cells were used as negative controls. The levels of cell surface HJV are expressed as arbitrary units. We used the standard deviation and the paired and two-tailed Student's *t* test to evaluate the statistical significance of the cell surface HJV in HepG2 cells with or without neogenin knockdown.

Phosphatidylinositol-specific Phospholipase C (PI-PLC) Cleavage of Cell Surface HJV—Approximately 10^6 HJV-HepG2 cells in 6-well plate were incubated in 0.5 ml of plain MEM in presence or absence of PI-PLC (Molecular Probes) at the concentration of 1 unit/ml at 37 °C in 5% CO_2 incubator or at 4 °C for the time intervals indicated in the text. The supernatants were collected, and the cell lysates were prepared using NET-Triton buffer (150 mM NaCl, 5 mM EDTA, and 10 mM Tris (pH 7.4) with 1% Triton X-100) with 1× protease inhibitor mixture (Roche Applied Science). Approximately one-third of the cell lysates or supernatants was subjected to 11% SDS-PAGE, followed by immunodetection of HJV and neogenin as described under "Immunodetection."

HJV Release—The effects of the ectodomain (extracellular domain) of neogenin, bafilomycin A (an inhibitor of the vacuolar H^+-ATPase; Sigma), dynasore (a cell-permeable inhibitor of dynamin; Sigma), and filipin (a cholesterol-binding agent; Sigma) on HJV release from HJV-HepG2 cells were examined. The ectodomain of neogenin was generated by subcloning the neogenin cDNA encoding the hydrophobic signal sequence (residues 1–33) and the ectodomain (residues 34–1103) with a C-terminal His_6 tag into the pVL1393 baculovirus transfer vector (BD Biosciences). The recombinant protein was purified from the supernatant of baculovirus-infected High 5 cells using nickel-nitrilotriacetic acid and gel filtration chromatography. HJV-HepG2 cells were cultured in the 12-well plates. After 48 h

of incubation with 60% confluence, fresh MEM, 5% fetal calf serum was changed with the addition of neogenin ectodomain at 0, 250, 500, 750, and 1,000 nM and incubated for 24 h. HJV in ~50% of cell lysate and 20% of the CM was analyzed by Western blot. For the inhibitors, the experiments were conducted when HJV-HepG2 cells were ~80% confluence. The cells were incubated in the absence or presence of bafilomycin A (100 nM), dynasore (80 and 160 μM), or filipin (1, 5, and 10 μg/ml) for the indicated time intervals where no evident cytotoxicity was detected. The whole cell lysate and 50% of CM were analyzed.

Expression of Wild Type and Mutant Dynamin—To block dynamin-mediated endocytosis, adenoviruses were used to infect cells to introduce wild type or K44A mutant dynamin-1 (dynamin) into HJV-HepG2 cells. The viruses were kindly provided by Dr. Sandra Schmid at the Scripps Research Institute (La Jolla, CA). The viral infections were conducted as described previously with some modifications (38). Briefly, HJV-HepG2 cells were subcultured into 12-well plates ~24 h before the infection. The cells were overlaid with 250 μl of binding medium (Hanks' salts containing 1 mM $MgCl_2$, 1 mM $CaCl_2$, and 10 mM Hepes, pH 7.2) containing the mixture of tTA activator virus and wild type or K44A-dynamin-1 virus at equal ratios. To generate the cells with various levels of dynamin, different amounts of virus were added as indicated in the text. After 2 h of incubation at 37 °C to enable viral attachment and infection, binding medium was changed to complete medium. After 18 h of incubation to allow the expression of introduced dynamin, the medium was replaced with 600 μl of fresh complete medium. The cultured conditioned medium was collected to assay HJV release after an additional 24 h of incubation. The levels of dynamin in cell lysate were analyzed as described under "Immunodetection." In this study, cells infected with tTA activator virus alone were served as negative controls.

HJV Internalization—The internalization of biotinylated cell surface HJV was conducted as previously described (39–41). Briefly, HJV or control HepG2 cells in 6-well plate at ~80% confluence were biotinylated with 0.25 mg/ml Sulfo-NHS-Biotin (Pierce) at 4 °C for 20 min. The cells were then incubated at 37 °C for the time intervals indicated in the text. Biotin remaining on cell surface was stripped using MesNa (Sigma) at 4 °C. Alternatively, the cells were incubated in presence of PI-PLC (1 unit/ml) at 4 °C for 3 h to release the cell surface GPI-anchored proteins. The cells were then solubilized in NET-Triton/1× protease inhibitors mixture, followed by using streptavidin-agarose beads (Pierce) to isolate the biotinylated HJV (internalized fraction). The total cell surface HJV was isolated with strepavidin-agarose from biotinylated cells labeled at 4 °C.

^{125}I-Tf Uptake—^{125}I-Tf uptake was used to detect the effect of dynasore and filipin on *TfR1*-mediated Tf uptake. The rate of ^{125}I-Tf uptake was determined as described previously (42) with the following modifications. HepG2 cells in 6-well plates were first preincubated in 1 ml of uptake medium (MEM, 2 mg/ml ovalbumin, 20 mM Hepes, pH 7.2) with dynasore (80 and 160 μM) or filipin (10 μg/ml) for 30 min at 37 °C. ^{125}Tf uptake was then initiated by changing to the uptake medium containing 50 nM ^{125}Tf as well as the same concentrations of dynasore or filipin. The inclusion of 1 mg/ml unlabeled Tf was used as the control for nonspecific uptake. After an 8-min incubation at 37 °C, externally bound Tf was stripped by acid wash. The radioactivity remaining within cells was counted. The amount of specific uptake in the presence of inhibitors was expressed as the percentage of corresponding controls. The standard deviation and the paired and two-tailed Student's *t* test were used to evaluate the statistical significance between the groups with and without inhibitors.

Immunodetection—Cell lysate protein and CM were subjected to SDS-PAGE under reducing conditions, followed by transfer onto nitrocellulose membrane. The membranes were probed with affinity-purified rabbit anti-HJV antibody (0.22 μg/ml), rabbit anti-neogenin antibody (0.4 μg/ml; Santa Cruz Biotechnology), mouse anti-dynamin (1:4000; Upstate), or mouse anti-β-actin antibody (1:10,000; Chemicon International), followed by immunodetection using corresponding horseradish peroxidase-conjugated secondary antibody (Chemicon International, Temecula, CA). The bands were exposed to x-ray film by chemiluminescence (Super Signal; Pierce).

RESULTS

Knockdown of Endogenous Neogenin Has No Effect on HJV Trafficking to the Plasma Membrane but Blocks HJV Release—Our previous studies demonstrate that HJV interacts with neogenin in HEK293 cells and that interaction with neogenin is required for HJV release in C2C12 cells, a mouse myoblast cell line (20, 21). Recent studies indicate that the G320V mutant form of HJV that does not bind neogenin remains predominantly in the ER and does not traffic efficiently to the plasma membrane (21, 37). These observations suggest a critical role of neogenin in HJV trafficking. To gain insight into the function of neogenin in this process, we first examined its role in HJV trafficking to the plasma membrane in HepG2 cells. HepG2 cells are of a relatively well differentiated human hepatoma cell line that expresses many hepatocyte-specific genes including Tf, hepcidin, *TfR2*, and ceruloplasmin (data not shown). The endogenously expressed neogenin is readily detectable by Western blot (Fig. 1*A*). We used siRNA to knock down the neogenin in HepG2 cells stably transfected with HJV (HJV-HepG2) and then quantified the levels of cell surface HJV by flow cytometry analysis. In comparison with the control siRNA, siRNA specific to human neogenin was able to eliminate detectable neogenin (Fig. 1*A*). Flow cytometry analysis revealed a mild but not statistically significant increase ($p = 0.36$) (Fig. 1*C*). Similar results were obtained by immunofluorescent analysis of nonpermeabilized cells (data not shown). To confirm the lack of change in cell surface HJV with the knockdown of neogenin, we examined the amount of HJV released by PI-PLC, which cleaves the phosphodiester bond of GPI-linked proteins. Similar quantities of HJV were released upon PI-PLC cleavage whether or not neogenin was present in the cells (Fig. 1*A*). Consistent with the previous reports showing complex processing of HJV (21, 23), three distinct HJV bands migrating at approximately 50, 33, and 15 kDa were detected in the supernatants of PI-PLC digestion (Fig. 1*A*, *bottom panel*). Down-regulation of neogenin does not alter this profile. Taken together, these results indicate that neogenin is not required for HJV trafficking to the plasma membrane.

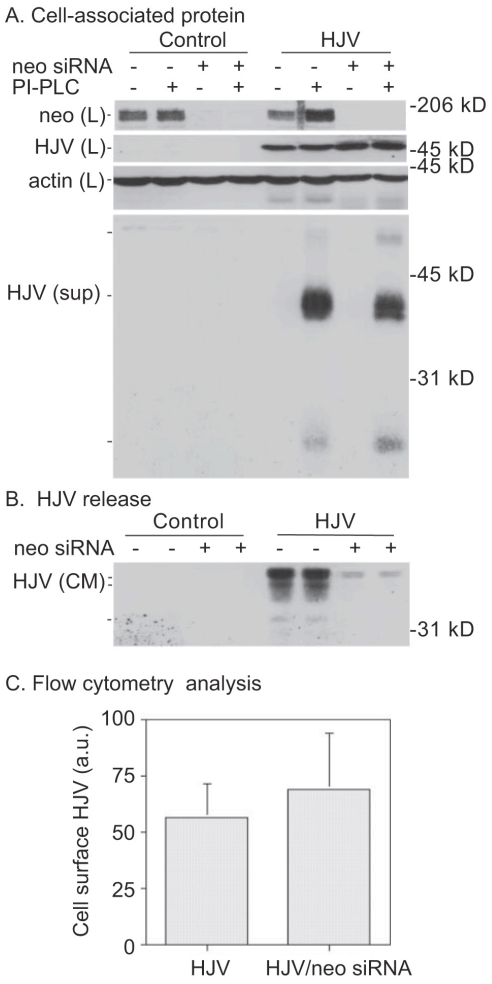

FIGURE 1. **Knockdown of neogenin blocks HJV release but does not affect HJV cell surface expression.** We used siRNA specific to human neogenin and Lipofectamine RNAiMax to knockdown the endogenous neogenin in control and HJV-HepG2 cells as described under "Experimental Procedures." Scrambled siRNA was used as a parallel negative control. *A*, cell-associated protein. PI-PLC digestion was used to examine the effect of neogenin knockdown on the dynamic HJV expression on cell surface. The cells from above were incubated in the presence or absence of PI-PLC at the concentration of 1 unit/ml for 2 h in 37 °C CO_2 incubator. HJV, neogenin (*neo*), and actin in cell lysates (*L*) and the HJV in supernatant (*HJV (sup)*) were detected by Western blot analysis. *B*, HJV release. At 24 h after the second transfection of cells with siRNA, the cells were pooled and subcultured into 12-well plates with complete medium containing 10% fetal calf serum. Approximately 48 h later, 100 μl of the CM was subjected to SDS-PAGE and Western blot analysis for HJV (*HJV (CM)*). *C*, flow cytometry analysis of the cell surface HJV. Flow cytometry analysis of cell surface HJV was analyzed as described under "Experimental Procedures" and expressed as arbitrary units (*a.u.*). The averages of four individual analyses and the standard deviations were presented. All of the other experiments were repeated at least three times with consistent results.

Because neogenin did not affect the biosynthetic pathway of HJV, the effect of neogenin on the shedding of HJV was examined. Detection of HJV in the CM by Western blot analysis

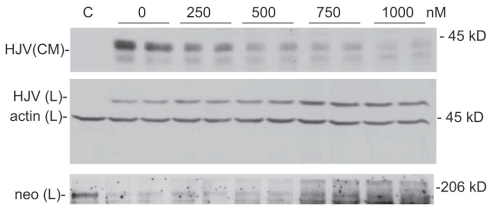

FIGURE 2. **The ectodomain of neogenin blocks HJV release.** *HFE2* stably transfected (HJV) and empty vector transfected control (*C*)-HepG2 cells in 12-well plate were incubated in the absence or presence of the soluble ectodomain of neogenin at 0–1000 nM for 24 h. Approximate half of the cell lysate (*L*) and 20% of the CM was subjected to Western blot analysis for HJV and neogenin (*neo*). Actin was also probed in the lysate as a protein loading control. The experiments were repeated three times with consistent results.

revealed a marked decrease of released HJV when neogenin was depleted (Fig. 1*B*). The multiple HJV bands migrating at ~37 kDa in the conditioned medium are in agreement with the previous observations (20, 23), implying the existence of multiple cleavage sites (Fig. 1*B*). These results suggest that both myocytes and hepatocytes share similar pathways of neogenin-mediated HJV release. Importantly, these results also imply that neogenin influences the shedding of HJV after it traffics to the cell surface.

Soluble Neogenin Inhibits HJV Release—Neogenin is a type I transmembrane protein consisting of an extracellular ectodomain, a transmembrane domain, and a cytoplasmic domain (33). The binding of neogenin to HJV has been mapped to the ectodomain of neogenin with a binding affinity of ~500 nM (43). We used purified ectodomain of neogenin to competitively disrupt the HJV-neogenin interaction at the cell surface and then examined the effect of this disruption on HJV release. In this study, we directly added ectodomain of neogenin to the culture medium of HJV-HepG2 cells. After 24 h of incubation, HJV in the cultured conditioned medium was analyzed by Western blot. In comparison with the parallel controls showing active HJV release, the dose response to neogenin ectodomain indicates that inhibition of HJV release was achieved over a similar concentration range as the binding affinity (Fig. 2, *top panel*). A similar inhibition of HJV release was observed when neogenin expression was knocked down using neogenin siRNA (Fig. 1*B*). Endogenous neogenin levels increase slightly upon treatment with the ectodomain fragment (Fig. 2, *bottom panel*), indicating that the binding of soluble neogenin to HJV could inhibit the down-regulation of endogenous neogenin by HJV. Together with the neogenin knockdown studies, these results indicate that the neogenin fragment competes with the endogenous neogenin for binding to HJV. The interaction of HJV with full-length neogenin is essential for both the processing and release of HJV as well as for the down-regulation of neogenin after HJV reaches the cell surface.

HJV Release Is Correlated with Neogenin Degradation—We observed that expression of HJV in HepG2 cells resulted in lower levels of endogenous neogenin (20). To further evaluate the role of HJV in the down-regulation of neogenin, we first compared the effect of wild type and G320V HJV expression on the level of neogenin. The G320V mutant, which does not bind neogenin, was used as a negative control. Wild type HJV, but

not the G320V mutant, markedly decreased neogenin protein levels and undergoes active release (Fig. 3*A*). A similar effect obtained in at least three individual stably transfected clones for each construct ruled out a clonal effect (data not shown). Alternatively, we used PI-PLC, which can release cell surface HJV into the medium, to determine the effect of HJV on neogenin levels. PI-PLC was directly added into the culture medium of HepG2 cells expressing HJV or G320V HJV at 37 °C, and the cells were incubated for 3 h. Under these conditions, PI-PLC is expected to release HJV. If the full-length HJV-neogenin complex is required for internalization and neogenin degradation, treatment of HJV-HepG2 cells with PI-PLC should release HJV from cell and elevate the cellular neogenin level. Consistent with this hypothesis, PI-PLC released HJV and resulted in a marked increase of neogenin after a 3-h incubation, as compared with the corresponding controls with no PI-PLC (Fig. 3*B*). Importantly, an increase of neogenin was not detected in the empty vector-transfected control or in G320V HepG2 cells where the G320 HJV mutant is located mainly in the ER (Fig. 3*B*) or in HJV-HepG2 cells at 4 °C (data not shown). These results suggest that HJV and neogenin internalize prior to neogenin degradation.

The increased neogenin degradation could result from the following two possibilities, the release of HJV/neogenin as a complex and/or the sorting to and degradation of neogenin in lysosomes. No shed neogenin could be detected in the concentrated conditioned medium from HJV-HepG2 cells by Western blot analysis under conditions where cellular neogenin decreased (data not shown). To determine whether neogenin is degraded in lysosomes, we treated HJV-HepG2 cells with bafilomycin A, an inhibitor of the vacuolar H^+-ATPase (44), which dissipates the pH gradient in the intracellular organelles and thereby blocks protein degradation in lysosomes. After a 4-h incubation with 100 nM bafilomycin A, a significant increase of cellular neogenin in HJV-HepG2 cells was apparent (Fig. 3*C*). Interestingly, HJV release does not seem to be altered. These results suggest that lysosome is the site of neogenin degradation and that HJV shedding does not depend on low pH. In addition, the mild increase of cellular HJV in presence of bafilomycin A (Fig. 3*C*) also implies that HJV release might not be the sole pathway for cellular HJV turnover. Rather, a certain portion of HJV may also be degraded in lysosomes. Taken together, the above observations imply that the interaction of neogenin with HJV triggers its internalization from plasma membrane for either cleavage or lysosomal degradation.

HJV Release Is Inhibited by Cholesterol Depletion but Not by Dynamin Inhibitors—Plasma membrane proteins can be internalized by at least four known pathways, three of which require dynamin for fission of the invaginated vesicles from the plasma membrane (45). To determine whether HJV release from cells was dependent on its endocytosis, we examined whether the disruption of dynamin function affects HJV release from HJV-HepG2 cells. Initially, dynasore, a cell-permeable inhibitor specific for the dynamin GTPase (46), was used to inhibit endocytosis. Unexpectedly, no evident effect was detected when cells were incubated in the presence of dynasore at the recommended concentrations (80 and 160 μM) (Fig. 4*A*). To test whether these cells were sensitive to dynasore, the effect of

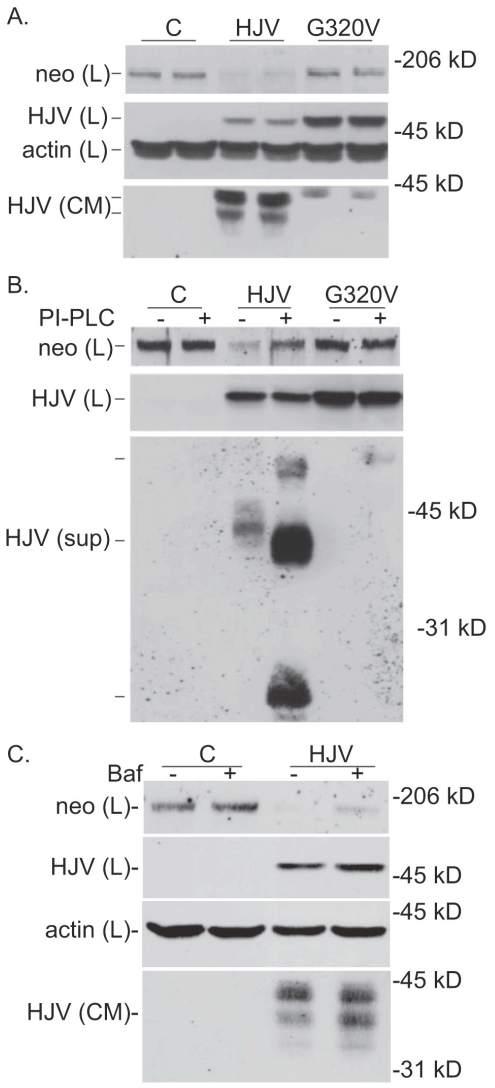

FIGURE 3. **HJV release is correlated with neogenin degradation.** *A*, expression of HJV, but not G320V mutant, decreases the level of neogenin protein in HepG2 cells. Cell lysate from 2×10^5 cells and CM from 0.8×10^5 cells of overnight culture were subjected to SDS-PAGE, followed by immunodetection of the HJV in both cell lysates (*HJV (L)*) and CM (*HJV (CM)*), and neogenin (*neo (L)*) and actin in the lysate. *B*, PI-PLC digestions. HJV, G320V, and control-HepG2 cells in 12-well plates at approximate 70% confluence were incubated in 300 μl of MEM with or without the addition of PI-PLC (1 unit/ml) for 3 h at 37 °C CO_2 incubator. Approximately half of the cell lysate or supernatant were subjected to SDS-PAGE, followed by immunodetection of HJV in both cell lysate (*L*) and supernatant (*sup*), and neogenin (*neo*) and actin in the lysate. *C*, bafilomycin A increases cellular neogenin. Control (*C*) and HJV-HepG2 cells in 12-well plate were incubated for 4 h in complete medium with or without the addition of 100 nM bafilomycin A (*Baf*). Neogenin, HJV, and actin in cell lysate (*L*) and HJV in approximately one-third of CM were detected by Western blot using the specific antibodies. All of the experiments were repeated at least three times with consistent results.

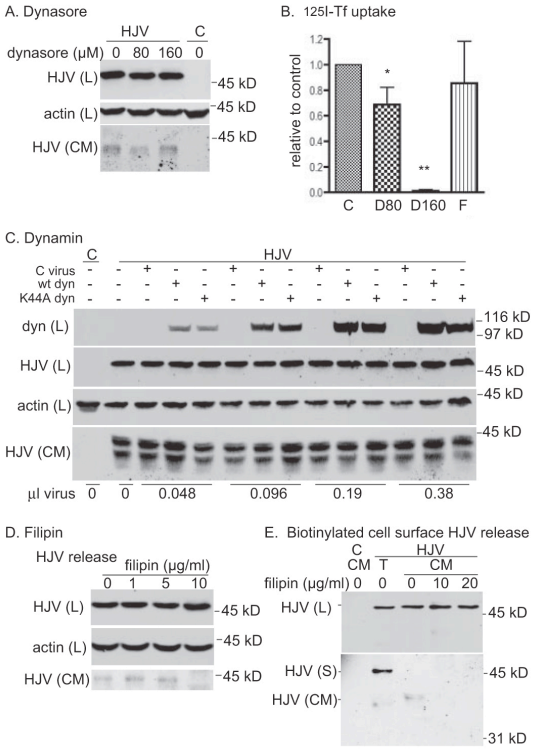

FIGURE 4. **Depletion of cholesterol inhibits HJV release.** *A*, dynasore does not inhibit HJV release. HJV-HepG2 cells in 12-well plates were incubated in the presence of 0, 80, and 160 μM of dynasore for 2 h at 37 °C. HJV in both cell lysate (*L*) and 50% of CM was detected by Western blot. *B*, ^{125}I-Tf-uptake. HepG2 cells in 6-well plates with approximate 80% confluence were first pre-incubated in absence or presence of dynasore (80 and 160 μM; *D80* and *D160*, respectively) and filipin (10 μg/ml) (*F*) for 30 min at 37 °C. ^{125}I-Tf uptake was initiated by incubating the cells in the presence of 50 nM ^{125}I-Tf and the same concentrations of inhibitors. After 8 min of incubation at 37 °C, membrane-bound ^{125}I-Tf was removed by acid wash. The ^{125}I radioactivity was counted. The inclusion of 1 mg/ml unlabeled cold Tf was used as the nonspecific uptake control. The rates of specific uptake in the presence of inhibitors were expressed as the percentage of the corresponding controls. The results are from four individual experiments. *, $p = 0.0281$; **, $p < 0.0001$. *C*, wild type and K44A mutant dynamin. HJV-HepG2 cells in 12-well plates were infected with the mixture of tTA activator virus and different amounts of adenovirus containing either wild type or K44A mutant dynamin (0, 0.048, 0.096, 0.19, and 0.38 μl of stock virus/well). tTA activator virus alone was used as a negative control. The cells were first incubated for ~18 h to allow the expression of introduced dynamin. Afterward, ~20% of the CM collected from the incubation between 18 and 42 h post-infection was detected for HJV by Western blot. In addition, dynamin (*dyn*), HJV, and actin in the cell lysate (*L*) at 42 h post-infection were also analyzed. *D*, filipin inhibits HJV release. HJV-HepG2 cells in 12-well plates were incubated in the presence of 0, 1, 5, and 10 μg/ml of filipin for 2 h at 37 °C. HJV in both cell lysate (*L*) and 50% of CM was detected by Western blot. *E*, filipin inhibits the biotinylated cell surface HJV release. Cell surface proteins in HJV-HepG2 cells were biotinylated at 4 °C, followed by incubation in the presence of 0, 10, and 20 μg/ml of filipin at 37 °C for 2 h. The biotinylated HJV that was released into the medium (*HJV (CM)*), as well as the total biotinylated cell surface HJV (T) (*HJV (S)*), was isolated using streptavidin-agarose beads and subjected to Western blot (lower panel). The total HJV in cell lysate (*L*) was also detected (*upper panel*). All of the experiments were repeated at least three times with consistent results. In each experiment, the lysate and CM from control-HepG2 cells (*C*) were included as a negative control for HJV.

dynasore on ^{125}I-Tf uptake was measured because transferrin receptor-mediated Tf uptake is a dynamin-dependent process. Consistent with the previous observations (46), dynasore significantly inhibited and completely blocks ^{125}Tf internalization at 80 and 160 μM, respectively (Fig. 4*B*). These results suggest that HJV release is independent of dynamin.

To further substantiate this observation, we next examined the effects of the K44A mutant dynamin. The K44A mutation disrupts the dynamin GTPase activity. It is widely used as a dominant-negative to block the dynamin-dependent endocytosis (38). HJV-HepG2 cells were infected with four different concentrations of adenovirus encoding either wild type or K44A mutant dynamin. Consistent with the dynasore results, no evident inhibition of HJV release was detected when cells were infected with the virus encoding the K44A dynamin mutant (Fig. 4*C*). These results again support that dynamin-dependent endocytosis is not involved in HJV release.

HJV is a GPI-anchored protein (21). Depletion of cholesterol by filipin, a sterol-binding agent that binds to cholesterol, disrupts both the endocytosis and exocytosis of GPI-anchored proteins (45, 47–49). Therefore, we examined the effect of filipin on HJV release from HJV-HepG2 cells. Filipin was added directly to the culture medium at the concentrations ranging from 0 to 10 μg/ml. The cells were incubated for 2 h at 37 °C. A marked decrease of HJV in the conditioned medium was evident in the presence of 10 μg/ml of filipin (Fig. 4*D*). Longer periods of incubation were not pursued because of the cytotoxicity of filipin. Alternatively, the effects of filipin on the release of biotinylated HJV were measured. Consistent with the above finding, filipin was also found to markedly suppress the release of HJV, which was derived from the cell surface (Fig. 4*E*). Further analysis revealed that filipin does not significantly alter the ^{125}Tf internalization compared with the control ($p = 0.4997$) (Fig. 4*B*). The relatively large variability in Tf uptake may result from the effect of cholesterol depletion on clathrin-coated pit internalization. Previous studies showed that the acute cholesterol depletion markedly reduces the rate of internalization of *TfR1* by more than 85% (50). These results suggest that HJV release depends on cholesterol and possibly on cholesterol-dependent HJV endocytosis.

Endocytosis of Hemojuvelin—To elucidate whether cell surface HJV undergoes endocytosis, cell surface proteins were labeled at 4 °C with a cleavable form of biotin. Less than 10% of the total HJV was biotinylated, suggesting that the majority of HJV is localized intracellularly (Fig. 5*A*). To detect internalized HJV, the cells were warmed to 37 °C for 10 min. Any biotin remaining on cell surface was stripped by the nonpermeable reducing agent, MesNa. The internalized HJV was then isolated using streptavidin-agarose beads. Controls showed that MesNa could strip most of the biotin coupled to HJV in HJV-HepG2 cells left at 4 °C (Fig. 5*A*). Internalization was a rapid process. The internalized HJV was detectable by Western blot after 5 min of incubation and reaches a plateau after 10 min of incubation (Fig. 5*A* and data not shown). Similar results were also obtained by using PI-PLC to strip the cell surface HJV (data not shown). These findings indicate that HJV undergoes endocytosis in HepG2 cells.

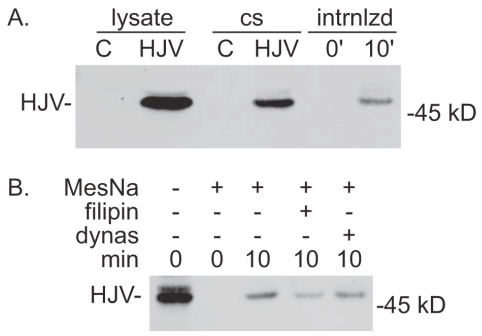

FIGURE 5. **HJV undergoes endocytosis.** *A*, internalization of biotinylated cell surface HJV. Cell surface proteins in control (*C*) and HJV-HepG2 cells were biotinylated at 4 °C, followed by incubation at 37 °C for 0 and 10 min (*0′* and *10′*). After stripping the biotin remaining on cell surface, the internalized HJV (*intrnlzd*) was isolated using streptavidin-agarose beads and subjected to Western blot. Approximately 10% of lysate from the cells without biotinylation (lysate) and the total biotinylated cell surface HJV without incubation and stripping (*cs*) were included for the analysis. *B*, filipin inhibits HJV internalization. The experiments were conducted essentially the same as described in *A*, except that the biotinylated cells were first preincubated in the absence or presence of 10 μg/ml filipin or 160 μM dynasore (*dynas*) at 4 °C for 30 min before the incubation at 37 °C.

HJV Endocytosis Is via Dynamin-independent but Possibly Cholesterol-dependent Pathway—To further characterize the pathway of HJV endocytosis, we examined the effect of filipin and dynasore on the internalization of biotinylated cell surface HJV in HJV-HepG2 cells. HJV internalization was markedly inhibited when cells were incubated in the presence of 10 μg/ml filipin (Fig. 5*B*). However, no evident inhibition was detected when cells were incubated in the presence of dynasore at concentrations of 80 and 160 μM (Fig. 5*B*; data not shown). These results suggest that HJV endocytosis is via the dynamin-independent and cholesterol-dependent pathway, although the definitive role of cholesterol in this process still remains to be further characterized by other strategies.

DISCUSSION

The role of neogenin in HJV trafficking in HepG2 cells was investigated. Our results show that knockdown of endogenous neogenin markedly suppresses HJV release but has no evident effect on HJV trafficking to the plasma membrane. The marked inhibition of HJV release by soluble neogenin suggests that the neogenin-regulated HJV release occurs after HJV traffics to the plasma membrane. Furthermore, our data also indicate that HJV shedding occurs after HJV is internalized.

HJV is a GPI-anchored protein (21) and, like other GPI-linked proteins, is co-translationally translocated into the ER where they are linked to a GPI anchor before trafficking to the cell surface (51). In this study, we excluded the possibility that HJV release occurs in its biosynthetic pathway. The observation that neogenin knockdown does not alter the HJV trafficking to the cell surface but does block the HJV release supports this assumption. In addition, these findings also have an important implication with respect to the possible defects of G320V mutation in HJV. The G320V mutation is the most frequently detected mutation in type 2A juvenile hemochromatosis, accounting for approximately two-thirds of cases (7). G320V mutation abolishes the HJV-induced hepcidin expression (14). Early studies demonstrated that it disrupts the interaction of HJV with neogenin and that G320V mutant HJV has a decreased targeting onto cell surface, is slightly shed, and is largely retained in the ER (7, 20, 21, 23, 37).[3] Because neogenin is not required for HJV trafficking to the plasma membrane, the primary defect of the G320V mutation appears to be misfolding, which consequently blocks its exit from the ER, the subsequent trafficking to the plasma membrane, as well as lack of the interaction with neogenin.

HJV release takes place after it traffics to the plasma membrane and binds neogenin. The finding that HJV can efficiently traffic to the plasma membrane in the absence of neogenin but does not undergo release rules out the possibility that neogenin acts as a chaperone to traffic HJV to the cell surface. Rather, the association with neogenin is a prerequisite for shedding, because soluble neogenin ectodomain can competitively inhibit HJV release, similar to neogenin knockdown. The finding that the addition of soluble neogenin ectodomain does not result in the depletion of endogenously expressed neogenin in cells but rather a slight increase in endogenous neogenin suggests that the inhibition of HJV release is caused by competitively disrupting the interaction of HJV with endogenous neogenin. These observations therefore implicate a critical role of neogenin transmembrane and cytoplasmic domains in the process of HJV release.

Recent studies indicate that the HJV cleavage is mediated by the proprotein convertase furin (24, 25). Furin is predominantly localized in the TGN and cycles between the TGN and the plasma membrane (52). Like transmembrane proteins, furin is synthesized in the ER, and like other pro-enzymes, it is activated until it reaches its destination, which is the TGN in the case of furin (52). This specific localization of furin and its trafficking between the plasma membrane and the TGN and our data, therefore, do not favor the findings in a recent report stating that the furin-mediated HJV shedding occurs in the ER (25). On the basis of our results, the endocytic compartments are most likely the sites of HJV shedding. First, HJV release is coupled to the increased neogenin degradation in lysosome. Second, HJV undergoes endocytosis, and blockage of HJV internalization inhibits HJV release.

Previous studies indicate that the endocytosis of many GPI-anchored proteins is through dynamin-independent but cholesterol-dependent pathway, because GPI-anchored proteins are present at the surface in cholesterol-dependent nanoscale clusters (45, 47–49). Our results showing that cholesterol inhibitor, but not dynamin inhibitor, is able to decrease HJV internalization tend to support that the endocytosis of HJV follows this pathway. These observations also imply that HJV endocytosis may depend on its GPI anchor. However, this does not exclude other possibilities because neogenin seems to play the critical role in this process. Neogenin has a cytoplasmic domain of 388 amino acids (33). The role of neogenin cytoplasmic domain in this process remains to be determined.

[3] A.-S. Zhang and C. A. Enns, unpublished observations.

On the basis of our data, we propose a model for the neogenin-required and furin-mediated HJV shedding. The association of HJV with neogenin on plasma membrane triggers the internalization of both proteins as a complex. The complex is then retrieved into a compartment, in which HJV is exposed to furin for cleavage and the subsequent release, whereas neogenin is sorted for degradation in lysosome. The fraction of HJV that is unable to associate with neogenin would be targeted for degradation.

Soluble HJV plays a critical role in the inhibition of hepatic hepcidin expression through the BMP signaling (22, 24, 26, 27). Studies in transfected cells indicate that holo-Tf and/or non-Tf iron inhibits the shedding of HJV (20, 22, 37). Animal studies suggest that serum HJV could be derived from both skeletal muscle and liver hepatocytes (20). These observations, therefore, support that serum HJV plays a critical role in the regulation of iron homeostasis. The findings in the present study showing that soluble neogenin competitively blocks HJV release and HJV release requires HJV endocytosis imply that the regulation of HJV release by holo-Tf might take place at the cell surface, after internalization or during the retrograde transport. Thus holo-Tf would disrupt HJV-neogenin complex similar to soluble neogenin and thereby modulate HJV release. However, the mechanism by which holo-Tf interferes with HJV release still remains to be elucidated.

In summary, this study demonstrates that neogenin is not required for HJV trafficking from the ER to the plasma membrane, but the HJV-neogenin interaction at the cell surface is essential for HJV release. Together with the specific localization of furin, the findings that HJV endocytosis is required for its release suggest that neogenin-dependent retrograde trafficking of HJV to furin positive compartments is necessary for HJV shedding. How this process is regulated by iron still remains to be explored and will be the subject of future research.

Acknowledgments—We thank Julia Maxson, Maja Chloupkova, Juxing Chen, and Junwei Gao in Caroline Enns' laboratory for critical reading of the manuscript and valuable comments.

REFERENCES

1. Nemeth, E., and Ganz, T. (2006) *Annu. Rev. Nutr.* **26,** 323–342
2. Park, C. H., Valore, E. V., Waring, A. J., and Ganz, T. (2001) *J. Biol. Chem.* **276,** 7806–7810
3. Pigeon, C., Ilyin, G., Courselaud, B., Leroyer, P., Turlin, B., Brissot, P., and Loreal, O. (2001) *J. Biol. Chem.* **276,** 7811–7819
4. Zhang, A. S., Xiong, S., Tsukamoto, H., and Enns, C. A. (2004) *Blood* **103,** 1509–1514
5. Niederkofler, V., Salie, R., and Arber, S. (2005) *J. Clin. Investig.* **115,** 2180–2186
6. Hentze, M. W., Muckenthaler, M. U., and Andrews, N. C. (2004) *Cell* **117,** 285–297
7. Papanikolaou, G., Samuels, M. E., Ludwig, E. H., MacDonald, M. L., Franchini, P. L., Dube, M. P., Andres, L., MacFarlane, J., Sakellaropoulos, N., Politou, M., Nemeth, E., Thompson, J., Risler, J. K., Zaborowska, C., Babakaiff, R., Radomski, C. C., Pape, T. D., Davidas, O., Christakis, J., Brissot, P., Lockitch, G., Ganz, T., Hayden, M. R., and Goldberg, Y. P. (2004) *Nat. Genet.* **36,** 77–82
8. Schmidtmer, J., and Engelkamp, D. (2004) *Gene Expr. Patterns* **4,** 105–110
9. Oldekamp, J., Kramer, N., Alvarez-Bolado, G., and Skutella, T. (2004) *Gene Expr. Patterns* **4,** 283–288
10. Niederkofler, V., Salie, R., Sigrist, M., and Arber, S. (2004) *J. Neurosci.* **24,** 808–818
11. De Gobbi, M., Roetto, A., Piperno, A., Mariani, R., Alberti, F., Papanikolaou, G., Politou, M., Lockitch, G., Girelli, D., Fargion, S., Cox, T. M., Gasparini, P., Cazzola, M., and Camaschella, C. (2002) *Br. J. Haematol.* **117,** 973–979
12. Camaschella, C., Roetto, A., and De Gobbi, M. (2002) *Semin. Hematol.* **39,** 242–248
13. Huang, F. W., Pinkus, J. L., Pinkus, G. S., Fleming, M. D., and Andrews, N. C. (2005) *J. Clin. Investig.* **115,** 2187–2191
14. Babitt, J. L., Huang, F. W., Wrighting, D. M., Xia, Y., Sidis, Y., Samad, T. A., Campagna, J. A., Chung, R. T., Schneyer, A. L., Woolf, C. J., Andrews, N. C., and Lin, H. Y. (2006) *Nat. Genet.* **38,** 531–539
15. ten Dijke, P., and Hill, C. S. (2004) *Trends Biochem. Sci.* **29,** 265–273
16. Feng, X. H., and Derynck, R. (2005) *Annu. Rev. Cell Dev. Biol.* **21,** 659–693
17. Samad, T. A., Rebbapragada, A., Bell, E., Zhang, Y., Sidis, Y., Jeong, S. J., Campagna, J. A., Perusini, S., Fabrizio, D. A., Schneyer, A. L., Lin, H. Y., Brivanlou, A. H., Attisano, L., and Woolf, C. J. (2005) *J. Biol. Chem.* **280,** 14122–14129
18. Wang, R. H., Li, C., Xu, X., Zheng, Y., Xiao, C., Zerfas, P., Cooperman, S., Eckhaus, M., Rouault, T., Mishra, L., and Deng, C. X. (2005) *Cell Metab.* **2,** 399–409
19. Krijt, J., Vokurka, M., Chang, K. T., and Necas, E. (2004) *Blood* **104,** 4308–4310
20. Zhang, A. S., Anderson, S. A., Meyers, K. R., Hernandez, C., Eisenstein, R. S., and Enns, C. A. (2007) *J. Biol. Chem.* **282,** 12547–12556
21. Zhang, A. S., West, A. P., Jr., Wyman, A. E., Bjorkman, P. J., and Enns, C. A. (2005) *J. Biol. Chem.* **280,** 33885–33894
22. Lin, L., Goldberg, Y. P., and Ganz, T. (2005) *Blood* **106,** 2884–2889
23. Kuninger, D., Kuns-Hashimoto, R., Kuzmickas, R., and Rotwein, P. (2006) *J. Cell Sci.* **119,** 3273–3283
24. Lin, L., Nemeth, E., Goodnough, J. B., Thapa, D. R., Gabayan, V., and Ganz, T. (2008) *Blood Cells Mol. Dis.* **40,** 122–131
25. Silvestri, L., Pagani, A., and Camaschella, C. (2007) *Blood* **109,** 4305–4510
26. Lin, L., Valore, E. V., Nemeth, E., Goodnough, J. B., Gabayan, V., and Ganz, T. (2007) *Blood* **110,** 2182–2189
27. Babitt, J. L., Huang, F. W., Xia, Y., Sidis, Y., Andrews, N. C., and Lin, H. Y. (2007) *J. Clin. Investig.* **117,** 1933–1939
28. Wilson, N. H., and Key, B. (2007) *Int. J. Biochem. Cell Biol.* **39,** 874–878
29. Cole, S. J., Bradford, D., and Cooper, H. M. (2007) *Int. J. Biochem. Cell Biol.* **39,** 1569–1575
30. Wilson, M. D., Riemer, C., Martindale, D. W., Schnupf, P., Boright, A. P., Cheung, T. L., Hardy, D. M., Schwartz, S., Scherer, S. W., Tsui, L. C., Miller, W., and Koop, B. F. (2001) *Nucleic Acids Res.* **29,** 1352–1365
31. Matsunaga, E., and Chedotal, A. (2004) *Dev. Growth Differ.* **46,** 481–486
32. Vielmetter, J., Kayyem, J. F., Roman, J. M., and Dreyer, W. J. (1994) *J. Cell Biol.* **127,** 2009–2020
33. Meyerhardt, J. A., Look, A. T., Bigner, S. H., and Fearon, E. R. (1997) *Oncogene.* **14,** 1129–1136
34. Keeling, S. L., Gad, J. M., and Cooper, H. M. (1997) *Oncogene.* **15,** 691–700
35. Wilson, N. H., and Key, B. (2006) *Dev. Biol.* **296,** 485–498
36. Mawdsley, D. J., Cooper, H. M., Hogan, B. M., Cody, S. H., Lieschke, G. J., and Heath, J. K. (2004) *Dev. Biol.* **269,** 302–315
37. Silvestri, L., Pagani, A., Fazi, C., Gerardi, G., Levi, S., Arosio, P., and Camaschella, C. (2007) *Blood* **109,** 4503–4510
38. Altschuler, Y., Barbas, S. M., Terlecky, L. J., Tang, K., Hardy, S., Mostov, K. E., and Schmid, S. L. (1998) *J. Cell Biol.* **143,** 1871–1881
39. VanSlyke, J. K., and Musil, L. S. (2005) *Mol. Biol. Cell* **16,** 5247–5257
40. Hammond, D. E., Carter, S., McCullough, J., Urbe, S., Vande Woude, G., and Clague, M. J. (2003) *Mol. Biol. Cell* **14,** 1346–1354
41. Schmidt, A., Hannah, M. J., and Huttner, W. B. (1997) *J. Cell Biol.* **137,** 445–458
42. Roy, C. N., Penny, D. M., Feder, J. N., and Enns, C. A. (1999) *J. Bio. Chem.* **274,** 9022–59028
43. Yang, F., West, A. P., Jr., Allendorph, G. P., Choe, S., and Bjorkman, P. J. (2008) *Biochemistry* **47,** 4237–4245
44. Bowman, E. J., Siebers, A., and Altendorf, K. (1988) *Proc. Natl. Acad. Sci.*

U. S. A. **85,** 7972–7976
45. Mayor, S., and Pagano, R. E. (2007) *Nat. Rev.* **8,** 603–612
46. Macia, E., Ehrlich, M., Massol, R., Boucrot, E., Brunner, C., and Kirchhausen, T. (2006) *Dev. Cell* **10,** 839–850
47. Chadda, R., Howes, M. T., Plowman, S. J., Hancock, J. F., Parton, R. G., and Mayor, S. (2007) *Traffic* **8,** 702–717
48. Orlandi, P. A., and Fishman, P. H. (1998) *J. Cell Biol.* **141,** 905–915
49. Nichols, B. J., Kenworthy, A. K., Polishchuk, R. S., Lodge, R., Roberts, T. H., Hirschberg, K., Phair, R. D., and Lippincott-Schwartz, J. (2001) *J. Cell Biol.* **153,** 529–541
50. Subtil, A., Gaidarov, I., Kobylarz, K., Lampson, M. A., Keen, J. H., and McGraw, T. E. (1999) *Proc. Natl. Acad. Sci. U. S. A.* **96,** 6775–6780
51. Mayor, S., and Riezman, H. (2004) *Nat. Rev. Mol. Cell Biol.* **5,** 110–120
52. Thomas, G. (2002) *Nat. Rev.* **3,** 753–766

Appendix B

Published as Zhang AS, Yang F, Wang J, Tsukamoto H, Enns CA. (2009) Hemojuvelin-Neogenin Interaction Is Required for Bone Morphogenic Protein-4-induced Hepcidin Expression. *Journal of Biological Chemistry* **284**(34):22580-9.

THE JOURNAL OF BIOLOGICAL CHEMISTRY VOL. 284, NO. 34, pp. 22580–22589, August 21, 2009
Printed in the U.S.A.

Hemojuvelin-Neogenin Interaction Is Required for Bone Morphogenic Protein-4-induced Hepcidin Expression*[S]

Received for publication, February 19, 2009, and in revised form, June 4, 2009 Published, JBC Papers in Press, June 29, 2009, DOI 10.1074/jbc.M109.027318

An-Sheng Zhang[‡1], Fan Yang[§], Jiaohong Wang[¶], Hidekazu Tsukamoto[¶‖], and Caroline A. Enns[‡]

From the [‡]Department of Cell and Developmental Biology, Oregon Health and Science University, Portland, Oregon 97239, the [§]Division of Biology, California Institute of Technology, Pasadena, California 91125, the [¶]Department of Pathology, Keck School of Medicine of the University of Southern California, Los Angeles, California 90033, and the [‖]Department of Veteran Affairs, Greater Los Angeles Healthcare System, Los Angeles, California 90073

Hemojuvelin (HJV) is a glycosylphosphatidylinositol-linked protein and binds both bone morphogenic proteins (BMPs) and neogenin. Cellular HJV acts as a BMP co-receptor to enhance the transcription of hepcidin, a key iron regulatory hormone secreted predominantly by liver hepatocytes. In this study we characterized the role of neogenin in HJV-regulated hepcidin expression. Both HJV and neogenin were expressed in liver hepatocytes. Knockdown of neogenin decreased BMP4-induced hepcidin mRNA levels by 16-fold in HJV-expressing HepG2 cells but only by about 2-fold in cells transfected with either empty vector or G99V mutant HJV that does not bind BMPs. Further studies indicated that disruption of the HJV-neogenin interaction is responsible for a marked suppression of hepcidin expression. Moreover, *in vivo* studies showed that hepatic hepcidin mRNA could be significantly suppressed by blocking the interaction of HJV with full-length neogenin with a soluble fragment of neogenin in mice. Together, these results suggest that the HJV-neogenin interaction is required for the BMP-mediated induction of hepcidin expression when HJV is expressed. Combined with our previous studies, our results support that hepatic neogenin possesses two functions, mediation of cellular HJV release, and stimulation of HJV-enhanced hepcidin expression.

Iron is an indispensable nutrient required for a variety of biochemical processes such as respiration, metabolism, and DNA synthesis. Iron homeostasis in the body is regulated primarily by the rate of iron absorption from the intestine.

Mutations in the key iron homeostatic proteins result in either hereditary hemochromatosis or iron-deficient anemia (1–4). Hereditary hemochromatosis is a heterogeneous group of inherited iron overload disorders linked to mutations in several genes including *HFE*, *HFE2*, *HAMP* (the hepcidin gene), and *TFR2*. *HFE2* is a recently cloned gene encoding the protein hemojuvelin (HJV)[2] (5). Both the *HFE2* mRNA and protein are highly expressed in skeletal muscles and the heart and at lower levels in the liver (5, 6).

HJV plays a pivotal role in iron homeostasis. Homozygous or compound heterozygous mutations in *HFE2* are the major cause of juvenile hemochromatosis (5), a particularly severe form of hereditary hemochromatosis (7, 8). The marked suppression of hepatic hepcidin expression observed in juvenile hemochromatosis patients with *HFE2* mutations as well as in HJV knock-out ($Hjv^{-/-}$) mice has implicated HJV as a critical upstream regulator of hepcidin transcription (5, 9, 10). Hepcidin, the key iron regulatory hormone, is predominantly expressed in liver hepatocytes, and iron levels in the body positively regulate its expression (11, 12). In the liver HJV is found predominantly in hepatocytes (10), where it regulates hepcidin expression.

HJV is a glycosylphosphatidylinositol-linked membrane-bound protein and is either associated with cells or released by proteolytic cleavage in a soluble form. Cellular HJV acts as a co-receptor for bone morphogenic proteins (BMPs), BMP2, BMP4, BMP5, and BMP6 to enhance the transcription of hepcidin through the BMP-signaling cascade (13, 14). Binding of BMP ligands to BMP receptor complexes on the cell surface triggers the phosphorylation of Smad1, Smad5, and Smad8 (Smad1/5/8) in the cytoplasm. The phosphorylated Smads (pSmad1/5/8) form heteromeric complexes with Smad4 and then translocate into the nucleus where they induce the transcription of target genes (15). Liver-specific disruption of Smad4 in mice markedly decreases hepcidin expression and causes severe iron accumulation in different organs, further supporting the pivotal role of BMP signaling in the regulation of hepcidin expression (16).

HJV cleavage and subsequent release constitutes the major pathway of cellular HJV turnover in HepG2 cells transfected to express HJV (17). Functional studies reveal that soluble HJV suppresses BMP-induced hepcidin expression both *in vitro* and when injected into mice, likely through competition with membrane-associated HJV for limited BMPs (14, 18). Previous studies suggest that HJV release may involve retrograde trafficking of HJV from the plasma membrane to the Golgi/trans-Golgi network compartment, where it may be subjected to cleavage

* This work was supported, in whole or in part, by National Institutes of Health Grants DK080765 (to A.-S. Z.), P50AA11199 (to H. T.), and R24AA12885 (to H. T.).

[S] The on-line version of this article (available at http://www.jbc.org) contains supplemental Figs. 1–3.

[1] To whom correspondence should be addressed: Dept. of Cell and Developmental Biology L215, Oregon Health and Science University, 3181 SW Sam Jackson Park Rd., Portland, OR 97239. Tel.: 503-494-5846; Fax: 503-494-4253; E-mail: zhanga@ohsu.edu.

[2] The abbreviations used are: HJV, hemojuvelin; BMP, bone morphogenic protein; CM, conditioned culture medium; dox, doxycycline; GAPDH, glyceraldehyde phosphate dehydrogenase; HSC, hepatic stellate cells; neo, neogenin; qRT-PCR, quantitative real-time PCR; RGM, repulsive guidance molecule; tTA, tetracycline controlled transactivator; FCI, furin convertase inhibitor; MEM, minimum essential medium; FCS, fetal calf serum; NEAA, nonessential amino acids; Neo, neogenin.

Supplemental Material can be found at:
http://www.jbc.org/content/suppl/2009/06/29/M109.027318.DC1.html

by the proprotein convertase furin, followed by rapid release from cells (17, 19, 20). Interaction of HJV with neogenin, a type I membrane protein expressed in most tissues including the liver (21), is required for HJV release from different cell lines (6, 17).

In this study we characterized the role of neogenin in HJV-regulated hepcidin expression. Our results indicated that HJV and neogenin are co-expressed in liver hepatocytes. Surprisingly, the HJV-neogenin interaction is required for the induction of hepcidin expression by BMP4 in addition to its role of mediating HJV release from cells.

EXPERIMENTAL PROCEDURES

Quantitative Real-time RT-PCR (qRT-PCR)— qRT-PCR was used to analyze the mRNA levels of HFE2, neogenin, and GAPDH in isolated rat liver hepatocytes, Kupffer cells, sinusoidal endothelial cells, and hepatic stellate cells (HSC) as well as the mRNA levels of hepcidin and GAPDH in HepG2 cells and mouse livers. Total RNA isolation and cDNA preparation were previously described (22). qRT-PCR analysis was performed using primers specific for rat genes and human GAPDH as previously reported (6, 22, 23). The sequences of other primers are 5′-ggctctgttttcccacaacag-3′ (forward, human hepcidin), 5′-tccttcgcctctggaacatgg-3′ (reverse, human hepcidin), 5′-aaatatgacaactcactcaagattgtca-3′ (forward, mouse GAPDH), 5′-cccttccacaatgccaaagt-3′ (reverse, mouse GAPDH), 5′-ctgagcagcaccacctatctc-3′ (forward, mouse hepcidin), and 5′-tggctctaggctatgttttgc-3′ (reverse, mouse hepcidin). The results for each gene of interest are expressed as the amount relative to that of GAPDH in each sample.

Cell Culture and Transfection—HepG2 cells were purchased from ATCC and maintained in MEM, 10% FCS, 1 mM pyruvate/1× nonessential amino acids (complete medium). HepG2 cells stably expressing G99V HJV (G99V-HepG2) were generated using the Nucleofector kit V (Amaxa Biosystems) as previously described (6). HepG2 cells stably transfected with wild type HFE2 (HJV-HepG2) or pcDNA3 empty vector (control-HepG2) were generated previously (6, 24). The stably transfected cells were maintained in complete medium with 800 μg/ml G418.

HepG2 cells stably transfected with the tetracycline repressor (tTA-HepG2) were obtained from Dr. Gregory Longmore at Washington University, St. Louis (25). tTA-HepG2-HJV and tTA-HepG2-G99V HJV cells were generated by subcloning HFE2 or G99V HFE2 cDNA into a tetracycline-inducible pcDNA4 vector, respectively, followed by a stable transfection into tTA-HepG2 cells. Transfected cells were maintained in complete medium with 800 μg/ml G418 and 5 μg/ml blasticidin and induced to express HJV using 2 μg/ml doxycycline (dox), a tetracyline homolog. tTA-HepG2 cells transfected with empty pcDNA4 vector (tTA-HepG2-control) were also generated and used as controls.

Mutagenesis—The G99V mutant HFE2 cDNA was generated using the QuikChange™ XL site-directed mutagenesis kit (Stratagene) following the manufacturer's instructions. pcDNA3-HFE2 construct was used as a template. The primers used to introduce the mutation were 5′-ccgcacctgccgcgtggacctcgccttcc-3′ (forward) and 5′-ggaaggcgaggtccacgcggcaggtgcgg-3′ (reverse). The mutation in the resulting construct was confirmed by DNA sequencing. No other sequence change was detected.

BMP4 Treatment—tTA-HepG2-HJV, -G99V HJV, or -control cells were subcultured into 12-well plates. After 48 h of incubation, cells at about 60% confluence were incubated with MEM, 1 mM pyruvate, 1× nonessential amino acids (NEAA), 1% FCS plus 2 μg/ml dox for 6 h to serum starve the cells and to induce HJV expression. Cells were then incubated in the same medium with BMP4 (R&D Systems, Inc.) at the indicated concentrations for the time intervals described in each figure legend. In some studies 40 nM soluble neogenin fibronectin type III 5–6 domain (Neo FNIII 5–6) or 5 μM decanoyl-Arg-Val-Lys-Arg-chloromethyl ketone (Alexis Biochemicals), a furin convertase inhibitor (FCI), was also included. For Western blot analysis, the conditioned medium (CM) was collected, and cell lysate was prepared for the immunodetection of HJV in both CM and lysate as well as for the immunodetection of phosphorylated Smad1/5/8 (pSmad) and β-actin in the lysates. For qRT-PCR analysis of hepcidin and GAPDH mRNA, total cellular RNA was isolated as described under "Quantitative Real-time RT-PCR." Neo FNIII 5–6 fragment specifically binds HJV with a K_D in the subnanomolar range. Purified Neo FNIII 5–6 was generated from baculovirus as previously described (26).

Knockdown of Endogenous Neogenin—SMARTpool siRNA specific for human neogenin (Dharmacon) was used to knock down the endogenous neogenin in control-, HJV-, and G99V HJV-HepG2 cells as previously described (6). RNAiMAX reagent (Invitrogen) was used for the transfection. The negative control siRNA was previously described (6). siRNA transfection was conducted in 12-well plates in complete medium. About 48-h after transfection, cells were serum-starved with MEM, 1 mM pyruvate, 1× NEAA, 1% FCS for 6 h followed by incubation with the same medium (1 ml per well) supplemented with 0, 0.5, 1, and 5 ng/ml BMP4 for 16 h. CM was then collected, and cell lysate was prepared for immunodetection. Total cellular RNA was isolated for qRT-PCR analysis.

For neogenin rescue studies HJV-HepG2 cells were first transfected with either control or neogenin siRNA. On the following day cells were transfected with either human neogenin cDNA or pcDNA3 empty vector using FuGENE HD transfection reagent (Roche Applied Science). On day 3, cells were serum-starved with MEM, 1 mM pyruvate, 1× NEAA, 1% FCS for 6 h followed by incubation with the same medium (1 ml per well) supplemented with 5 ng/ml BMP4 for 16 h. About 72 h after the siRNA transfection, CM was collected, cell lysate was prepared for immunodetection, and total RNA was isolated for qRT-PCR analysis.

Flow Cytometry—Flow cytometry was used to quantify cell surface HJV in HJV-HepG2 cells after treatment with or without 40 nM Neo FNIII 5–6 for 16 h as well as in G320V HJV, D172E HJV, and G99V HJV-HepG2 cells. Cells were detached from flasks with cell dissociation buffer (Invitrogen). Cells were then incubated with affinity-purified rabbit anti-HJV antibody (4 μg/ml) in Hanks' buffer supplemented with 3% fetal bovine serum for 30 min at 4 °C, washed, and incubated with phycoerythrin-conjugated goat anti-rabbit IgG (1:500 dilution) (Caltag, Burlingame, CA) in the same buffer for 30 min at 4 °C. Flow cytometry analysis was performed on a BD Biosciences

FACSCalibur flow cytometer. Rabbit IgG and control-HepG2 cells were used as negative controls. The levels of cell surface HJV are expressed as arbitrary units (6).

Immunodetection—Cell lysates from the isolated rat liver cells and HepG2 cells were prepared using NET-Triton (150 mM NaCl, 5 mM EDTA, 10 mM Tris (pH 7.4), and 1% Triton X-100) supplemented with 1× protease inhibitor mixture (Roche Applied Science), 1 mM sodium fluoride (Sigma), and 1 mM sodium orthovanadate (Sigma). Proteins from the isolated liver cells (250 μg), whole cell extract from 1 well of a 12-well plate, and conditioned medium (120 μl) were separated using 11% SDS-PAGE under reducing conditions followed by transfer onto nitrocellulose membrane. Membranes were probed with affinity-purified rabbit anti-HJV antibody (0.22 μg/ml) (21), rabbit anti-neogenin antibody (0.4 μg/ml, Santa Cruz Biotechnology), rabbit anti-phosphorylated Smad1/5/8 (1:1,000; Cell Signaling Technology), or mouse anti-β-actin antibody (1:10,000; Chemicon International, Temecula, CA) followed by immunodetection using corresponding horseradish peroxidase-conjugated secondary antibodies (Chemicon International). The chemiluminescent bands were exposed to x-ray film (Super Signal, Pierce).

Neo FNIII 5–6 Injection—Eight-week-old male 129EvSv mice were injected intraperitoneally with purified Neo FNIII 5–6 at 3 mg/kg body weight or carrier buffer twice on the same day at 8:30 a.m. and 3:30 p.m. Injected mice had free access to the regular rodent diet. At 24 h after the first injection, animals were euthanized while under anesthesia. Liver tissues were collected for qRT-PCR analysis of hepcidin and GAPDH mRNA. Each group consisted of three mice. All the procedures were approved by the Institutional Animal Care and Use Committee of Oregon Health and Science University.

Statistical Analysis—The S.D. and the paired two-tailed Student's *t* test were used to compare two sets of data. The one-way analysis of variance and Tukey's post-test were used to compare three or more sets of data.

RESULTS

HJV and Neogenin Are Co-expressed in Hepatocytes—We sought to explore the role of neogenin in HJV-regulated hepcidin expression in hepatocytes *in vivo* because previous studies demonstrated that HJV binds neogenin and that the HJV-neogenin interaction is required for HJV release (11, 21, 22). We first examined the expression profiles of HFE2 and neogenin mRNA and proteins in the liver using isolated rat liver hepatocytes, Kupffer cells, sinusoidal endothelial cells, and HSC. Consistent with findings in a previous report (10), both HFE2 mRNA and protein were detected predominantly in hepatocytes (Fig. 1, *A* and *C*). In contrast, both neogenin mRNA and protein were detected in all liver cell populations (Fig. 1, *B* and *C*). The highest level of neogenin mRNA was found in HSC, ~3.7-, ~12.9-, and ~7.3-fold greater than in hepatocytes, Kupffer cells, and sinusoidal endothelial cells, respectively (Fig. 1*B*). Immunoblots revealed a similar profile of neogenin protein expression (Fig. 1*C*, *upper panel*). In the liver, hepatocytes account for approximate 65% in cell number and 80% in volume, but HSCs only account for approximate 5–8% in cell number and 1.4% in volume (27). Therefore, these results sug-

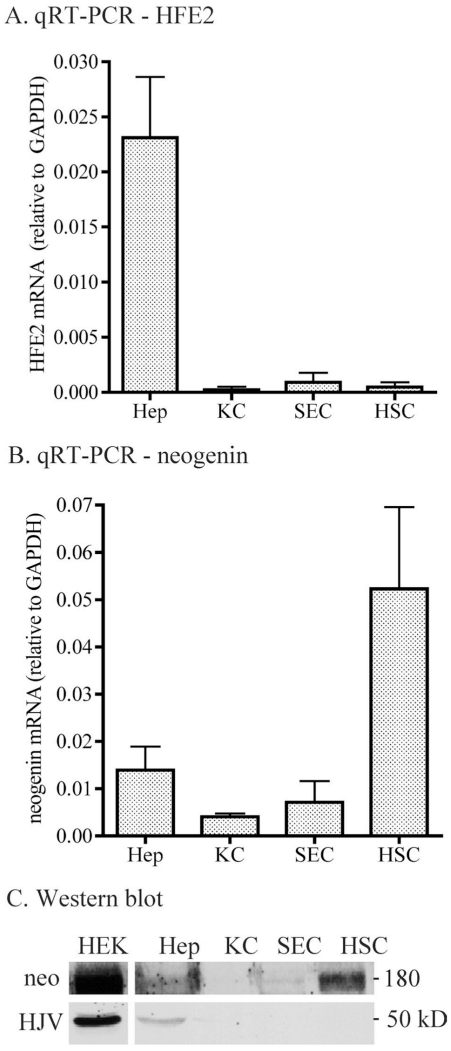

FIGURE 1. **HFE2 and neogenin expression profiles in isolated rat liver cells.** *A*, qRT-PCR analysis of HFE2 mRNA in isolated rat liver hepatocytes (Hep, $n = 5$), Kupffer cells (*KC*, $n = 7$), sinusoidal endothelial cells (*SEC*, $n = 4$), and hepatic stellate cells (HSC, $n = 6$). Results are expressed as the amounts relative to GAPDH. The mean values and the S.D. for each cell population are presented. *B*, qRT-PCR analysis of neogenin mRNA in isolated rat liver cell populations. The analysis was performed as described in *A*. *C*, Western blot analysis of HJV and Neo proteins in isolated rat liver cells. Cell extract protein (250 μg) was separated in SDS-PAGE under reducing conditions. Equal protein loading was confirmed by Ponceau S staining of the membrane (not shown). Membranes were probed with antibodies against HJV and neogenin. Cell lysate from HEK293 cells stably expressing both HJV and neogenin (*HEK*) was included as a positive control. Experiments were performed using two different sets of isolated cells and showed consistent results.

Supplemental Material can be found at:
http://www.jbc.org/content/suppl/2009/06/29/M109.027318.DC1.html

gest that hepatocytes are also the major site of neogenin expression in the liver.

In situ hybridization and immunohistochemistry analysis revealed that both HFE2 mRNA and protein were evenly detected in hepatocytes in rat liver tissues with no evidence of a zonal distribution (supplemental Fig. 1, *A* and *B*). Neogenin mRNA and protein were observed in hepatocytes as well as in non-parenchymal cells throughout the liver tissues (supplemental Fig. 1, *A* and *B*). Together, the above results indicate that HJV and neogenin are co-expressed in hepatocytes.

BMP4 Induces Hepcidin Expression in HepG2 Cells—Hepcidin expression is induced via the BMP-signaling cascade (13, 16). We wanted to use the hepatoma cell lines HepG2 cells and tTA-HepG2 cells, where proteins can be expressed in a tetracycline-dependent manner, as model systems to determine the role of neogenin in HJV-regulated hepcidin expression. They are relatively differentiated hepatoma cell lines that express hepcidin, neogenin (24), and many other hepatocyte-specific genes but have no detectable HJV protein by Western blot analysis (data not shown). HFE2 mRNA levels are close to the limit of detection by qRT-PCR and are about 1300-fold lower than in human liver tissue (data not shown).

We first titrated the response of tTA-HepG2 cells to BMP4, a ligand for both HJV and BMP receptors that is expressed in the liver (14, 28). Induction of hepcidin could be detectable at as low as 0.1 ng/ml BMP4 as measured by qRT-PCR. Increases in hepcidin mRNA of 1.8-, 3.5-, 13.4-, 130-, 212-, 310-, and 371-fold were detected with the addition of 0.1, 0.5, 1, 5, 10, 25, and 50 ng/ml BMP4, respectively. The induction was nearly linear up to 5 ng/ml BMP4 when cells were treated with BMP4 for 18 h (Fig. 2). On the basis of these observations, a concentration of 5 ng/ml BMP4 was chosen for our studies. At 5 ng/ml BMP4, hepcidin mRNA levels were increased by 130-fold in tTA-HepG2 cells, indicating that BMP4 can induce hepcidin transcription independently of HJV. These results are consistent with previous studies showing that BMP2 induces hepcidin expression in the primary hepatocytes isolated from *Hjv*$^{-/-}$ mice (13). HepG2 cells are, thus, an appropriate cell line to study the effects of neogenin and different constructs of HJV on hepcidin expression.

Knockdown of Neogenin Suppresses Hepcidin Expression Markedly When HJV Is Expressed—Soluble HJV suppresses BMP-induced hepcidin expression through competition with membrane-associated HJV for a limited BMP supply (14, 18). We wanted to test the hypothesis that neogenin negatively regulates hepcidin expression by facilitating the release of HJV from cells as shown previously (24). Endogenous neogenin was knocked down in HepG2 cells stably transfected with HFE2 (HJV) or empty vector (control). The responses of BMP signaling and hepcidin expression to BMP4 treatment were then examined.

First, we tested the effects of neogenin knockdown on BMP signaling and hepcidin mRNA in the presence of 5 ng/ml BMP4 (Fig. 3, *A* and *B*). A single transfection of neogenin siRNA significantly decreased the levels of endogenous neogenin in control and HJV-HepG2 cells (Fig. 3*A*, *top panel*). The accumulation of cellular HJV detected in HJV-HepG2 cells with neogenin knockdown (Fig. 3*A*) is consistent with a previous study, in

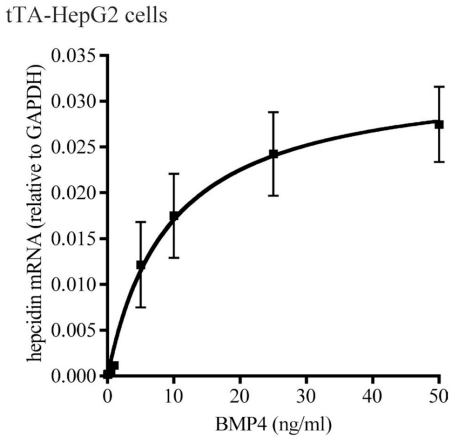

FIGURE 2. **Titration of the response of hepcidin mRNA expression to BMP4.** tTA-HepG2 cells were subcultured into 12-well plates. After 48 h of incubation, cells at about 60% confluence were first incubated with MEM, 1 mM pyruvate, 1× NEAA, 1% FCS for 6 h to serum starve the cells. Cells were then incubated in the same medium with BMP4 at 0, 0.1, 0.5, 1, 5, 10, 25, and 50 ng/ml for 18 h followed by total RNA isolation, cDNA preparation, and qRT-PCR analysis of hepcidin and GAPDH mRNA. The hepcidin mRNA levels are expressed as the amount relative to that of GAPDH in each specific sample. The results are from three separate experiments, and the mean values and the S.D. are presented.

which a soluble neogenin whole ectodomain that binds HJV was used to block HJV release (17). HJV-HepG2 cells have lower base-line levels of pSmad than control-HepG2 cells (Fig. 3*A*). Because HepG2 cells were stably transfected with HJV and clonally selected, differences in basal levels in the selected clones could account for this observation.

Contrary to our initial hypothesis, neogenin knockdown resulted in a 16-fold decrease, rather than an increase, in hepcidin mRNA in HJV-HepG2 cells and about a 2-fold decrease in control-HepG2 cells compared with their corresponding controls (Fig. 3*B*). Because hepcidin expression is induced by the BMP-signaling pathway (13, 16), the results of hepcidin mRNA were verified by examining the effects of neogenin knockdown on BMP signaling. Levels of phosphorylated Smad1/5/8 (pSmad) are a direct indicator of BMP receptor activation. In agreement with the reduced induction of hepcidin mRNA, immunoblots revealed decreased pSmad in neogenin-depleted cells (Fig. 3*A*). Therefore, these results suggest that the suppression of hepcidin expression in both control and HJV-HepG2 cells after neogenin knockdown results from decreased BMP signaling.

To determine whether the inhibition is BMP4-dependent, we next examined the effects of neogenin knockdown on hepcidin expression in HJV-HepG2 cells with the addition of 0, 0.5, and 1 ng/ml concentrations of exogenous BMP4. A similar level of inhibition was obtained under each condition (Fig. 3*C*). These results indicate that when HJV is expressed, the suppression of hepcidin expression by neogenin knockdown is independent of the addition of exogenous BMP4. Because the levels of HJV mRNA in the control-HepG2 cells

Neogenin and Hepcidin Expression

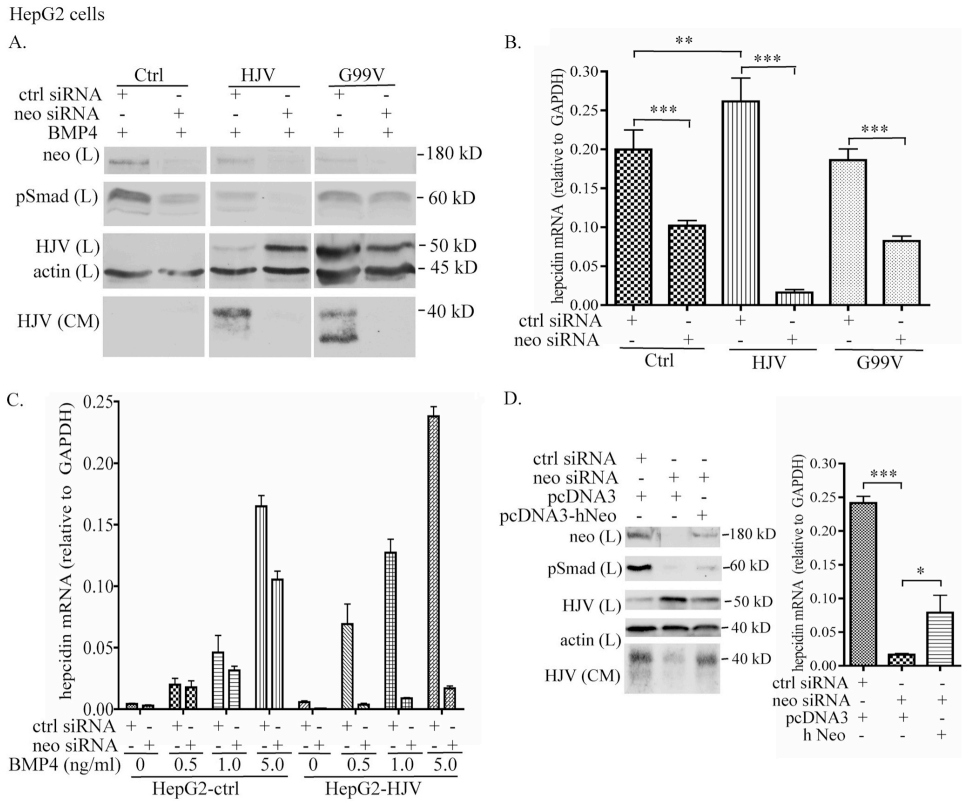

FIGURE 3. **Knockdown of neogenin suppresses BMP4-induced hepcidin expression.** A, knockdown of neogenin decreases pSmad1/5/8. Control-, HJV-, and G99V HJV-HepG2 cells in 12-well plates were transfected with either control (*Ctrl*) or neogenin (*Neo*) siRNA using RNAiMAX reagent. After about 48 h, cells were serum-starved for 6 h followed by incubation with the same medium (1 ml/well) supplemented with 5 ng/ml BMP4 for 16 h. CM was then collected, and cell lysate was prepared. About 15% of CM and the total lysate were subjected to SDS-PAGE followed by immunodetection of neogenin (*Neo*), pSmad1/5/8 (*pSmad*), HJV, and β-actin in the lysate (*L*) and HJV in CM. *B*, knockdown of neogenin decreases the BMP4-induced hepcidin mRNA. Neogenin knockdown and BMP4 treatment in control-, HJV-, and G99V HJV-HepG2 cells were performed in essentially the same manner as described in *A*. Total RNA was isolated followed by cDNA preparation and qRT-PCR analysis of hepcidin and GAPDH mRNA. The hepcidin mRNA levels are expressed as the amount relative to that of GAPDH in each specific sample. *C*, knockdown of neogenin decreases hepcidin mRNA in the absence of exogenous BMP4. All the experimental procedures were performed as described in *B* except that control- and HJV-HepG2 cells were incubated with different concentrations of BMP4 (0, 0.5, 1, and 5 ng/ml). *D*, neogenin rescue analysis. HJV-HepG2 cells were first transfected with either control (*Ctrl*) or neogenin (*Neo*) siRNA on day 1. About 24 h later, cells were introduced with either human neogenin cDNA (*hNeo*) or pcDNA3 empty vector (*pcDNA3*). On day 3, cells were serum-starved with MEM, 1 mM pyruvate, 1× NEAA, 1% FCS for 6 h followed by incubation with the same medium (1 ml/well) supplemented with 5 ng/ml BMP4 for 16 h. At about 72 h after the siRNA transfection, CM was collected, and cell lysate was prepared for immunodetection (*left panel*) as well as for qRT-PCR analysis of hepcidin mRNA (*right panel*) as described in *A* and *B*, respectively. All the experiments were repeated at least three times with consistent results. The qRT-PCR results in *B* and *D* were assessed by one-way analysis of variance, and the statistical significant differences relative to the corresponding controls were determined by Tukey's post-test. *, $p < 0.05$; **, $p < 0.01$; ***, $p < 0.001$.

are negligible compared with human liver tissues or HJV-HepG2 cells (data not shown), these results suggest that in the presence of no or very low levels of HJV, neogenin acts to maintain the basal levels of BMP signaling, and the resulting hepcidin expression. In contrast, the marked suppression of hepcidin expression detected in HJV-HepG2 cells depleted of neogenin implies that when HJV is expressed, neogenin is required for full extent of the induction of hepcidin expression by BMP4.

To rule out the possibility that the inhibitory effect detected in neogenin-depleted HJV-HepG2 cells results from an off-target effect, we conducted a neogenin rescue study. Transfection of cells with neogenin after endogenous neogenin knockdown was able to partially rescue the HJV release (Fig. 3*D*, *left panel*) as well as the hepcidin expression (Fig. 3*D*, *right panel*) induced by BMP4 at 5 ng/ml. The lack of a complete rescue might be because of the low transfection efficiency of neogenin cDNA. These results, therefore, suggest that the effect of neogenin

Supplemental Material can be found at:
http://www.jbc.org/content/suppl/2009/06/29/M109.027318.DC1.html

knockdown in HJV-HepG2 cells is not caused by an off-target effect.

HepG2 cells have higher basal levels of hepcidin mRNA than tTA-HepG2 cells (Fig. 3*B versus* Fig. 2). tTA-HepG2 cells were derived by selecting a clone of HepG2 cells stably transfected with the tTA tetracycline repressor (25) and, thus, could account for the lower basal levels of hepcidin than the parent cell line.

Neogenin Knockdown Does Not Markedly Suppress Hepcidin Expression when G99V HJV Is Expressed—HJV can simultaneously bind both BMP2 and neogenin (26). G99V mutant HJV is a non-functional form of HJV. In humans G99V substitution in HJV causes juvenile hemochromatosis (5). G99V HJV binds neogenin (supplemental Fig. 2*A*) but not BMPs (29). To determine whether or not the suppression of hepcidin expression detected in HJV-HepG2 cells after neogenin knockdown is because of the disruption of the HJV-neogenin interaction, we next examined the effect in HepG2 cells stably expressing the G99V mutant HJV. Because the interaction with neogenin is required for HJV release (6), G99V HJV behaved similarly to wild type HJV in its active release and plasma membrane expression (supplemental Fig. 2, *B* and *C*). Similar to HJV-HepG2 cells, neogenin knockdown blocked the release of G99V HJV from G99V HJV-HepG2 cells (Fig. 3*A*). However, in contrast to the marked suppression of hepcidin expression in HJV-HepG2 cells, knockdown of neogenin knockdown in G99V HJV-HepG2 cells only caused a mild decrease in hepcidin mRNA, which is similar to that in control-HepG2 cells (Fig. 3*B*). Together with the findings in both control and HJV-HepG2 cells, our results imply that neogenin dictates the extent of the induction of hepcidin expression only when it is associated with a functional HJV that can bind BMPs.

Blockage of HJV Release by a Furin Convertase Inhibitor Does Not Suppress BMP4-induced Hepcidin Expression—Because neogenin is not necessarily required for HJV trafficking to the plasma membrane (24), the dramatic suppression of BMP4-induced hepcidin expression in HJV-HepG2 cells with neogenin knockdown could result from either the inhibition of HJV release or the lack of HJV-neogenin association. To determine which of these processes is required for the induction of hepcidin expression, we first examined the role of HJV release in BMP4-induced hepcidin expression in tTA-HepG2-HJV cells, in which the expression of HJV was induced by the addition of dox. HJV release is mediated via cleavage by the proprotein convertase, furin (19, 20). tTA-HepG2-HJV cells were incubated with BMP4 to induce BMP signaling in the absence or presence of 5 μM FCI, which blocks the release of HJV. Blockage of HJV release by FCI mildly increased the levels of pSmad protein (Fig. 4*A*) and hepcidin mRNA (Fig. 4*B*). This is consistent with previous observations that soluble HJV suppresses BMP-induced hepcidin expression (14, 18). Thus, the suppression of hepcidin expression observed in HJV-HepG2 cells when neogenin expression is down-regulated does not result from the inhibition of HJV release.

Disruption of the HJV-Neogenin Interaction by a Soluble Neogenin Fragment Suppresses BMP4-induced Hepcidin Expression—The binding of neogenin to HJV maps to the fibronectin type III 5–6 domain (Neo FNIII 5–6) in the extracellular domain of

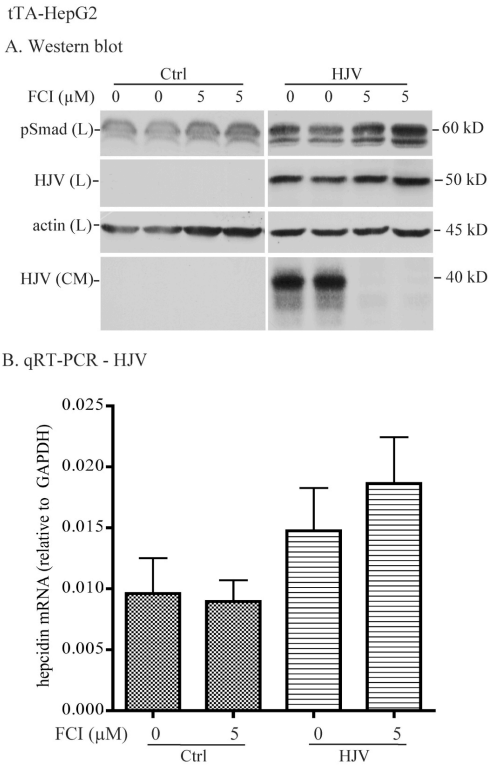

FIGURE 4. **Inhibition of HJV release by a furin convertase inhibitor does not suppress BMP4-induced hepcidin expression.** *A*, Western blot analysis. tTA-HepG2 cells stably expressing HJV or transfected with empty vector (*Ctrl*) were maintained in the absence of dox. At about 48 h after subculturing into 12-well plates, cells were first incubated with MEM, 1 mM pyruvate, 1× NEAA, 1% FCS plus 2 μg/ml dox for 6 h to serum starve the cells and to induce HJV expression. Cells were then incubated in the same medium containing 5 ng/ml BMP4 with or without 5 μM decanoyl-Arg-Val-Lys-Arg-chloromethyl ketone, a FCI, for 18 h. CM was collected, and cell lysates were prepared. About 20% of CM and the total lysate were subjected to SDS-PAGE followed by immunodetection of pSmad1/5/8 (*pSmad*), HJV, and β-actin in the lysate (*L*) and HJV in CM. This experiment was repeated three times with consistent results. *B*, qRT-PCR analysis of hepcidin mRNA. Incubation of tTA-HepG2-control and -HJV cells with FCI and BMP4 was performed in essentially the same manner as described in *A*. Total RNA was isolated followed by cDNA preparation and qRT-PCR analysis of hepcidin and GAPDH mRNA. The hepcidin mRNA levels are expressed as the amount relative to that of GAPDH in each specific sample. The results are from four separate experiments, and the mean values and the S.D. are presented.

neogenin (26). HJV can simultaneously bind both BMP2 and neogenin, suggesting that the binding sites do not overlap (26). To determine the effect of the HJV-neogenin interaction on BMP4-induced hepcidin expression, purified Neo FNIII 5–6 fragment was used to disrupt the interaction of HJV with the endogenously expressed full-length neogenin. tTA-HepG2 cells were used as a model system in which the expression of HJV or G99V HJV was under the control of tetracycline-inducible promoter. tTA-HepG2 cells stably transfected with wild

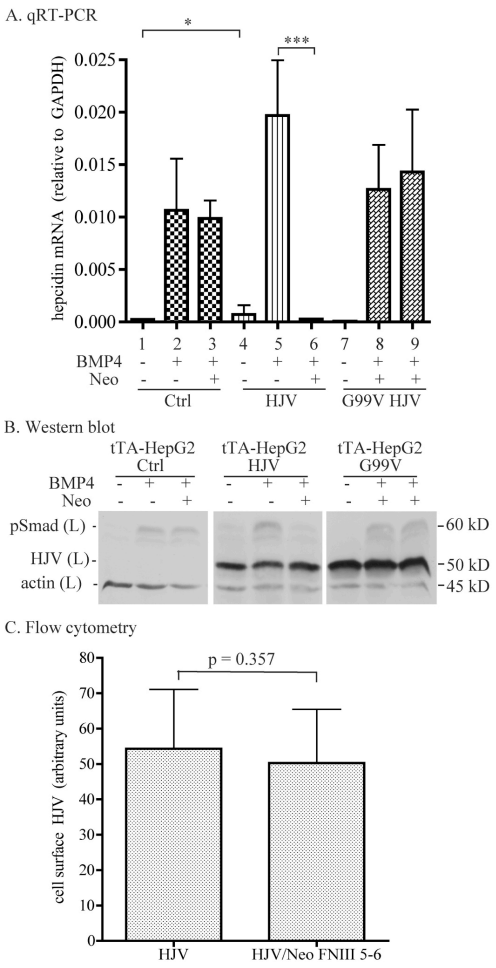

FIGURE 5. **Soluble neogenin suppresses BMP4-induced hepcidin expression only when HJV is expressed.** *A*, qRT-PCR analysis of hepcidin mRNA. tTA-HepG2 cells stably transfected with empty vector (control), HJV, or G99V HJV were maintained in the absence of dox. At about 48 h after subculturing into 12-well plates, cells were first incubated with MEM, 1 mM pyruvate, 1× NEAA, 1% FCS plus 2 μg/ml dox for 6 h to serum starve the cells and to induce HJV expression. Cells were then incubated in the same medium containing BMP4 at 0 or 5 ng/ml with or without 40 nM Neo FNIII 5–6 (*Neo*) for 18 h. Total RNA was isolated followed by cDNA preparation and qRT-PCR analysis of hepcidin and GAPDH mRNA. The hepcidin mRNA levels are expressed as the amount relative to that of GAPDH in each specific sample. The results are from four separate experiments and were assessed by one-way analysis of variance. The statistical significant differences relative to the corresponding controls were determined by Tukey's post test. *, $p < 0.05$; ***, $p < 0.001$. *B*, Western blot analysis. Incubation of tTA-HepG2-control, -HJV, and -G99V HJV cells with Neo FNIII 5–6 (*Neo*) and BMP4 was performed essentially the same as described in *A*. Total cell lysates (*L*) were subjected to SDS-PAGE followed by immunodetection of pSmad1/5/8 (*pSmad*), HJV, and β-actin. This experiment was repeated three times with consistent results. *C*, flow cytometry analysis of cell surface HJV after incubation with Neo FNIII 5–6. Control- and HJV-HepG2 cells were incubated with or without 40 nM Neo FNIII 5–6 for 18 h. Cells were then detached from flasks with cell dissociation buffer and incubated with affinity-purified rabbit anti-HJV antibody (4 μg/ml) in Hanks' buffer supplemented with 3% fetal bovine serum for 30 min at 4 °C followed by incubation with phycoerythrin-conjugated goat anti-rabbit IgG (1:500 dilution) in the same buffer for 30 min at 4 °C. Flow cytometry analysis was performed on a BD Biosciences FACSCalibur flow cytometer. Rabbit IgG and control-HepG2 cells were used as negative controls. The levels of cell surface HJV are expressed as arbitrary units. The results are from three separate experiments and the mean values and the S.D. are presented. *p* values are calculated using two-tailed Student's *t* test to compare the difference between the HepG2-HJV cells incubated with (*HJV/Neo FNIII 5–6*) and without (*HJV*) Neo FNIII 5–6.

type HFE2 (tTA-HepG2-HJV), G99V HFE2 (tTA-HepG2-G99V HJV), or empty vector (tTA-HepG2-control) were maintained in the absence of dox. Because the expression of HJV mRNA in the absence of dox could not be turned off completely in tTA-HepG2-HJV cells, as judged by qRT-PCR, tTA-HepG2-control and tTA-HepG2-G99V HJV cells were used as the controls in this study. The expression of HJV was induced by the addition of dox to the medium 6 h before cells were incubated with Neo FNIII 5–6 and BMP4. Cell lysates were collected 18 h later to analyze the hepcidin mRNA and pSmad protein levels by qRT-PCR and Western blot, respectively.

The addition of Neo FNIII 5–6 to cells suppresses BMP4-stimulated hepcidin expression. Expression of HJV, but not G99V HJV, increased hepcidin mRNA by about 3-fold (*1 versus 4*, Fig. 5*A*) and 1.8-fold (*2 versus 5*, Fig. 5*A*) without and with addition of 5 ng/ml BMP4, respectively. Upon treatment with both Neo FNIII 5–6 and BMP5, about a 70-fold decrease of BMP4-induced hepcidin mRNA was detected in tTA-HepG2-HJV cells (*5 versus 6*, Fig. 5*A*). In contrast, no significant change was observed in tTA-HepG2 control (*2 versus 3*, Fig. 5*A*) and G99V HJV (*8 versus 9*, Fig. 5*A*) cells under the same conditions. These results are consistent with the finding that HJV is a BMP co-receptor (13) and that Neo FNIII 5–6 disrupts the HJV-neogenin complex that augments BMP signaling.

In agreement with the levels of hepcidin mRNA (Fig. 5*A*), the addition of Neo FNIII 5–6 also prevented the induction of pSmad signaling by BMP4 in tTA-HepG2-HJV cells but not in tTA-HepG2-control or tTA-HepG2-G99V HJV cells (Fig. 5*B*). The lack of inhibition in tTA-HepG2-control or tTA-HepG2-G99V HJV cells suggests that Neo FNIII 5–6 does not affect the BMP signaling in the absence of wild type HJV. Given the findings that the HJV-neogenin interaction takes place at the plasma membrane (24), that Neo FNIII 5–6 disrupts the interaction of HJV with full-length neogenin (supplemental Fig. 3), and that HJV can simultaneously bind both BMP2 and neogenin (26), these data suggest that the interaction between HJV and neogenin after it reaches the cell surface is required for the induction of BMP-signaling by BMP4.

To rule out the possibility that the suppressed BMP signaling and hepcidin expression by Neo FNIII 5–6 is caused by the altered HJV trafficking to the plasma membrane, the effect of Neo FNIII 5–6 on cell surface HJV expression was examined. BMP signaling is initiated upon BMP binding to the BMP receptors on the cell surface (15). Our previous studies indicate that knockdown of neogenin does not affect HJV targeting to the plasma membrane (24). HJV-HepG2 cells were incubated in the presence or absence of Neo FNIII 5–6 for 18 h followed by flow cytometry analysis of cell sur-

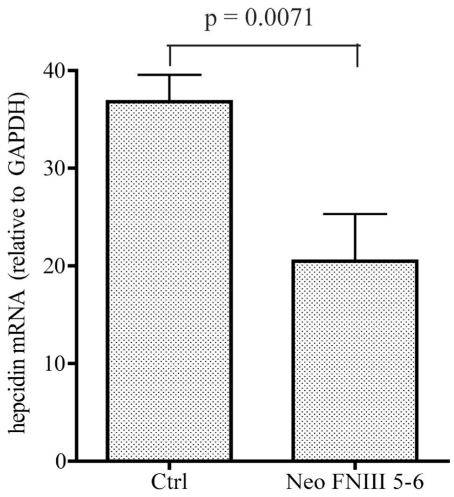

FIGURE 6. **Soluble neogenin suppresses hepatic hepcidin expression in mice.** Eight-week-old male 129EvSv mice were injected intraperitoneally with purified neogenin FNIII 5–6 (*Neo FNIII 5–6*) at 3 mg/kg body weight or the carrier buffer (*Ctrl*) twice at 8:30 am and 3:30 pm on the same day. Injected mice had free access to the regular rodent diet. At 24 h after the first injection, animals were euthanized while under anesthesia. Liver tissues were collected for qRT-PCR analysis of hepcidin and GAPDH mRNA. The hepcidin mRNA levels were calculated as the amount relative to that of GAPDH in each specific sample and are expressed as the amount relative to the carrier buffer-injected mice. Each group consisted of three mice. The mean values and the S.D. are presented. *p* values are calculated using two-tailed Student's *t* test to compare the difference between the two groups.

face HJV (24). Consistent with the neogenin knockdown study (24), Neo FNIII 5–6 did not significantly alter the cell surface HJV levels compared with the corresponding control (Fig. 5*C*). Together, these results indicate that Neo FNIII 5–6 suppresses BMP signaling and hepcidin expression by disrupting the interaction between full-length neogenin and HJV but not through its participation in HJV cleavage or by affecting its cell surface localization.

Soluble Neogenin Suppresses Hepatic Hepcidin Expression in Vivo—To determine whether the HJV-neogenin interaction is physiologically significant *in vivo*, we examined the effect of human Neo FNIII 5–6 on hepatic hepcidin expression in mice. Both neogenin and HJV are highly conserved between species. Our previous study showed that knockdown of neogenin in C2C12 cells, a mouse myoblast cell line, suppresses the release of transfected human HJV (6). Because the inhibition of HJV release in HepG2 cells is an immediate process (data not shown), purified Neo FNIII 5–6 at 3 mg/kg body weight was intraperitoneally injected into wild type male 129EvSv mice (8 weeks old) at 16 and 24 h before the collection of liver tissues. Control mice were injected with the same volume of carrier buffer. We used qRT-PCR to examine the levels of hepatic hepcidin mRNA. Injection of Neo FNIII 5–6 significantly suppressed hepcidin mRNA by ~40% ($p = 0.0071$) (Fig. 6). These results suggest that interaction of HJV with neogenin is required for the induction of hepcidin expression *in vivo*.

DISCUSSION

In this study we characterized the role of neogenin in HJV-regulated hepcidin expression. Results showed that both HJV and neogenin were expressed in liver hepatocytes and evenly detected throughout the liver tissues. Disruption of the interaction between HJV and neogenin by down-regulation of neogenin by siRNA or by the addition of a soluble neogenin fragment that binds HJV markedly decreased BMP4-induced hepcidin mRNA levels in HJV-expressing HepG2 cells. Together with the *in vivo* study using the HJV binding fragment of neogenin (FNIII 5–6) to disrupt the interaction between HJV and the full-length neogenin, our data support the idea that HJV-neogenin interaction enhances BMP-mediated induction of hepcidin expression.

To determine the role of neogenin in HJV-regulated hepcidin expression, we examined the expression profiles of HJV and neogenin in the liver. A previous report using lacZ protein as an indirect marker showed a selective expression of HJV, a critical upstream regulator of hepcidin transcription (5, 9, 10), in the hepatocytes around the portal triad (10). Here, using more direct methods, we confirmed the predominant expression of HJV in liver hepatocytes. But rather than a selective expression of HJV in hepatocyte cells in the periportal zone (10), our results indicate a uniform localization of both HJV mRNA and protein in hepatocytes throughout the tissue. Distinct from HJV, neogenin mRNA and protein were detected in all of the liver cell populations with the hepatocytes as the predominant source of neogenin. Thus, both HJV and neogenin are co-expressed in liver hepatocytes.

The significant inhibition of hepcidin expression by disrupting the HJV-neogenin interaction in HJV-expressing HepG2 cells was an unexpected result. Previous studies show that the interaction of HJV with neogenin is required for HJV release from hepatoma cell lines (HepG2 and Hep3B cells), a myoblast cell line (C2C12 cells), and HEK293 cells (6, 17, 24). Cellular HJV enhances the transcription of hepcidin through the BMP-signaling cascade by acting as a BMP co-receptor (13, 14), whereas the released soluble HJV is thought to serve as a BMP antagonist to suppress BMP-induced hepcidin expression through competition with membrane-associated HJV for limited BMPs (14, 18, 20). In HepG2 cells, HJV release constitutes the major pathway of cellular HJV turnover (17). Initially, we reasoned that blockage of HJV release by neogenin knockdown or a soluble neogenin would enhance BMP signaling and BMP4-induced hepcidin expression. However, the profound suppression of BMP signaling by both neogenin knockdown and treatment with Neo FNIII 5–6, but not by a furin convertase inhibitor that inhibits HJV release, leads us to conclude that the HJV-neogenin interaction is essential for the induction of BMP signaling and hepcidin expression in hepatocytes. Results from the further studies of G99V HJV, a non-functional form of HJV that causes juvenile hemochromatosis in humans (5), support that neogenin functions to guide the induction of BMP signaling and hepcidin expression only when it is associated with the HJV that binds both full-length neogenin and BMPs.

Neogenin and Hepcidin Expression

In contrast to HJV-HepG2 cells, we did not observe any significant effect on hepcidin expression when HepG2 cells transfected with empty vector or G99V HJV were incubated with soluble neogenin. However, we detected a 2-fold decrease of hepcidin expression when the endogenous neogenin in these cells was knocked down. These results imply that neogenin alone mildly enhances BMP signaling. Neogenin is a type I transmembrane protein. Recent studies showed that the neogenin 388-amino acid cytoplasmic domain is involved in various signal transduction pathways when associated with the repulsive guidance molecules a (RGMa) (30–33). The RGM family has three members (RGMa, RGMb, and RGMc). RGMc is the ortholog of HJV in mice. Similar to HJV, both RGMa and RGMb are glycosylphosphatidylinositol-linked proteins, bind neogenin, and are BMP coreceptors. In contrast to HJV, RGMa and RGMb are expressed primarily in the developing and adult central nervous system in distinct, mostly non-overlapping patterns (34–36). On the basis of the results in this study, we speculate that in the tissues that do not express HJV or RGMa or RGMb, neogenin may function to maintain the basal level of BMP signaling through its cytoplasmic domain. In the tissues that express either RGMa or RGMb, neogenin may play a similar role in the induction of BMP signaling as it does in the presence of HJV.

In this and our previous studies (17), we observed an interesting phenomenon. Both neogenin knockdown and treatment with either neogenin whole ectodomain or FNIII5–6 fragments can suppress the HJV release from HJV-HepG2 cells. But only the neogenin knockdown and neogenin whole ectodomain treatment result in the accumulation of cellular HJV. Flow cytometry analysis showed no significant change of cell surface HJV, suggesting that the increased cellular HJV does not result from the HJV accumulation at the cell surface. Immunofluorescence analysis revealed an increased accumulation of HJV in an uncharacterized intracellular compartment when neogenin is knocked down.[3] As a result, we speculate that cellular HJV accumulation may result from an altered HJV trafficking.

HJV release is negatively regulated by holo-transferrin and iron (6, 19, 20). The release of HJV from both a myoblast cell line and HepG2 cells depends on the interaction with neogenin (6). Although both HJV and neogenin are expressed in skeletal muscles and the liver (5, 6, 21), only the liver is the predominant site of hepcidin expression (11, 12). On the basis of these observations and the results obtained in this study, we hypothesize that the major function of hepatic neogenin is to augment the HJV-enhanced hepcidin expression through the BMP signaling pathway. We speculate that the major function of neogenin in the skeletal muscles, the major site of HJV expression in the body (5), is to mediate the release of HJV into circulation in response to the body iron status, which indirectly modulates the hepatic hepcidin expression.

In this study we found that the extent of inhibition of hepcidin expression by disrupting the HJV-neogenin interaction is independent of exogenous BMP4 ligand. Our findings are, therefore, not in agreement with the recent report showing that knockdown of neogenin has no evident effect on hepcidin expression in HJV-expressing cells (28). The basis for the difference between our results and theirs is not clear.

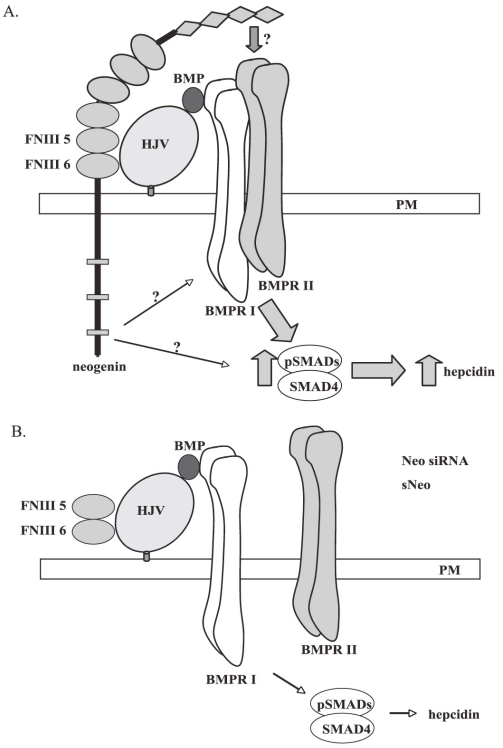

FIGURE 7. **A model of neogenin in HJV-induced hepcidin expression in hepatocytes.** *A*, HJV-neogenin is required for the proper assembly of HJV-BMP ligand-BMPR I/BMPR II complex to initiate the BMP signaling and to induce hepcidin expression. *B*, disruption of HJV-neogenin interaction either by neogenin (*Neo*) knockdown or by soluble neogenin (*sNeo*) leads to the formation of the aberrant and non-functional HJV-BMP ligand-BMPR I complex. *FNIII 5*, neogenin fibronectin type III 5 domain. *FNIII 6*, neogenin fibronectin type III 6 domain. *BMPRI*, type I BMP receptor. *BMPRII*, type II BMP receptor.

The BMP signaling cascade is initiated by ligand binding to two type I receptors followed by recruitment of two type II receptors to form heterotetramers. Ligand binding induces phosphorylation of the type I receptor by the type II receptor, which leads to phosphorylation of cytoplasmic receptor-activated pSmads. The receptor-activated Smads form heteromeric complexes with Smad4, the central mediator in BMP/Smad signaling, which translocates from the cytoplasm to the nucleus to initiate hepcidin gene transcription (37). We found that the interaction with neogenin is required for cellular HJV processing in our previous studies (17, 24) and that the disruption of the HJV-neogenin interaction suppresses BMP4-induced hepcidin expression in this study. On the basis of these observations, we hypothesize that neogenin may regulate BMP signaling and hepcidin expression through several possible mechanisms. First, neogenin could be directly or indirectly

[3] A.-S. Zhang and C. A. Enns, unpublished observations.

Supplemental Material can be found at:
http://www.jbc.org/content/suppl/2009/06/29/M109.027318.DC1.html

involved in the proper assembly of the BMP receptor tetramer upon the binding of BMP ligand in the presence of HJV. In this scenario, disruption of the HJV-neogenin interactions at the cell surface will lead to the aberrant assembly of BMP receptors with HJV upon the BMP ligand binding and consequently result in the lack of BMP-signaling induction (Fig. 7). Second, neogenin could inhibit the degradation of BMP receptors once associated with HJV. Third, the signal transduction mediated by the neogenin cytoplasmic domain may play an important regulatory role in the induction of hepcidin expression. Understanding the requirement for neogenin in the activation of hepcidin transcription will be the subject of future research.

In addition, two recent studies indicate a critical role of BMP6 in iron homeostasis, presumably through HJV (38, 39). Kautz *et al.* (40) showed that similar to the hepatic hepcidin expression profile, BMP6 expression in the liver is positively regulated by dietary iron. Therefore, it will also be important to elucidate the role of neogenin in BMP6-regulated hepcidin expression.

In summary, we demonstrated that both HJV and neogenin are uniformly expressed in liver hepatocytes with no distinct gradient of distribution. Our results support the notion that in the presence of HJV, the induction of hepcidin expression by BMP4 requires neogenin.

Acknowledgments—We thank Dr. Pamela Bjorkman at Caltech for generously providing us with the neogenin FNIII 5–6 fragment and the neogenin ectodomain, Dr. Gregory Longmore at Washington University for generously giving us tTA-HepG2 cells and a tetracycline-inducible pcDNA4 plasmid, and Julia Maxson, Maja Chloupkova, Gary Reiness, Juxing Cheng, Junwei Gao, and Kristina Nicholson for critical reading of this manuscript and helpful comments.

REFERENCES

1. Hentze, M. W., Muckenthaler, M. U., and Andrews, N. C. (2004) *Cell* **117,** 285–297
2. De Domenico, I., McVey Ward, D., and Kaplan, J. (2008) *Nat. Rev. Mol. Cell Biol.* **9,** 72–81
3. Du, X., She, E., Gelbart, T., Truksa, J., Lee, P., Xia, Y., Khovananth, K., Mudd, S., Mann, N., Moresco, E. M., Beutler, E., and Beutler, B. (2008) *Science* **320,** 1088–1092
4. Finberg, K. E., Heeney, M. M., Campagna, D. R., Aydinok, Y., Pearson, H. A., Hartman, K. R., Mayo, M. M., Samuel, S. M., Strouse, J. J., Markianos, K., Andrews, N. C., and Fleming, M. D. (2008) *Nat. Genet.* **40,** 569–571
5. Papanikolaou, G., Samuels, M. E., Ludwig, E. H., MacDonald, M. L., Franchini, P. L., Dubé, M. P., Andres, L., MacFarlane, J., Sakellaropoulos, N., Politou, M., Nemeth, E., Thompson, J., Risler, J. K., Zaborowska, C., Babakaiff, R., Radomski, C. C., Pape, T. D., Davidas, O., Christakis, J., Brissot, P., Lockitch, G., Ganz, T., Hayden, M. R., and Goldberg, Y. P. (2004) *Nat. Genet.* **36,** 77–82
6. Zhang, A. S., Anderson, S. A., Meyers, K. R., Hernandez, C., Eisenstein, R. S., and Enns, C. A. (2007) *J. Biol. Chem.* **282,** 12547–12556
7. De Gobbi, M., Roetto, A., Piperno, A., Mariani, R., Alberti, F., Papanikolaou, G., Politou, M., Lockitch, G., Girelli, D., Fargion, S., Cox, T. M., Gasparini, P., Cazzola, M., and Camaschella, C. (2002) *Br. J. Haematol.* **117,** 973–979
8. Camaschella, C., Roetto, A., and De Gobbi, M. (2002) *Semin. Hematol.* **39,** 242–248
9. Huang, F. W., Pinkus, J. L., Pinkus, G. S., Fleming, M. D., and Andrews, N. C. (2005) *J. Clin. Invest.* **115,** 2187–2191
10. Niederkofler, V., Salie, R., and Arber, S. (2005) *J. Clin. Invest.* **115,** 2180–2186
11. Pigeon, C., Ilyin, G., Courselaud, B., Leroyer, P., Turlin, B., Brissot, P., and Loréal, O. (2001) *J. Biol. Chem.* **276,** 7811–7819
12. Frazer, D. M., Wilkins, S. J., Becker, E. M., Vulpe, C. D., McKie, A. T., Trinder, D., and Anderson, G. J. (2002) *Gastroenterology* **123,** 835–844
13. Babitt, J. L., Huang, F. W., Wrighting, D. M., Xia, Y., Sidis, Y., Samad, T. A., Campagna, J. A., Chung, R. T., Schneyer, A. L., Woolf, C. J., Andrews, N. C., and Lin, H. Y. (2006) *Nat. Genet.* **38,** 531–539
14. Babitt, J. L., Huang, F. W., Xia, Y., Sidis, Y., Andrews, N. C., and Lin, H. Y. (2007) *J. Clin. Invest.* **117,** 1933–1939
15. Feng, X. H., and Derynck, R. (2005) *Annu. Rev. Cell Dev. Biol.* **21,** 659–693
16. Wang, R. H., Li, C., Xu, X., Zheng, Y., Xiao, C., Zerfas, P., Cooperman, S., Eckhaus, M., Rouault, T., Mishra, L., and Deng, C. X. (2005) *Cell Metab.* **2,** 399–409
17. Maxson, J. E., Enns, C. A., and Zhang, A. S. (2009) *Blood* **113,** 1786–1793
18. Lin, L., Goldberg, Y. P., and Ganz, T. (2005) *Blood* **106,** 2884–2889
19. Silvestri, L., Pagani, A., and Camaschella, C. (2008) *Blood* **111,** 924–931
20. Lin, L., Nemeth, E., Goodnough, J. B., Thapa, D. R., Gabayan, V., and Ganz, T. (2008) *Blood Cells Mol. Dis.* **40,** 122–131
21. Zhang, A. S., West, A. P., Jr., Wyman, A. E., Bjorkman, P. J., and Enns, C. A. (2005) *J. Biol. Chem.* **280,** 33885–33894
22. Zhang, A. S., Xiong, S., Tsukamoto, H., and Enns, C. A. (2004) *Blood* **103,** 1509–1514
23. Davies, P. S., and Enns, C. A. (2004) *J. Biol. Chem.* **279,** 25085–25092
24. Zhang, A. S., Yang, F., Meyer, K., Hernandez, C., Chapman-Arvedson, T., Bjorkman, P. J., and Enns, C. A. (2008) *J. Biol. Chem.* **283,** 17494–17502
25. Feng, Y., and Longmore, G. D. (2005) *Mol. Cell. Biol.* **25,** 4010–4022
26. Yang, F., West, A. P., Jr., Allendorph, G. P., Choe, S., and Bjorkman, P. J. (2008) *Biochemistry* **47,** 4237–4245
27. Luxon, B. A. (2000) in *Liver Disease: Diagnosis and Management* (Bacon, B. R., and DiBisceglie, A. M., eds) pp. 3–15, Churchill Livingstone, Philadelphia
28. Xia, Y., Babitt, J. L., Sidis, Y., Chung, R. T., and Lin, H. Y. (2008) *Blood* **111,** 5195–5204
29. Kuns-Hashimoto, R., Kuninger, D., Nili, M., and Rotwein, P. (2008) *Am. J. Physiol. Cell Physiol.* **294,** C994–C1003
30. Conrad, S., Genth, H., Hofmann, F., Just, I., and Skutella, T. (2007) *J. Biol. Chem.* **282,** 16423–16433
31. Goldschneider, D., Rama, N., Guix, C., and Mehlen, P. (2008) *Mol. Cell. Biol.* **28,** 4068–4079
32. Schaffar, G., Taniguchi, J., Brodbeck, T., Meyer, A. H., Schmidt, M., Yamashita, T., and Mueller, B. K. (2008) *J. Neurochem.* **107,** 418–431
33. Matsunaga, E., and Chédotal, A. (2004) *Dev. Growth Differ.* **46,** 481–486
34. Matsunaga, E., Tauszig-Delamasure, S., Monnier, P. P., Mueller, B. K., Strittmatter, S. M., Mehlen, P., and Chédotal, A. (2004) *Nat. Cell Biol.* **6,** 749–755
35. Babitt, J. L., Zhang, Y., Samad, T. A., Xia, Y., Tang, J., Campagna, J. A., Schneyer, A. L., Woolf, C. J., and Lin, H. Y. (2005) *J. Biol. Chem.* **280,** 29820–29827
36. Xia, Y., Sidis, Y., Mukherjee, A., Samad, T. A., Brenner, G., Woolf, C. J., Lin, H. Y., and Schneyer, A. (2005) *Endocrinology* **146,** 3614–3621
37. Samad, T. A., Rebbapragada, A., Bell, E., Zhang, Y., Sidis, Y., Jeong, S. J., Campagna, J. A., Perusini, S., Fabrizio, D. A., Schneyer, A. L., Lin, H. Y., Brivanlou, A. H., Attisano, L., and Woolf, C. J. (2005) *J. Biol. Chem.* **280,** 14122–14129
38. Meynard, D., Kautz, L., Darnaud, V., Canonne-Hergaux, F., Coppin, H., and Roth, M. P. (2009) *Nat. Genet.* **41,** 478–481
39. Andriopoulos, B., Jr., Corradini, E., Xia, Y., Faasse, S. A., Chen, S., Grgurevic, L., Knutson, M. D., Pietrangelo, A., Vukicevic, S., Lin, H. Y., and Babitt, J. L. (2009) *Nat. Genet.* **41,** 482–487
40. Kautz, L., Meynard, D., Monnier, A., Darnaud, V., Bouvet, R., Wang, R. H., Deng, C., Vaulont, S., Mosser, J., Coppin, H., and Roth, M. P. (2008) *Blood* **112,** 1503–1509

Supplemental Materials and Methods

In situ hybridization

In situ hybridization analysis of HFE2 and neogenin mRNA in rat liver tissues was performed as previously described (1). Briefly, the digoxigenin-labeled antisense and sense riboprobes for rat HFE2 and neogenin were synthesized by *in vitro* transcription using either MEGAscript SP6 kit or MEGAscript T7 kit (Ambion, Austin, TX). The fragments of rat HFE2 and neogenin cDNA used for riboprobe synthesis were amplified from a rat liver cDNA preparation by PCR using the Expand High Fidelity PCR system (Roche Applied Science), followed by cloning into pGEM-T vector (Promega). The primers used for HFE2 cDNA amplification were 5'- CTATGAAGCCCGGTTTTCCA-3' (forward) and 5'-GGAAAAGGTGCAAGTTCTCCAA-3' (reverse). The primers used for rat neogenin cDNA amplification were 5'-CTCATGCCCAGACCATCAAA-3' (forward) and 5'-CTGGTGGCCTCCTGTACCTC-3' (reverse). The amplicons were confirmed by DNA sequencing.

Immunohistochemistry.

Immunohistochemistry was used to localize the expression of HJV and neogenin proteins in rat liver tissues. Formalin-fixed and paraffin-embedded rat liver sections (5 μm thick) were processed for the analysis of HJV, neogenin and glial fibrillary acidic protein (GFAP, a specific marker for HSC in liver) (2). Briefly, tissue sections were fixed with 1% paraformaldehyde in PBS for 15 min at room temperature, followed by permeabilization with 0.2% Triton X-100 for another 15 min. After 1 hr blocking in PBS with 3% bovine serum albumin (BSA) (blocking buffer), tissue sections were incubated with affinity-purified rabbit anti-HJV antibody (1 μg/ml), rabbit anti-neogenin (1 μg/ml, Santa Cruz Biotechnology), or mouse anti-GFAP-CY3 conjugate (1 μg/ml, Sigma) in blocking buffer at 4°C overnight. For anti-GFAP-CY3 conjugate, tissues were directly mounted with ProLong Antifade (Molecular Probes, OR) and imaged by a Nikon TE200 microscope (Meridian Instrument Company, Inc., Kent, WA) at the magnifications indicated in the text. For anti-HJV and neogenin antibodies, tissue sections were further incubated with Alexa 488-labeled goat anti-rabbit antibody (1:500 dilution; Molecular Probes, OR) for 1 h at room temperature, followed by soaking in 50 mM ammonium acetate buffer (pH 5.0) with 5 mM CuSO4 for 10 min to quench the autofluorescence (3). Rabbit IgG (1 μg/ml) and soluble HJV preabsorbed-rabbit anti-HJV antibody (1 μg/ml) were used as negative controls. The rabbit anti-HJV antibody cross-reacts with rat HJV (4).

References

1. Zhang, A. S., Xiong, S., Tsukamoto, H., and Enns, C. A. (2004) *Blood* **103**, 1509-1514
2. Knittel, T., Kobold, D., Piscaglia, F., Saile, B., Neubauer, K., Mehde, M., Timpl, R., and Ramadori, G. (1999) *Histochem. Cell Biol.* **112**, 387-401
3. Schnell, S. A., Staines, W. A., and Wessendorf, M. W. (1999) *J. Histochem. Cytochem.* **47**, 719-730
4. Zhang, A. S., Anderson, S. A., Meyers, K. R., Hernandez, C., Eisenstein, R. S., and Enns, C. A. (2007) *J. Biol. Chem.* **282**, 12547-12556

Supplemental Figure 1. *In situ* hybridization and immunohistochemistry analysis of HFE2 and neogenin expression in liver tissue sections. A. *In situ* hybridization analysis of HFE2 and neogenin mRNA localization in liver tissue sections. Digoxigenin-labeled antisense riboprobes for rat HFE2 and neogenin were used to probe HFE2 and neogenin mRNA in rat liver tissue sections, respectively. The corresponding sense riboprobes were used as negative controls. Images were taken under light microscope at 200x magnifications. B. Immunohistochemistry analysis of HJV and neogenin protein localization in rat liver tissue sections. Rabbit antibodies against HJV and neogenin were used to probe the HJV and neogenin proteins in rat liver sections, respectively. Mouse antibody against GFAP, a HSC marker protein, was used to stain the HSC. Anti-HJV antibody was used alone, and images were taken under fluorescent microscopy at 400x magnification. Antibodies against neogenin and GFAP were used for double labeling. Rabbit IgG was used as a negative control. C. Immunohistochemistry analysis of neogenin protein localization by confocal microscopy. The same rat liver tissue sections as described in B were visualized under the confocal microscopy at 1,000x magnification. Rabbit antibody against neogenin was used to probe the neogenin protein (neo), whereas the mouse antibody against GFAP, a HSC marker protein, was used to stain the HSC.

Supplemental Figure 2. Characterization of G99V, D172E and G320V mutant HJV. A. G99V HJV, but not D172E and G320V HJV, binds neogenin. myc-HJV (HJV with a N-terminal *myc* tag), HJV, G320V HJV, G99V HJV, or D172E HJV was co-transfected with neogenin into HEK293 cells. HJV in the cell lysates was immunoprecipitated (IP) with rabbit anti-HJV 18745 antibody and the Pansorbin beads. Immunoprecipiated proteins were separated by SDS-PAGE, followed by immunoblotting (IB) with both anti-HJV and anti-neogenin (neo) antibodies. HEK293 cells transfected with pcDNA3 empty vector (C) were used as a negative control. B. Released G99V HJV has a lower molecular weight. HepG2 cells stably expressing HJV, G320V HJV, D172E HJV, or G99V HJV were subcultured into 12-well plates with complete medium. After 48-hr, medium was changed to MEM/5% FCS (1 ml per well). About 18 hr later, conditioned medium (CM) was collected and cell lysates were prepared. About 120 μl of CM and the total cell lysate were subjected to SDS-PAGE, followed by immunodetection of HJV in CM and neogenin (neo), HJV and β-actin in the lysate (L). HepG2 cells transfected with pcDNA3 empty vector (C) were used as a negative control. C. Flow cytometry analysis of cell surface HJV. HepG2 cells stably expressing HJV, G320V HJV, D172E HJV, or G99V HJV were first detached from flasks with the cell dissociation buffer (Invitrogen). Cells were then incubated with affinity-purified rabbit anti-HJV antibody (4 μg/ml) in Hanks Buffer supplemented with 3% fetal bovine serum for 30 min at 4°C, followed by incubation with phycoerythrin-conjugated goat anti-rabbit IgG (1:500 dilution) (Caltag, Burlingame, CA) in the same buffer for 30 min at 4°C. Flow cytometry analysis was performed on a Becton Dickinson FACSCalibur flow cytometer. Rabbit IgG and control-HepG2 cells were used as negative controls. The levels of cell surface HJV are expressed as arbitrary units. All the experiments were repeated at least three times with consistent results. The qRT-PCR results in C were assessed by one-way ANOVA, and the statistical significant difference relative to HJV-HepG2 cells were determined by Tukey's post test. ** $P<0.01$.

Supplemental Figure 3. Neo FNIII 5-6 disrupts the HJV/neogenin interactions. HEK293 cells stably expressing both HJV and neogenin were incubated in MEM (without met/cys)/2% FCS/^{35}S-(met/cys) (100 μCi/ml, Perkin Elmer) for 4 hours to metabolically label the cellular proteins. After washing the cells with PBS, cell lysates were prepared and incubated in the presence of 20 μM holo-Tf (Tf), 40 nM Neo FNIII 5-6 (N-FNIII), or 1 μM soluble neogenin ectodomain (N-ecto) for 1 hr at 4°C. Afterwards, HJV was immunoprecipitated with the Pansorbin precoated with either pre-immune serum (ctrl), rabbit anti-neogenin (anti-neo) or rabbit anti-HJV 18745 antibody (anti-HJV). Immunoprecipitated proteins were separated by SDS-PAGE. Image was obtained by exposure to X-ray film. During the process of gel drying, the gel was warped which caused the slanted neogenin bands. This experiment was repeated three times with consistent results.

sFigure 1.

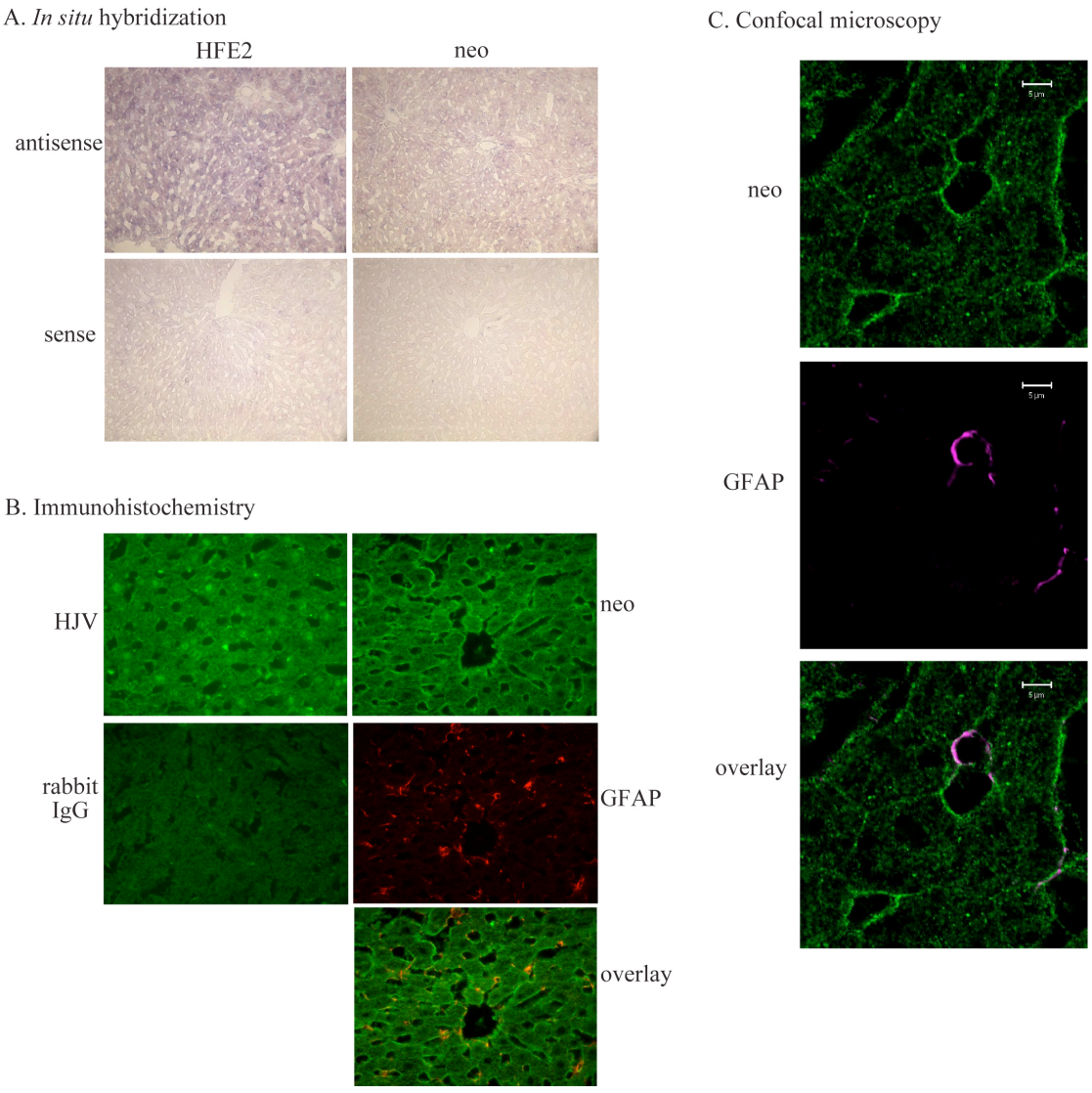
A. *In situ* hybridization
HFE2
neo
antisense
sense
B. Immunohistochemistry
HJV
neo
rabbit IgG
GFAP
overlay
C. Confocal microscopy
neo
GFAP
overlay

sFigure 2.

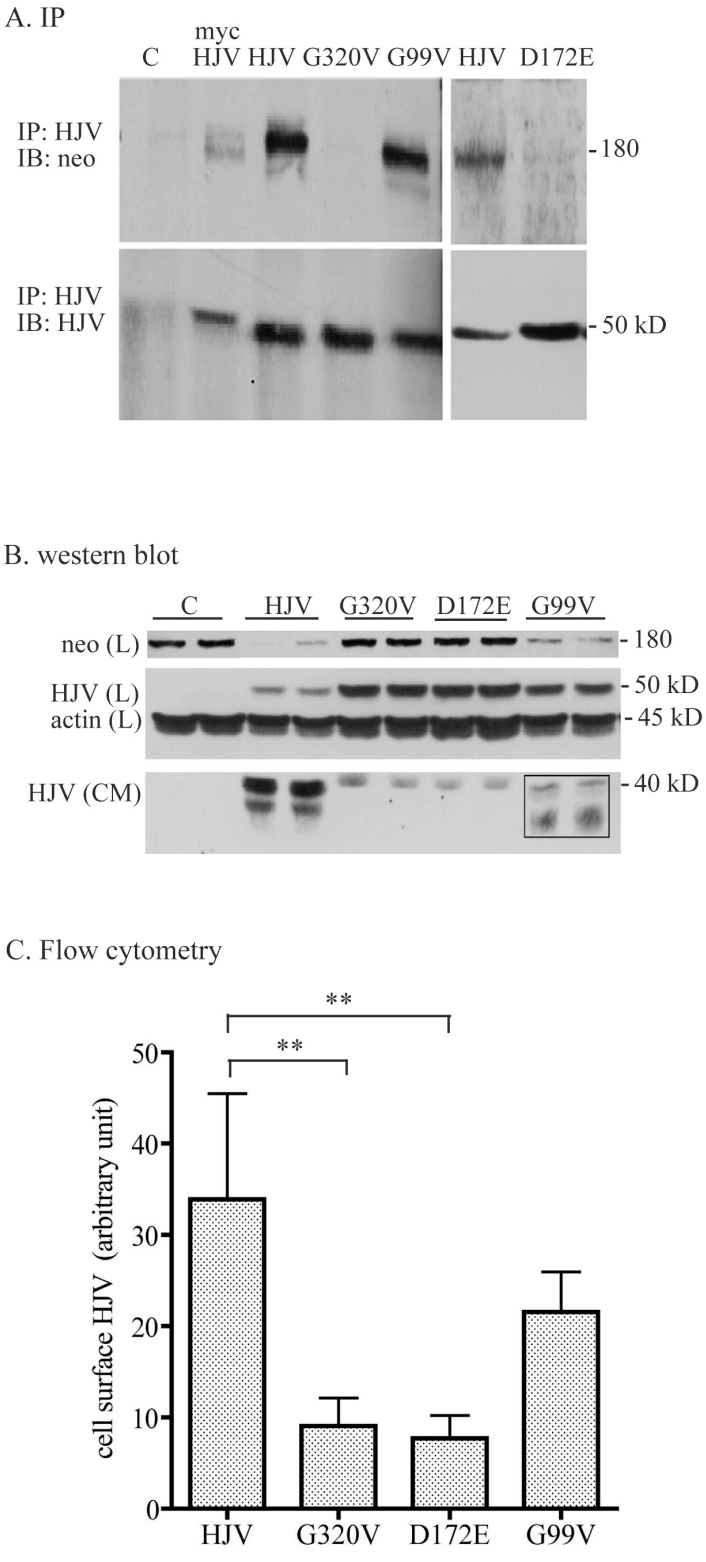
A. IP
myc
C
HJV
HJV G320V
G99V HJV
D172E
IP: HJV
IB: neo
180
IP: HJV
IB: HJV
50 kD
B. western blot
C
HJV
G320V
D172E
G99V
neo (L)
180
HJV (L)
50 kD
actin (L)
45 kD
HJV (CM)
40 kD
C. Flow cytometry
**
**
cell surface HJV (arbitrary unit)
50
40
30
20
10
0
HJV
G320V
D172E
G99V

sFigure 3

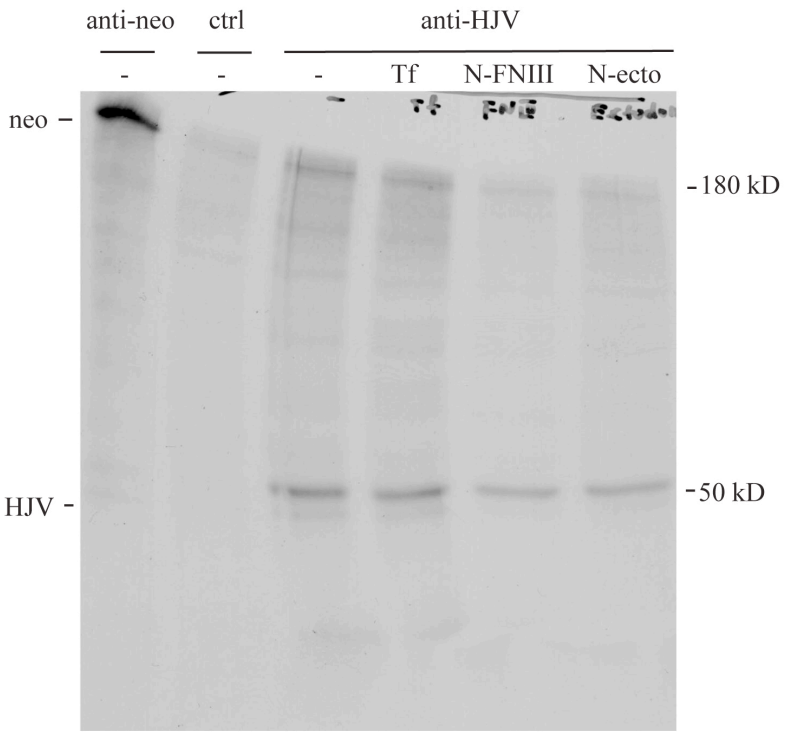

Appendix C

Matlab scripts for the L1 project

Matlab script for profile simulation for given adhesion strength

```
% **********************File name: E_minimization.m**********************
% Fan Yang
% This subroutine returns the configuration parameters with the total lowest energy value
once the adhesion strength w, reduced volume Sigma, and total area A0 are specified.

function p=E_minimization(w,Sigma,A0)

%clear all
N=6000;
lambda=linspace(0.01,50,N);
cspace=linspace(-0.99,0.99,200);

% initial total area, passed to the current subroutine
% A0=4*pi*8*8; % R0=8

%Scan lambda values and store the resulting energy E, R and c in an arrays
%c1(2), R1(2) and E1(2).
for i=1:N
   %Find the minimal value of D=peliminate([-.99,0.99],lambda(i)).
   %If min is less than zero, start root searching toward both ends
   %If min is bigger than zero, no root will be found - exit with error.
   for j=1:length(cspace)
      D(j)=peliminate_x(cspace(j),lambda(i),Sigma);
   end
   [Dmin,Imin]=min(D);
   if Dmin<0

   opts=optimset('TolX',1e-10,'TolFun',1e-10);
   %Look for root to the left and right of the minimum of D(i) to find
   %roots of D
```

```
    try
        c(i)=fzero(@(x) peliminate_x(x,lambda(i),Sigma),[-0.99,cspace(Imin)],opts);
        R3(i)=sqrt(A0/(pi*(lambda(i)*lambda(i)+2*(lambda(i)+sqrt(1-
c(i)*c(i)))^2/(1+c(i))+2*lambda(i)*acos(-c(i))+2*(1+c(i)))));
        E(i)=TotalE_w(R3(i),c(i),lambda(i),w);
    catch ME1
        idSegLast = regexp(ME1.identifier, '(?<=:)\w+$', 'match');
        if strcmp(idSegLast, 'ValuesAtEndPtsSameSign')
            c(i)=NaN;
            R3(i)=NaN;
            E(i)=NaN;
        end
    end



    else
        c(i)=NaN;
        R3(i)=NaN;
        E(i)=NaN;

    end
end

[E1min Imin]=min(E);
R3min=R3(Imin);
cmin=c(Imin);
lambda_min=lambda(Imin);

    p(1)=R3min;
    p(2)=lambda_min;
    p(3)=cmin;
```

```
% **********************File name: peliminate_x.m**********************
% Fan Yang
% "p" denotes parameterized, meaning that the user is allowed to supply a parameter
lambda here rather than a given number.
% eliminate R3 using the area and volume constraints

function D=peliminate(c0,lambda,Sigma)

if lambda>0
V=2/3*pi*(lambda/sqrt(1-c0*c0)+1)^3*(1-c0)+pi/3*(lambda+sqrt(1-
c0*c0))^2*(lambda/sqrt(1-c0*c0)+1)*(-c0)+pi*(1+c0)*lambda*lambda+pi*c0*sqrt(1-
c0*c0)*lambda+pi*(1+c0)*(1+c0)-1/3*pi*(1+c0)^3+pi*2*lambda*asin(sqrt((1+c0)/2));
A=pi*(lambda*lambda+2*(lambda+sqrt(1-c0*c0))^2/(1+c0)+2*lambda*acos(-
c0)+2*(1+c0));
%R=V/A^(3/2)-Sigma/(6*sqrt(pi));
D=V-A^(3/2)*Sigma/(6*sqrt(pi));

else D=(4/3*pi*(1-c0)+pi/3*(1-c0*c0)*(-c0)+(1+c0)^2+1/3*(1+c0)^3)/(4*pi)^1.5-
Sigma/(6*sqrt(pi));
end



% **********************File name: TotalE_w.m**********************
% Fan Yang
% This subroutine calculates and returns the total energy for an adhered vesicle when all
configuration parameters and the adhesion energy density are provided.

function TE=TotalE_w(R,c,lambda,w)

   if lambda>1,
```

```
    TE=4*pi*k*(1-c)+k*pi/sqrt(lambda^2-1)*(4*sqrt(lambda^2-1)-
2*lambda^2*atan((1+lambda*sqrt((1-c)/(1+c)))/(sqrt(lambda^2-1)))+4*c*sqrt(lambda^2-
1)+lambda^2*pi)-w*pi*lambda^2*R^2;
  elseif lambda<1,
    TE=8*pi*k+k*pi*lambda*lambda/sqrt(1-lambda*lambda)*log(((1+sqrt(1-
lambda*lambda))*(lambda+sqrt(1-c*c))/(lambda*(1-c*sqrt(1-
lambda*lambda)+lambda*sqrt(1-c*c)))))-w*pi*lambda^2*R^2;
  else
    TE=8*pi*k+2*k*pi/(1+sqrt((1-c0)/(1+c0)))-w*pi*lambda^2*R^2;
  end
```

Matlab scripts for confocal data processing

```
% Tristan Ursell - extraction of vesicle shape from confocal z-stack
% March 2009
% Vesicle Adhesion Shape Analysis
%
% Fan Yang - fitting the extracted profile to the basic shape model
clear all
close all

% file1 is a tiff stack of confocal images. There should be only one vesicle in the field of
% view. The z-stack is built such that it starts from the top of a vesicle toward the
% coverglass (adhesion zone).
[file1,aa]=imgetfile;
%[file1,dir]=uigetfile('*.tif','MultiSelect', 'on');

% get the number of images in the stack
N=length(imfinfo(file1));

% Pick an image in the middle of the stack and select a region about the center of the
% vesicle. The average intensity in the selected region is analyzed for each image, and it
```

```
% reaches maximum when the section is focused on the adhesion patch on the bottom of
% the vesicle. N is then changed to the frame number for this section so that we only
% analyze images at or above the adhesion zone.
colormap(gray);
Im=imread(file1,floor(N/2));
imagesc(Im);
% choose the region of interest by mouse clicking
[B roi]=imcrop;
for i=1:N
   Ims=imread(file1,i);
   Ims_crop=imcrop(Ims,roi);
   mean_crop(i)=mean2(Ims_crop);
end
[C bt_ind]=max(mean_crop);
N=bt_ind;

disp(['This z-stack has ' num2str(N) ' images.']);

% The center of the vescile is determined by analyzing the sections focused in the middle
% of the vesicle where a clear circle can be obtained by thresholding. The threshold is
% determined by user selecting the bright region and the dark region. Pixels with an
% intensity bigger than that of the dark region by more than 0.95*(difference between
% dark and bright region) is used in the next step for curve fitting. The circle is fitted to
% obtained the position of the center, and the cooridinates from all centering frames are
% averaged.

% choose centering frames
startf=input('Enter initial centering frame:  ');
endf=input('Enter final centering frame:  ');

centN=endf-startf+1;
```

```
%xy plane pixel conversion (um/px)
conv=0.1136;

% Cutoff between dark and light
C=0.95;

q1=input('Analyze brightness of all centering frames?(y/n) ','s');

if q1=='y'
   figure
   colormap(gray)
   for i=startf:endf
      disp('Choose a brightness cutoff...')
      disp(' ')
      Im=imread(file1,i);
      imagesc(Im)
      axis equal
      axis tight
      title('Choose dark region.')
      rect1=round(getrect);
      dark=Im(rect1(2):rect1(2)+rect1(4),rect1(1):rect1(1)+rect1(3));
      title('Choose light region.')
      rect2=round(getrect);
      light=Im(rect2(2):rect2(2)+rect2(4),rect2(1):rect2(1)+rect2(3));

      cut(i)=(mean(mean(light))-mean(mean(dark)))*C+mean(mean(dark));

      clear T
      T(:,:,1)=mat2gray(Im)-mat2gray(Im).*double(Im>cut(i));
      T(:,:,2)=mat2gray(Im);
```

```
        T(:,:,3)=mat2gray(Im)-mat2gray(Im).*double(Im>cut(i));

        imagesc(T)
        axis equal
        axis tight
        title(['Frame ' num2str(i) ' / ' num2str(i-startf+1) ' of ' num2str(centN)])
        pause(1)
    end
    close
else
    figure
    colormap(gray)
    disp('Choose a brightness cutoff...')
    disp(' ')
    Im=imread(file1,startf);
    imagesc(Im)
    axis equal
    axis tight
    title('Choose dark region.')
    rect1=round(getrect);
    dark=Im(rect1(2):rect1(2)+rect1(4),rect1(1):rect1(1)+rect1(3));
    title('Choose light region.')
    rect2=round(getrect);
    light=Im(rect2(2):rect2(2)+rect2(4),rect2(1):rect2(1)+rect2(3));

    cut(startf)=(mean(mean(light))-mean(mean(dark)))*C+mean(mean(dark));

    disp('Choose a brightness cutoff...')
    disp(' ')
    Im=imread(file1,endf);
    imagesc(Im)
```

```
    axis equal
    axis tight
    title('Choose dark region.')
    rect1=round(getrect);
    dark=Im(rect1(2):rect1(2)+rect1(4),rect1(1):rect1(1)+rect1(3));
    title('Choose light region.')
    rect2=round(getrect);
    light=Im(rect2(2):rect2(2)+rect2(4),rect2(1):rect2(1)+rect2(3));

    cut(endf)=(mean(mean(light))-mean(mean(dark)))*C+mean(mean(dark));

    for i=startf+1:endf-1
        cut(i)=cut(startf)+(cut(endf)-cut(startf))/centN*(i-startf);

        Im=imread(file1,i);
        clear T
        T(:,:,1)=mat2gray(Im)-mat2gray(Im).*double(Im>cut(i));
        T(:,:,2)=mat2gray(Im);
        T(:,:,3)=mat2gray(Im)-mat2gray(Im).*double(Im>cut(i));

        imagesc(T)
        axis equal
        axis tight
        title(['Frame ' num2str(i) ' / ' num2str(i-startf+1) ' of ' num2str(centN)])
        pause(0.5)
    end
end

%Perform the center frame circle fitting
n=1;
for i=startf:endf
```

```
Im=imread(file1,i);
[Y,X]=find(Im>cut(i));
for j=1:length(X)
   Z(j)=double(Im(Y(j),X(j)));
end

g = @(R)  sum(Z'.^n.*(R(1)-sqrt((R(2)-X).^2+(R(3)-Y).^2)).^2);

if i==startf
   R0=[size(Im,1)/4,size(Im,1)/2,size(Im,2)/2];
else
   R0=[r(i-1),X0(i-1),Y0(i-1)];
end

R=fminsearch(g,R0);

r(i)=R(1);
X0(i)=R(2);
Y0(i)=R(3);

%Plot the result
T(:,:,1)=mat2gray(Im)-mat2gray(Im).*double(Im>cut(i));
T(:,:,2)=mat2gray(Im);
T(:,:,3)=mat2gray(Im)-mat2gray(Im).*double(Im>cut(i));

theta=0:0.01:2*pi;
Xp=r(i)*cos(theta)+X0(i);
Yp=r(i)*sin(theta)+Y0(i);

imagesc(T)
```

```
    hold on
    plot(Xp,Yp,'r')
    plot(X0(i),Y0(i),'bo')
    axis equal
    axis tight
    title(['Frame ' num2str(i) ' / ' num2str(i-startf+1) ' of ' num2str(centN)])
    pause(0.5)
    hold off

    clear X Y Z R T Xp Yp
end
close

Xcent=mean(X0(startf:endf));
Ycent=mean(Y0(startf:endf));

% The intensity in a shell is averaged to provide a radial intensity profile for each frame.
% determining minimum polar size
sz=size(Im);
s1=abs(sz(2)-Xcent);
s2=abs(Xcent);
s3=abs(sz(1)-Ycent);
s4=abs(Ycent);

% Establish maximum polar information radius
Rmin=round(0.9*min([s1,s2,s3,s4]));
Rminsq=Rmin^2;

% Get bin positions
clear bins
dR=0.33;
```

```
bins=conv*(dR/2:dR:Rmin);

% Create data matrices
binmean=zeros(N,length(bins));
binstd=zeros(N,length(bins));

% Find the points that lie within Rmin of the vesicle center
m=0;
for j=1:size(Im,1)
   for k=1:size(Im,2)
      if ((j-Ycent)^2+(k-Xcent)^2)<Rminsq
         m=m+1;
         R(m)=sqrt((j-Ycent)^2+(k-Xcent)^2);
         RminX(m)=k;
         RminY(m)=j;
      end
   end
end

% Performing the symmetry revolution
figure;
for i=1:N
   %i=30;
   clear V
   Im=imread(file1,i);

   for j=1:m
      V(j)=Im(RminY(j),RminX(j));
   end

   % Create histogram-averaged profile
```

```
for p=1:length(bins)
   clear binvals
   %find the points in the p-th bin
   binvals=find(and(((p-1)*dR)<R,(p*dR)>=R));
   %calculate the mean of those points
   if size(binvals,2)>0
      binmean(i,p)=mean(double(V(binvals)));
   else
      binmean(i,p)=NaN;
   end

   % Calculate the STD of these points
   if length(binvals)>1
      binstd(i,p)=std(double(V(binvals)));
   else
      binstd(i,p)=NaN;
   end

   % Plot the results
   plot(R*conv,V,'k.')
   hold on
   plot(bins,binmean(i,:),'r','LineWidth',2)
   %plot(r(i),max(binmean),'go','LineWidth',2)
   plot(bins,binmean(i,:)+binstd(i,:),'Color',[1,0.7,0],'LineWidth',1)
   plot(bins,binmean(i,:)-binstd(i,:),'Color',[1,0.7,0],'LineWidth',1)
   box('on')
   xlabel('R(um)')
   ylabel('Intensity(au)')
   title(['Frame ' num2str(i) ' of ' num2str(N)])
   hold off
end
```

```
   pause(0.1)
end
close

% Create final plots
clear Z
% step size in Z direction is 0.2 micron
dZ=0.2;
Z=0:dZ:(N-1)*dZ;
Z=Z-Z(bt_ind);
Z=-Z;
% Z coordinate is modified by taking into consideration the refractive index mismatch
% using routine test_optics.
for i=1:N
   Z(i)=10^6*test_optics(Z(i)*1e-6)+Z(i); % in microns
end

colormap(hot)

surf(bins,Z,binmean,'LineStyle','none')
hold on
surf(-bins,Z,binmean,'LineStyle','none')

view([0,90])
xlabel('R(um)')
ylabel('Z(um)')
title('Mean Polar Symmetric Intensity')
axis equal
axis tight
```

```
% Select points from the radial profile. Those higher than the average by more than
% 1.5*standard deviation is considered a point on the vesicle.
binmean_nor=mat2gray(binmean);
mean_v=mean2(binmean_nor);
std_v=std2(binmean_nor);
bg=mean_v+1.5*std_v;

X_data=[];
Z_data=[];
weight_data=[];
for i=1:N
% The first 3 points in radial profile is not used since they came from the average of too
% few pixels.
ind=find((binmean_nor(i,4:length(bins))>max(binmean_nor(i,4:length(bins)))*.85).*(bin
mean_nor(i,4:length(bins))>bg));
   if isempty(ind)
   else
      X_data=[X_data bins(ind+3)];
      for j=1:length(ind)
         Z_data=[Z_data Z(i)];
      end
      weight_data = [weight_data binmean_nor(i, ind+3)];

   end
end
weight_data = weight_data/sum(weight_data);


plot3(X_data,Z_data,sign(X_data)*1000,'b.');
plot3(-X_data,Z_data,sign(X_data)*1000,'b.');
```

```
% Now perform fitting to X_data and Z_data using basic shape model. Random initial
% conditions for the three unknown parameters are provided at the beginning of search
and the set of parameters that gives the smallest error is reported as p_final_out

fun_final=[];
p_final=[];

% Number of cycles for different random initial conditions
N_cyc=40;

for i=1:N_cyc
   % Generate four random numbers on the unit interval
   r1=rand;
   r2=rand;
   r3=rand;
   p_ini=[0.1+r1*(1-0.01) 0.1+r2*(5-0.1) -1+r3*2];
   tic
   % Search for a set of parameters that would minimize the given function
   [p_fit fun_err]=fminsearch(@(p) AdhesionError _3p(X_data,Z_data,0,p),p_ini);
   toc
   fun_final=[fun_final;fun_err];
   p_final=[p_final;p_fit];
end

[fun_final_min p_final_ind] = min(fun_final);
p_final_out = [p_final(p_final_ind, :) 0];
[x_fit z_fit] = AdhesionCurve(p_final_out);
figure;
plot(X_data, Z_data, 'rx');
hold on
plot(x_fit, z_fit, 'k.');
```

```
% ****************File name: AdhesionError_3p.m*******************
function err=AdhesionError_3p(x,z,z0,p)
% This function calculates the relative mean square error between the
% "experimental" profile (x,z) and the theoretical one given by parameter
% vector p
R3=p(1);
lambda=p(2);
c=p(3);
%x: xdata vector
%z: zdata vector
Neff=length(x);

err=0;
for i=1:1:length(x)
   %Calculate the theoretical positions by calling ModelCoor subroutine
   [xtmp ztmp ifoutside]=ModelCoor(x(i),z(i),[p z0]);
   %Calculate the errors
   err=err+((x(i)-xtmp)^2+(z(i)-ztmp)^2)/(xtmp^2+ztmp^2);
   %At the junction of two regions, ignore the data points
   Neff=Neff-ifoutside;
end
err=err/Neff;



% File name: test_optics.m
% This function calculates and returns the real z-coordinate from the nominal coordinates
% by correcting for the refractive index mismatch.

function z_max=test_optics(d)
n1=1.515;
```

```
n2=1.34;
NA=1.40;
alpha=asin(NA/n1);
theta1=linspace(0.01,alpha,200);
theta2=zeros(size(theta1));
tao_s=zeros(size(theta1));
tao_p=zeros(size(theta1));
phi_d=zeros(size(theta1));
P=ones(size(theta1));

% d=10*1e-6;
lambda=568e-9; % wavelength
k0=2*pi/lambda;
k2=2*pi*n2/lambda;
for j=1:1:200,
   theta2(j)=asin(n1*sin(theta1(j))/n2);
   tao_s(j)=2*sin(theta2(j))*cos(theta1(j))/sin(theta1(j)+theta2(j));
   tao_p(j)=2*sin(theta2(j))*cos(theta1(j))/(sin(theta1(j)+theta2(j))*cos(theta1(j)-
theta2(j)));
   phi_d(j)=-d*(n1*cos(theta1(j))-n2*cos(theta2(j)));
   %P(j)=sqrt(cos(theta1(j)));
end

z=linspace(-d/2,d/2,200);
I0=zeros(size(z));
h=zeros(size(z));
for k=1:1:200
   I0(k)=0;
   for j=1:1:200,
```

```
I0(k)=I0(k)+P(j)*sin(theta1(j))*(tao_s(j)+tao_p(j)*cos(theta2(j)))*exp(i*(k0*phi_d(j)+k2
*z(k)*cos(theta2(j))));
   end
   h(k)=abs(I0(k))*abs(I0(k));
end

%figure

%plot(z,h);

[C I]=max(h);
z_max=z(I);
```

Surface Evolver sample script

```
/* Revisions by Ken Brakke, Feb. 26, 2010
  enabled fixed area constraint
  set facet tension to 0
  fixed bug in Evolver regarding gradient of star*sq_mean_curvature on constraints.
  wrote "gogo" procedure to illustrate evolution techniques for keeping
  the bottom vertices well groomed; particularly necessary since the
   way squared mean curvature is calculated for discrete surfaces.

  Revisions by Ken Brakke, Mar. 1, 2010
    Vertices along the contact line still want to go sideways too much.
      So adding a constraint guidecon to keep the contact line vertices
      on fixed radial lines.  Had to re-center starting coordinates to
```

```
      get nice central symmetry to start with.
    Tried different versions of star sq curvature; star_normal worked
      best, winding up with no negative eigenvalues after "gogo".
*/
gravity_constant 0
/* fix area */
quantity totalarea fixed = 5 method facet_area global
/* bending energy */
// sq_mean has problems with horns.
// quantity stnsq energy modulus 1 method sq_mean_curvature global
// star_perp has trouble convergin.
//quantity stnsq energy modulus 1 method star_perp_sq_mean_curvature global
// star_normal seems to work pretty well; at least no negative eigenvalues
// after "gogo" and hessian_seek works.
quantity stnsq energy modulus 1 method star_normal_sq_mean_curvature global
// star_eff_area comes up with a few negative eigenvalues after "gogo"
// quantity stnsq energy modulus 1 method star_eff_area_sq_mean_curvature global
/* adhesion energy */
quantity adhesion energy modulus 1 method facet_scalar_integral
scalar_integrand: -5 /* user enters adhesion energy here */
/* fix the bottom on a plane */
constraint 1   /* the table top */
formula: z = 0
// Guide lines for keeping contact line vertices spaced out.
parameter guidemult = 4    // should be doubled each refinement
constraint guidecon
formula: sin(guidemult*atan2(y,x))

vertices
1  -0.5 -0.5 0.0  constraint 1,guidecon  /* 4 vertices on plane */
2   0.5 -0.5 0.0  constraint 1,guidecon
```

```
3   0.5  0.5 0.0  constraint 1,guidecon
4  -0.5  0.5 0.0  constraint 1,guidecon
5  -0.5 -0.5 1.0
6   0.5 -0.5 1.0
7   0.5  0.5 1.0
8  -0.5  0.5 1.0

edges  /* given by endpoints and attribute */
1   1 2    constraint 1,guidecon /* 4 edges on plane */
2   2 3    constraint 1,guidecon
3   3 4    constraint 1,guidecon
4   4 1    constraint 1,guidecon
5   5 6
6   6 7
7   7 8
8   8 5
9   1 5
10  2 6
11  3 7
2  4 8

faces  /* given by oriented edge loop */
1   1 10 -5  -9 density 1
2   2 11 -6 -10 density 1
3   3 12 -7 -11 density 1
4   4  9 -8 -12 density 1
5   5  6  7   8 density 1
6  -4 -3 -2  -1  color green constraint 1 density 1 adhesion

bodies  /* one body, defined by its oriented faces */
1   1 2 3 4 5 6 volume 1
```

```
//1   1 2 3 4 5 6  volume 1  density 1

read
set facet tension 0
linear_metric on // for consistently normalized eigenvalues
// Initial squish to get it started better
set vertex z z*0.7
// Grooming subroutine, for bottom facets.  Don't want to use vertex
// averaging on contact line vertices.
groom_size := 1;
groom := {
 fix vertices where on_constraint 1;
 unfix vertices vv where on_constraint 1 and sum(vv.facet, not on_constraint 1) == 0;
 refine edge where on_constraint 1 and length > groom_size;
 u; V; u; V;
 unfix vertices;
 delete edge where on_constraint 1 and length < groom_size/4;
 fix vertices vv where on_constraint 1 and sum(vv.facet, not on_constraint 1) == 0;
}

// Re-define r to automatically adjust groom_size
r :::= { guidemult *= 2; 'r'; groom_size /= 2; }

// Typical evolution.  Problem is that since curvature averages over adjacent facet area,
//rim facets on the bottom want to increase in area toward the inside, since that does not
//change the angles at the contact line vertices, but does increase the area averaged over.

gogo := {
  r;
  r;
  refine edge ee where sum(ee.facet,color==green)==1;
```

```
 m 0;  // give it a chance to adjust volume
 g;
 g;
 optimize 0.1;  // now start minimizing energy
 g;
 u;
 {g 5; groom;} 100;
 r;
 {g 5; groom; } 20;

 // try some second-order convergence
 hessian_seek;  // seems happy; hessian scale near 1.
 hessian_seek;
 v;
}
```